

Quantum Monte Carlo Investigation of Quantum Phase Transitions of Mixed Heisenberg Spin Chains

DIPLOMARBEIT/DIPLOMA THESIS

vorgelegt von
Rainer Bischof

durchgeführt am
Institut für Theoretische Physik
der Technischen Universität Graz

in Zusammenarbeit mit dem
Institut für Theoretische Physik
der Universität Leipzig

unter der Betreuung von
Prof. Dr. Wolfhard Janke (Leipzig)
und
Ao. Univ.-Prof. Dr. Hans Gerd Evertz (Graz)

Graz, Februar 2006

Dedicated to the memory of my father.

Abstract

Quanten-Phasenübergänge in antiferromagnetischen Heisenbergschen Spinketten, bestehend aus zwei unterschiedlichen Spinsorten S_a und S_b , die jeweils paarweise alternierend angeordnet sind, werden für die Fälle $S_a = 1/2$ und $S_b = 1$, $S_a = 1/2$ und $S_b = 3/2$ sowie $S_a = 1$ und $S_b = 3/2$ anhand von Quanten-Monte-Carlo Simulationen bei tiefen Temperaturen untersucht. Variation des Parameters α , der das Verhältnis der Kopplungskonstanten zwischen Spins ungleicher bzw. gleicher Sorte angibt, führt zu qualitativ unterschiedlichen Grundzuständen (Quantenphasen). Gemessen und analysiert werden insbesondere der sogenannte Twist-Ordnungsparameter sowie die Korrelationslängen in räumlicher und imaginärer zeitlicher Richtung. Mit Hilfe von Finite-Size Scaling Analysen werden kritische Werte von α , kritische Exponenten sowie führende Korrekturterme ermittelt.

By means of quantum Monte Carlo simulations at low temperatures, the quantum phase transitions in antiferromagnetic Heisenberg spin chains consisting of two different kinds of spin, S_a and S_b , that appear alternatingly in pairs, are investigated for the cases $S_a = 1/2$ and $S_b = 1$, $S_a = 1/2$ and $S_b = 3/2$ as well as $S_a = 1$ and $S_b = 3/2$. Transitions between qualitatively different ground states (quantum phases) are induced by varying the parameter α which is the relative coupling between unlike and like spins. In particular, the so-called twist order parameter as well as spatial and imaginary temporal correlation lengths are measured and analysed. Critical values of α , critical exponents and leading correction terms are extracted by finite-size scaling analysis.

Acknowledgements

I am grateful to Prof. Dr. Wolfhard Janke for support and advice, and especially for offering the opportunity to work in the beautiful city of Leipzig. I also thank Dr. Peter Crompton for discussion and motivation. Special thanks go to Prof. Dr. Hans-Gerd Evertz for advice and supervising this work from afar.

Additionally, I would like to thank all members of the CQT group at the ITP, University of Leipzig, for a good scientific year “abroad”. In particular, I am thankful to Erik Lorenz, Jakob Schluttig, Anna Kallias, Stefan Schnabel, Christoph Junghans and, last but not least, Gil Spiegel for an uplifting working atmosphere.

Moreover, I am grateful to Peter Jessner, Dipl.-Ing. Franz Michel and Ingrid Reiweger for fruitful discussions and motivation back home in Austria.

Finally, I want to thank Heidi Ziegner for priceless mental support and all members of the “Nachtspalter” for making my life in Leipzig not just a scientific one.

Contents

1	Introduction	1
2	Statistical Physics	5
2.1	Partition Function and Physical Observables	5
2.2	Phase Transitions	7
2.3	Quantum–Classical Mapping	10
3	Heisenberg Spin Chains	13
3.1	Spin	14
3.2	Two-Particle Systems	16
3.3	Representing Spins of Higher Magnitude	17
3.4	Uniform and Mixed Spin Chains – Models A , B and C	18
3.4.1	Ground State and Excitations	19
3.4.2	Exact Energy Gap of Small Systems	23
3.4.3	Valence Bond States and Phase Transitions	24
3.5	Observables	27
3.5.1	Twist Order Parameter	27
3.5.2	Dynamic Susceptibilities and Correlation Lengths	28
4	Quantum Critical Phenomena	31
4.1	General Aspects	31
4.2	Quantum Critical Points in Mixed Spin Chains	35
5	Quantum Monte Carlo	37
5.1	Traditional Monte Carlo	38
5.2	Quantum Monte Carlo: Loop Algorithm	39
5.2.1	Discrete Time	39
5.2.2	Continuous Time	43
5.2.3	Measurements and Improved Estimators	45
5.3	Algorithm In Use	46

5.4	Test of the Algorithm	48
5.5	Analysis of Simulational Data	49
5.5.1	Jackknife Method	49
5.5.2	Finite-Size Scaling	50
6	Results of Model B	55
6.1	Twist Order Parameter	55
6.2	Correlation Lengths	61
6.2.1	Imaginary Time Correlation Length at Fixed Temperature	61
6.2.2	Imaginary Time Correlation Length for Fixed Chain Length	64
6.2.3	Spatial Correlation Length	66
6.2.4	Corrections to Scaling and Linearity Check	68
6.3	Staggered Susceptibility	70
6.4	Analysis With Constant Aspect Ratio	73
7	Results of Models A and C	77
7.1	Twist Order Parameter	77
7.2	Correlation Lengths and Susceptibility	80
8	Discussion	85
8.1	Conclusions	85
8.2	Summary and Outlook	89
A	Finite-Size Scaling at Fixed Temperatures	91
	Bibliography	101

List of Tables

1.1	Realisations of quasi one-dimensional spin systems.	4
3.1	Ground state energies of ferro- and antiferromagnetic two-particle systems. . .	17
3.2	Implications of LSM argument for half-odd integer and integer spin chains. . .	22
4.1	Parallels and contrasts between classical and quantum critical points.	34
6.1	Model B – pseudo-critical points of the twist order parameter – fit to finite-size scaling relation without corrections.	59
6.2	Model B – pseudo-critical points of the twist order parameter – fit to finite-size scaling relation with corrections in $1/L$	60
6.3	Model B – pseudo-critical points of the twist order parameter – fit to finite-size scaling relation with corrections in $1/L$ with fixed exponent.	60
6.4	Model B – finite-size scaling fit results of the imaginary time correlation length – β kept fixed.	69
6.5	Model B – finite-size scaling fit results of the imaginary time correlation length – L kept fixed.	69
6.6	Model B – numerical check of linearity of the correlation length estimators – considering error estimates of the peak heights.	70
6.7	Model B – numerical check of linearity of the correlation length estimators – not considering error estimates of the peak heights.	70
6.8	Model B – finite-size scaling fit results of the staggered susceptibility – L kept fixed.	73
6.9	Model B – shift exponent – constant aspect ratio.	75
7.1	Models A and C – pseudo-critical points of the twist order parameter – fit to finite-size scaling relation without corrections.	79
8.1	Comparison of results.	88
8.2	Critical values of the coupling ratio α_c derived from field theoretic investigation compared to results from quantum Monte Carlo.	89

A.1	Model A – ξ_τ – improved second-moment estimator.	92
A.2	Model A – ξ_τ – unimproved second-moment estimator.	93
A.3	Model A – z_L	94
A.4	Model B – ξ_τ – improved second-moment estimator.	95
A.5	Model B – ξ_τ – unimproved second-moment estimator.	96
A.6	Model B – z_L	97
A.7	Model C – ξ_τ – improved second-moment estimator.	98
A.8	Model C – ξ_τ – unimproved second-moment estimator.	98
A.9	Model C – z_L	99
A.10	Model C – z_L	100

List of Figures

3.1	Basis cells of the three different mixed spin chains.	19
3.2	Exact excitation gap of small uniform spin chains.	23
3.3	Exact excitation gap of small mixed spin chains.	24
3.4	Valence bond configurations of basis cells of mixed spin chains.	25
3.5	Valence bond solid configuration of uniform spin chain – $S = 1$	26
3.6	Twist order parameter of small chain lengths.	28
4.1	Low energy spectrum of finite spin chains.	32
4.2	Quantum critical point – example of phase diagrams.	33
5.1	Checkerboard of one-dimensional spin chain.	40
5.2	The three different plaquette types for antiferromagnetic spin chains.	42
5.3	Example of a loop update.	42
5.4	Projector plaquettes.	43
5.5	Plaquette picture of uniform and mixed spin chains.	44
5.6	Illustration of loop building rules in continuous imaginary time.	45
5.7	Loop path for mixed spin chains in continuous imaginary time.	45
5.8	Model B – twist order parameter and excitation gap for $L = 8$ – a test of the algorithm.	49
6.1	Model B – twist order parameter.	56
6.2	Model B – twist order parameter – temperature induced formation of a plateau.	56
6.3	Model B – exact spectrum of the twist order parameter for $L = 8$ and three different values of α	57
6.4	Model B – slope of the twist order parameter at the zero point – temperature and system size dependence.	58
6.5	Model B – temperature and chain length of maximum slope.	58
6.6	Model B – pseudo-critical points determined from the twist order parameter – temperature dependence.	59
6.7	Model B – ξ_τ at fixed β – second-moment estimator.	62

6.8	Model B – ξ_τ at fixed β – fourth-moment estimator.	62
6.9	Model B – ξ_τ at fixed β – finite-size scaling of peak locations.	63
6.10	Model B – ξ_τ at fixed L – second-moment estimator.	64
6.11	Model B – ξ_τ at fixed L – fourth-moment estimator.	64
6.12	Model B – ξ_τ at fixed L – finite-size scaling of peak locations.	65
6.13	Model B – ξ_τ at fixed L – finite-size scaling of peak locations.	65
6.14	Model B – ξ at fixed β – second-moment estimator.	66
6.15	Model B – ξ at fixed L – second-moment estimator.	67
6.16	Model B – ξ – finite-size scaling of peak locations.	68
6.17	Model B – χ_s at fixed β	71
6.18	Model B – χ_s at fixed L	72
6.19	Model B – χ_s – finite-size scaling of peak locations.	72
6.20	Model B – $\xi_{\tau,\text{imp}}^{(2)}$ – constant aspect ratio.	74
6.21	Model B – z_L – constant aspect ratio.	74
7.1	Model A – twist order parameter.	78
7.2	Model C – twist order parameter – left transition.	78
7.3	Model C – twist order parameter – right transition.	78
7.4	Model A – ξ_τ and χ_s	81
7.5	Model A – location of pseudo-critical points.	81
7.6	Model C – ξ_τ	82
7.7	Model C – χ_s	83
7.8	Model C – location of pseudo-critical points.	83
7.9	Model C – peak height of pseudo-critical points.	83
8.1	Schematic picture of twist order parameter at low non-zero temperatures. . . .	86

Chapter 1

Introduction

The mystery of magnetism has been startling from the very beginning of its discovery, its true nature was not unveiled until the development of quantum mechanics. The fascinating insight gained from ideas based on classical models that were inspired by quantum mechanics, or on quantum models, and the rich variety of unexpected effects has kept theorists and experimentalists busy throughout the past decades. Not to forget computationalists who found a prosperous field of research in (quantum) magnetism.

Quantum mechanics showed that it is the fundamental properties of electrons – spin, kinetic energy, Pauli exclusion principle and Coulomb interaction ([1], p. 11) – that give rise to various magnetic manifestations such as ferromagnets (Fe, Co, Ni, Gd) and antiferromagnets (CoO, NiCo, FeO, RbMnFe₃). Despite the fundamental insight originating from quantum mechanics, many properties of magnetic materials in three dimensions can be described by effectively classical models one of which is the classical Heisenberg model that represents spins as classical vectors that can point into any spatial direction. The typical temperature driven transition from a long-range ordered (anti)ferromagnetic phase to a paramagnetic phase can also be modelled by the nearest-neighbour Ising model

$$\mathbf{H} = J \sum_{\langle i,j \rangle} \mathbf{S}_i^z \mathbf{S}_j^z. \quad (1.1)$$

Even though it incorporates a fundamental quantum feature – the discreteness of spin and its z -component – the Ising model obeys classical statistical mechanics, which is why it is often referred to as a “classical” model, with the Ising spins being “classical” variables.

Quantum effects become more apparent in low dimensions, in particular in one-dimensional spin systems. Chains of localised spins are effectively modelled by the quantum Heisenberg Hamiltonian

$$\mathbf{H} = J \sum_{\langle i,j \rangle} \vec{\mathbf{S}}_i \vec{\mathbf{S}}_j. \quad (1.2)$$

For $J < 0$ the nearest-neighbour interaction is ferromagnetic (FM) and spins tend to align par-

allel to each other, while for $J > 0$ it is antiferromagnetic (AF) with anti-parallel alignment of spins. The coupling constant J is determined from the orbital overlap integral. If the two electrons involved occupy the same spatial region but different orthogonal orbitals, the interaction energy will be reduced by parallel alignment of the spins leading to a ferromagnetic coupling constant. For two electrons that occupy non-orthogonal orbitals that are spatially separated, anti-alignment of spins reduces the kinetic energy of the electrons, leading to antiferromagnetic coupling constants.¹

Unlike their FM counterparts, AF chains do not have trivial ground states due to another fundamental quantum feature – the superposition of states. Néel ordered states are not stable as for the mediation between up and down spins measured along the z -axis (for spin $S = 1/2$) by the x - and y -components of the spin operators.

Thus, even though the quantum Heisenberg Hamiltonian in its “pure” form above looks appealingly simple and tame, the interplay of at least three fundamental quantum features – discreteness of spin, superposition of states and Berry phase factors – leads to interesting and exotic effects that include zero temperature quantum phase transitions driven by couplings [2]. The acquisition of a Berry phase factor upon rotation of the z -axis is the origin of a striking difference between uniform half-odd integer and integer spin chains, as first conjectured by Haldane in 1983 [3]. For isotropic and translationally invariant couplings, uniform spin chains are gapless (i.e. critical) for $S = 1/2, 3/2, 5/2, \dots$ and gapped for $S = 1, 2, 3, \dots$

A good deal of theoretical and numerical investigation has been carried out since, to confirm what has become known as Haldane’s conjecture. The ground states of uniform integer spin chains that can be described by the valence bond picture [4] show “liquid Néel order”. Uniform half-odd integer spin chains with translationally invariant coupling are critical and located at a phase boundary that separates different phases that are described by different valence bond configurations that depend on the specific values of coupling constants of bond alternating chains. Analogous critical states (i.e. phase boundaries) can be detected for integer spin chains. The relative coupling ratio, however, is different from unity. Thus, by varying the bond alternation parameter the quantum spin chain can be driven through a quantum critical point.

Field theoretical methods based upon the non-linear σ -model are successfully applied to derive critical theories of quantum spin chains. This thesis, however, will not dive into this vast field. Interested readers will find an extensive field theoretic treatment of critical phenomena in [5]. It is the numerical path that will be chosen in this thesis. Quantum Monte Carlo simulations provide a powerful tool in order to numerically study quantum spin chains. The Loop Algorithm [6, 7] with its continuous imaginary time extension [8, 9] readily implements quantum properties of the Heisenberg Hamiltonian and allows for effective simulation

¹For more detail on the mechanisms, leading to FM or AF couplings see [1], Chapter 2.

of quantum spin chains, in particular, close to quantum critical points.

Complementary to numerical work, experimental verification of Haldane's conjecture became feasible thanks to the synthetisation of organic and inorganic compounds especially in the past decade (see Table 1.1). Linear chains of magnetic ions (e.g. $S = 1/2$: Cu^{++} , Co^{++} ; $S = 1$: Ni^{++} ; $S = 5/2$: Mn^{++}) are hosted in three-dimensional arrangements of non-magnetic molecules or ions that screen the magnetic interchain interaction. Materials in which this interchain interaction is significantly smaller than the intrachain interaction between the magnetic ions are considered to be quasi one-dimensional (Q1D). The examples of chains with $S = 1$ in Table 1.1 show translationally invariant and bond alternating chains, which were mostly tested in neutron scattering experiments to determine the excitation gap and verify that for a certain ratio of bond alternation this gap does indeed vanish. In the first line of Table 1.1 an interesting realisation of a Q1D chain of $S = 1/2$ is given. At temperatures well above $T \approx 14\text{K}$ it shows translationally invariant couplings while below due to spin-phonon interaction it becomes bond alternating with a dimerised ground state. The transition between these two different phases has become known as a spin-Peierls transition.

In this thesis mixed spin chains will be studied with two different types of spin, arranged as $S_a - S_a - S_b - S_b$. The three simplest combinations, including $S = 1/2, 1, 3/2$, are investigated by continuous imaginary time quantum Monte Carlo simulations. No realisations of exactly this spin arrangement are yet known to the author. The mixed spin materials stated in Table 1.1 either show alternating arrangement with period two and have ferrimagnetic ground states [10, 13], or incorporate spins of different kind in the crystal structure between the linear chains. However, the effects of including spins of different magnitude are of great theoretical interest in order to understand the low-temperature properties of antiferromagnetic Heisenberg spin chains. Previous theoretical studies have been carried out by mapping onto the non-linear σ -model for general mixed spin chains [11, 12, 13]. The cases $S_a = 1/2, S_b = 1$ (model **A**) as well as $S_a = 1, S_b = 3/2$ (model **C**) have been numerically investigated before [14] by using the same method and code as in this thesis.

This thesis is organised as follows. In Chapter 2 the basic concepts of statistical physics that are of central importance in this thesis are briefly recapitulated. Chapter 3 presents one-dimensional spin chains in a slightly more detailed fashion. The models under investigation are defined and the valence bond picture that approximately describes different ground states in uniform and mixed spin chains is introduced. In Chapter 4 quantum critical points are discussed briefly. The method of data production and analysis is described in Chapter 5. Results for $S_a = 1/2$ and $S_b = 3/2$ (model **B**) are presented and carefully discussed in Chapter 6. The other two models qualitatively show the same behaviour and corresponding results are therefore only representatively reported in Chapter 7. Finally, discussion and summary are given in Chapter 8.

Table 1.1: List of materials that realise Q1D spin systems. (Notes: * More recently considered to be a spin-ladder system with $S = 1/2$ or approximately a spin chain of $S = 1$, see references given. ** See also references therein.)

Spin Chain	Material	Refs.
$S = 1/2$; invariant/alternating	CuGeO ₃	[15]
$S = 1/2$; FM–AF alternating*	(CH ₃) ₂ CHNH ₃ CuCl ₃	[16, 17, 18]
$S = 1/2$; AF–AF alternating	(CH ₃) ₂ CHNH ₃ CuBr ₃	[16, 19, 20]
$S = 1/2$; FM–AF random alternating	(CH ₃) ₂ CHNH ₃ (Cl _x Br _{1-x})	[16, 20]
$S = 1$; invariant	CsNiCl ₃	[21]
	Ni(C ₂ H ₈ N ₂) ₂ NO ₂ (ClO ₄) (NENP)	[22, 23]
	Ni(C ₅ H ₁₄ N ₂) ₂ N ₃ (ClO ₄) (NDMAZ)	[24, 25]
	Ni(C ₅ H ₁₄ N ₂) ₂ N ₃ (PF ₆) (NDMAP)	[26, 27]
	PbNi ₂ V ₂ O ₈	[28]
	Y ₂ BaNiO ₅	[29, 30]
$S = 1$; alternating	NMAOP	[31, 34]
	NTENP	[32, 34]
	NTEAP	[33, 34]
Mixed Spins; Ni-chains coupled by magnetic rare earths R (e.g. Pr, Tm)	R ₂ BaNiO ₅	[30]**
$S = 1/2, 5/2$; alternating, ferrimagnetic	CuMn(S ₂ C ₂ O ₂) ₂ · 7.5H ₂ O	[35]
$S = 1/2, 1$; alternating, ferrimagnetic	NiCu(pba)(D ₂ O) ₃ · 2D ₂ O	[36]

Chapter 2

Statistical Physics

In this chapter a quick review of the most important statistical physics background will be given. In Section 2.1 the partition function and its relation to physical observables will be presented, and in Section 2.2 we will briefly encounter phase transitions. For detailed insight in this field the interested reader is referred to standard textbooks such as [37, 38, 39, 40] and the references given in the text. In Section 2.3 the important connection between d -dimensional quantum systems and classical systems in $d + 1$ dimensions will be discussed via the imaginary time formalism. For a more detailed discussion of quantum–classical mapping, in particular in the context of quantum phase transitions, [2] is highly recommended. For an introductory study of the imaginary time formalism see for example [41], Chapter 21.

2.1 Partition Function and Physical Observables

For classical systems with constant particle number one is interested in the canonical partition function Z given by

$$Z(\beta) = \sum_i e^{-\beta E_i(H, \dots)}, \quad (2.1)$$

with inverse temperature $\beta = 1/k_B T$, k_B is Boltzmann's constant which we will set to unity for all of our discussion. The sum counts all accessible microstates (microscopic configurations) i weighted with the Boltzmann factor $e^{-\beta E_i(H, \dots)}$. $E_i(H, \dots)$ is the energy of microstate i that usually depends on external parameters such as a magnetic field H . Knowing all possible microstates and the corresponding energies that determine the weights is equivalent to knowing all thermodynamics of the system. Thus, the partition function contains all relevant thermodynamic information.

The macroscopic values of any physical quantity (observable) A and functions of it are given by the mean value over all microscopic values A_i ,

$$\langle f(A) \rangle = \sum_i p_i f(A_i), \quad (2.2)$$

with p_i the probability of microstate i to occur. p_i is given by the corresponding Boltzmann weight, normalised by the partition function,

$$p_i = \frac{1}{Z} e^{-\beta E_i(H, \dots)}. \quad (2.3)$$

At non-zero temperature the system fluctuates around this mean value. The variance σ_A of $f(A) = A$

$$\sigma_A = \langle (\Delta A)^2 \rangle = \langle A^2 \rangle - \langle A \rangle^2, \quad (2.4)$$

with $\Delta A_i = A_i - \langle A \rangle$, is a measure of those fluctuations. The internal energy U of a system is the mean energy of its microscopic configurations,

$$U = \langle E \rangle = \sum_i p_i E_i(H, \dots) = \frac{1}{Z} \sum_i e^{-\beta E_i(H, \dots)} E_i(H, \dots) = -\frac{\partial \ln Z}{\partial \beta}. \quad (2.5)$$

Similarly evaluating (2.2) for the entropy S identifies the free energy $F = U - TS$ as

$$F = -\frac{\ln Z}{\beta}. \quad (2.6)$$

Of particular interest are the first and second derivatives of the free energy with respect to its external parameters T , H . The magnetisation M of a system of volume $V = L^3$ at constant temperature and the corresponding magnetic susceptibility χ are given by

$$VM = -\left(\frac{\partial F}{\partial H}\right)_T, \quad (2.7)$$

$$\chi = \left(\frac{\partial M}{\partial H}\right)_T. \quad (2.8)$$

Using (2.4) for the magnetisation relates its fluctuations to the susceptibility¹

$$\beta \sigma_M = \beta \left(\langle M^2 \rangle - \langle M \rangle^2 \right) = \chi. \quad (2.9)$$

For non-critical systems the variance (2.4) vanishes for large system size and constant particle density V/N like $1/N$. Thus, in experiments far from critical points that approximately realise the thermodynamic limit of $N \rightarrow \infty$, fluctuations cannot be measured and used to determine observables related to it. Computer simulations, however, are naturally restricted to finite and small systems, and fluctuations can readily be used to directly measure for instance first and second derivatives of the free energy ([42], p. 11).

For **quantum problems** the energy in (2.1) must be replaced by the Hamiltonian \mathbf{H} of the system. The partition function then becomes the trace of the quantum statistical canonical

¹Similarly the specific heat at constant magnetic field is linked to fluctuations of the internal energy, $\beta C_H = k_B (\langle E^2 \rangle - \langle E \rangle^2)$.

density operator

$$\begin{aligned}
 Z(\beta) &= \text{Tr} e^{-\beta \mathbf{H}} \\
 &= \sum_n \langle n | e^{-\beta \mathbf{H}} | n \rangle \quad \dots \text{in a discrete basis,} \\
 &= \int_{-\infty}^{\infty} \langle x | e^{-\beta \mathbf{H}} | x \rangle dx \quad \dots \text{in a continuous basis.}
 \end{aligned}
 \tag{2.10}$$

Observables of quantum systems can be calculated by

$$\langle A \rangle = \frac{1}{Z} \text{Tr} \left(e^{-\beta \mathbf{H}} \mathbf{A} \right).
 \tag{2.11}$$

Using the, say discrete, set of normalised eigenvectors of \mathbf{H} (= eigenbasis) we write

$$Z(\beta) = \sum_n e^{-\beta E_n},
 \tag{2.12}$$

where E_n is the eigenvalue of eigenvector $|E_n\rangle$ determined from the eigenvalue equation

$$\mathbf{H} |E_n\rangle = E_n |E_n\rangle.
 \tag{2.13}$$

The crucial part in order to calculate the quantum partition function is the diagonalisation of the Hamiltonian. This is generally a highly nontrivial task for many body problems particularly if there are off-diagonal elements involved.

2.2 Phase Transitions

Let us begin by remembering the ideal classical ferromagnet as a generic and well-known example of a system that undergoes phase transitions (see e.g. [39], p. 21 ff.). Below the critical temperature T_c , the Curie-temperature, the magnetisation will jump (change its sign) if an applied magnetic field is driven through zero. This transition is of first order. Even in zero magnetic field below T_c , the classical ferromagnet in three dimensions develops spontaneous magnetisation, i.e. is ordered, and rotational symmetry is “spontaneously broken”. Raising the temperature will eventually destroy this order at T_c and the system becomes paramagnetic, full rotational symmetry then appears restored. This order–disorder phase transition is of second order. Note that above T_c in systems with continuous and full rotational symmetry no field driven first-order transitions take place and that temperature driven second-order transitions cannot happen for magnetic fields $\neq 0$ in the classical ferromagnet.

A phase transition is called first-order if one of the first derivatives of the free energy with respect to an external parameter changes its value non-analytically (i.e. jumps). The free energy itself then exhibits a kink. This is the case for the classical ferromagnet at $H = 0$. Here, the relevant first derivative is the magnetisation.

A phase transition is referred to as second-order, also called continuous or critical, if the correlation length diverges at some critical value of the control parameter. Usually this is accompanied by the divergence of one of the second derivatives. The name “continuous” comes from the fact that first derivatives do not jump if the second derivatives diverge. Their slope becomes infinite but they remain continuous. The classical ferromagnet–paramagnet transition at T_c is of second order. We will only be interested in this kind of phase transitions, continuous ones, further on.

In many cases, continuous phase transitions are of the order–disorder type. Thus, an order parameter such as the magnetisation can be defined that is non-zero in the ordered and zero in the disordered phase to signal the transition. The disordered phase is not complete chaos but shows short-range order that can be measured by correlation functions. Let us define the connected magnetic two-point spatial correlation function

$$\begin{aligned}\Gamma(r) &= \left\langle \left(m(\vec{r}) - \langle m(\vec{r}) \rangle \right) \left(m(\vec{r}_0) - \langle m(\vec{r}_0) \rangle \right) \right\rangle \\ &= \langle m(\vec{r})m(\vec{r}_0) \rangle - \langle m(\vec{r}) \rangle \langle m(\vec{r}_0) \rangle ,\end{aligned}\tag{2.14}$$

where $m(\vec{r})$ is the magnetisation at position \vec{r} and $r = |\vec{r} - \vec{r}_0|$, with the total magnetisation $M = 1/V \int dV m(\vec{r})$. $\Gamma(r)$ measures the correlation between deviations of the local magnetisation at position \vec{r} from its mean value, i.e. *fluctuations*, and the same deviations at position \vec{r}_0 . In the paramagnetic phase $\langle m(\vec{r}) \rangle \langle m(\vec{r}_0) \rangle$ vanishes, which is why the two-point correlation function very often is also defined just by $C(r) = \langle m(\vec{r})m(\vec{r}_0) \rangle$ (see e.g. [40], Chapter 2). For sufficiently large r , $\Gamma(r)$ will decay exponentially with distance r which defines a correlation length ξ by

$$\Gamma(r) \sim \exp\left(-\frac{r}{\xi}\right).\tag{2.15}$$

The correlation length will grow if the system approaches the critical point T_c from the disordered phase. At $T = T_c$, $\xi = \infty$ and the correlation function still decreases but with an inverse power of distance,

$$\Gamma(r) \sim \frac{1}{r^{d-2+\eta}},\tag{2.16}$$

with d the dimension and η a critical exponent. For $d = 3$, η controls the deviation from the usual $1/r$ decay. Equations (2.15) and (2.16) are expressed in the more general relation

$$\Gamma(r) = \frac{1}{r^{d-2+\eta}} \tilde{\Gamma}(r/\xi).\tag{2.17}$$

This relation was originally justified by phenomenological extension of mean-field results but can be proven within the context of renormalisation group theory which we will not utter here (see e.g. [37], Chapter 7). It reflects that, close to the critical point, ξ is the only relevant length scale, and with diverging ξ the system becomes self-similar at all length scales. In the vicinity of T_c the divergence of ξ is asymptotically described by a power-law growth,

$$\xi(T) \sim \left(1 - \frac{T}{T_c}\right)^{-\nu} \quad \text{for } T \geq T_c,\tag{2.18}$$

with ν the critical exponent of the correlation length. Similarly other diverging quantities show power-law behaviour

$$A(T) \sim \left| 1 - \frac{T}{T_c} \right|^{-\varrho_A}, \quad (2.19)$$

with different critical exponents ϱ_A for different observables. Proportionality constants are generally different below and above the transition. The exponents ϱ_A are usually labelled α for the specific heat, $-\beta$ for the magnetisation, γ for the susceptibility and δ for the critical isotherm. These, however, are not completely independent from each other but can be related through scaling relations,

$$\begin{aligned} \alpha &= 2 - 2\beta - \gamma, \\ \beta &= \frac{2 - \alpha}{\delta + 1}, \\ \gamma &= \nu(2 - \eta), \\ \nu &= \frac{2 - \alpha}{d}, \end{aligned} \quad (2.20)$$

where the last two lines are so-called hyper-scaling relations.

ξ is the characteristic length scale at which fluctuations occur. With ξ getting larger and larger as T_c is approached, fluctuations grow. Microscopic details such as the specific form of short-range interactions do not play a dominant role anymore, and the behaviour of the system only depends on true long-range characteristics such as dimension and symmetries. Phase transitions in different systems that have the same dimension and symmetries thus will show the same universal critical exponents, i.e. they fall into the same universality class.

Real singularities of phase transitions only occur in the thermodynamic limit of infinite system size. Finite samples (e.g. in the context of computer simulations) show analytic behaviour of all thermodynamic quantities. The singularities are smoothed out. Critical points are then, in fact, pseudo-critical points usually defined by a peak. The reader is to bear this in mind as we will very often talk about finite systems in the next chapters. To gather information about infinite systems from finite-size data is an important task that will be presented in Section 5.5.2.

Only few models can be solved to determine critical exponents exactly. The most famous example is the Ising model in two dimensions where the exact solution yields $\nu = 1$, $\eta = 0.25$, $\beta = 1/8$ and $\gamma = 7/4$ (see e.g. [38], Chapter 5, and the references therein). Experimental and numerical investigations provide further estimates of exponents of phase transitions in various systems and models. Some examples are:

- 3D Ising model: Field theoretic studies give $\nu = 0.6300(15)$, $\eta = 0.031(4)$, $\beta = 0.3250(15)$ and $\gamma = 1.241(2)$ [43].
- 3D classical Heisenberg model (Spin $S \rightarrow \infty$): Field theoretic studies give $\nu = 0.705(3)$,

$\eta = 0.033(4)$, $\beta = 0.3645(25)$ and $\gamma = 1.386(4)$ [43], compared with $\nu = 0.7048(30)$, $\gamma = 1.3873(85)$ [44] and $\eta = 0.0271(17)$, $\beta = 0.362(4)$ [45, 46] from Monte Carlo simulations.

- Spin $S = 1/2$ Heisenberg model: $\gamma \approx 1.41 - 1.51$ from series expansions [47].
- Inhomogeneous ferromagnets: $\beta = 0.3682(33)$ from experiments [48].
- 3D XY-model: Combined Monte Carlo and high-temperature expansions give $\nu = 0.67155(27)$, $\eta = 0.0380(4)$, $\alpha = -0.0146(8)$, $\beta = 0.3485(2)$ and $\gamma = 1.3177(5)$ [49], whereas Monte Carlo studies based on the complex $|\Phi|^4$ -model yield $\nu = 0.670(3)$ and following from ν , $\alpha = -0.010(9)$ [50]. Earth orbit experiments with superfluid ^4He give $\alpha = 0.0127(1)$ and therefore following from α , $\gamma = 0.6709(1)$ [51, 52].

2.3 Quantum–Classical Mapping

We have seen that the partition function of a quantum system is the trace of the quantum statistical operator. This actually also applies to classical systems. It just happens that a “classical” Hamiltonian is fully diagonal in a “classical” basis from the start, and thus, the trace turns into the partition function known from classical statistical mechanics.

Lattice spin systems are quantum systems. To perform the trace, we use as a basis of all many particle states the set of vectors $\{|\phi_i\rangle\}$ that contains all possible configurations where each spin has a defined discrete value

$$|\phi_i\rangle = |(S_1, m_1), (S_2, m_2), \dots, (S_N, m_N)\rangle_i, \quad (2.21)$$

where S_j is the size of spin at site j that can take the values $m_j = S_j, S_j - 1, \dots, -S_j$. N is the total number of spins. The discrete set of values for m_j is a fundamental quantum feature of particles that carry spin².

Generally one is not as lucky as to deal with diagonal spin Hamiltonians. Off-diagonal elements introduce another fundamental quantum feature. The eigenstates $|E_n\rangle$ of the Hamiltonian \mathbf{H} are no longer pure classical states that can simply be described by (2.21), but superpositions of those,

$$|E_n\rangle = \sum_i c_i^{(n)} |\phi_i\rangle. \quad (2.22)$$

The sum runs over the full set of basis vectors. The square of the coefficients’ absolute value $|c_i^{(n)}|^2$ gives the probability of finding a configuration defined by $|\phi\rangle_i$ in a measurement.

This superposition of classical states introduces a new kind of “quantum degree of freedom” that implies the need of an additional artificial dimension if one wants to keep working in a classical basis. The fact that computers, so far, cannot represent superpositions of variables

²A more detailed presentation of quantum spin systems will be given in the following chapter.

makes it clear that the task to map d -dimensional quantum systems onto systems with classical variables in $d + 1$ dimensions is of high relevance for computer simulations.

A way to realize this quantum-classical mapping is provided by the quantum statistical operator itself. $e^{-\beta\mathbf{H}}$ looks strikingly similar to the real time evolution operator $e^{-\frac{i}{\hbar}\mathbf{H}t}$. Indeed, it can be interpreted as “evolution” operator that evolves states in an imaginary time direction defined by $\tau = \beta\hbar$ which immediately introduces the needed additional dimension. The terms in the sum of the quantum partition function (2.10),

$$\langle n | e^{-\beta\mathbf{H}} | n \rangle = \langle n(0) | n(\tau) \rangle , \quad (2.23)$$

are imaginary time transition amplitudes over closed paths, i.e. the probability (if $|n\rangle$ is normalised) of the imaginary time evolved state $|n(\tau)\rangle = e^{-\beta\mathbf{H}} |n\rangle$ again to be in state $|n(0)\rangle = |n\rangle$ after time τ . At $\beta = \infty$ ($T = 0$) the quantum statistical operator projects onto the ground state. This corresponds to infinite imaginary time evolution at the “end” of which any initial state will be evolved into the ground state if it was not orthogonal to it from start. Thus, only those states of the basis $|n\rangle$ that are not orthogonal to the ground state will contribute to the partition function for $\beta \approx \infty$. Note that if $|n\rangle$ is an eigenvector of \mathbf{H} , it will trivially not change throughout the entire evolution. Instead, if the classical basis (2.21) is used we will readily observe interesting imaginary time evolution.

Spins are correlated in imaginary time. This can be expressed by defining the spin correlation function along τ analogously to correlation functions along space directions (see [2], p. 19 f)

$$\Gamma_i(\tau) = \frac{1}{Z} \text{Tr} \left(e^{-\beta\mathbf{H}} \mathbf{S}_i^z(\tau) \mathbf{S}_i^z(0) \right) - \langle \mathbf{S}_i^z(\tau) \rangle \langle \mathbf{S}_i^z(0) \rangle . \quad (2.24)$$

$\mathbf{S}_i^z(\tau) = e^{\mathbf{H}\tau} \mathbf{S}_i^z(0) e^{-\mathbf{H}\tau}$ is the imaginary time evolved z -component of the spin operator $\vec{\mathbf{S}}_i$ at site i . We will simply write \mathbf{S}_i^z for $\mathbf{S}_i^z(0)$. We insert complete sets of eigenstates of \mathbf{H} to obtain

$$\begin{aligned} \Gamma_i(\tau) &= \frac{1}{Z} \sum_{m,n} e^{-\beta E_m} e^{(E_m - E_n)\tau} |\langle E_m | \mathbf{S}_i^z | E_n \rangle|^2 - \langle \mathbf{S}_i^z \rangle^2 \\ &= \frac{2}{Z} \sum_{m,n} e^{-\frac{\beta}{2}(E_m + E_n)} \cosh \left((E_m - E_n) \left(\tau - \frac{\beta}{2} \right) \right) |\langle E_n | \mathbf{S}_i^z | E_m \rangle|^2 - \langle \mathbf{S}_i^z \rangle^2 . \end{aligned} \quad (2.25)$$

$\langle E_n | \mathbf{S}_i^z | E_m \rangle$ is the matrix element $\{\mathbf{S}_i^z\}_{m,n}$ in the eigenbasis of \mathbf{H} . Taking the limit $\beta \rightarrow \infty$ gives

$$\begin{aligned} \lim_{\beta \rightarrow \infty} \Gamma_i(\tau) &= \sum_m e^{-(E_m - E_0)\tau} |\langle E_0 | \mathbf{S}_i^z | E_m \rangle|^2 \\ &\approx e^{-\Delta\tau} |\langle E_0 | \mathbf{S}_i^z | E_1 \rangle|^2 , \end{aligned} \quad (2.26)$$

if the ground state expectation value of the z -component of spin is zero, with $\Delta = E_1 - E_0$, the energy difference in the asymptotically dominant term. The simple form of (2.26) is valid when the ground state and the first excited state are non-degenerate and when there is another finite

gap to the next excited state. Higher energy differences can then be neglected for sufficiently large τ , as they will certainly decrease faster. This means, at $T = 0$, that the asymptotic form of the temporal two-point correlation function is determined by Δ , the energy gap between ground state and first excited state,

$$\Gamma_i(\tau) \sim e^{-\Delta \cdot \tau}. \quad (2.27)$$

This gives, as important result of quantum–classical mapping, the relation between excitation gap of the d -dimensional quantum spin system and imaginary time correlation length of the $(d + 1)$ -dimensional classical system at $T = 0$:

$$\xi_\tau = \frac{1}{\Delta}. \quad (2.28)$$

We note from (2.25) that correlations begin to grow again for $\tau > \beta/2$, which naturally reflects the periodic boundary conditions in imaginary time imposed by the trace in the partition function.

Chapter 3

Heisenberg Spin Chains

In 1928 during his professorship in Leipzig, W. Heisenberg proposed to study localised electrons that interact only pairwise through exchange couplings as a model explanation of ferromagnetism [54]. This is reflected in what is now called “Heisenberg model” (HM). It serves as a fundamental model for quantum magnetism, superconductivity and charge wave densities. The *antiferromagnetic* Heisenberg model (AFHM) furthermore provides an effective Hamiltonian for Mott insulators. This chapter will partly follow [1] where, among other topics, an introduction of the Heisenberg model, its relation to other models, and various applications can be found.

A general Heisenberg Hamiltonian for uniform spins in zero magnetic field is

$$\mathbf{H} = \sum_{\langle i,j \rangle} J_x \mathbf{S}_i^x \mathbf{S}_j^x + J_y \mathbf{S}_i^y \mathbf{S}_j^y + J_z \mathbf{S}_i^z \mathbf{S}_j^z, \quad (3.1)$$

where \mathbf{S}_i^α are the components of the quantum spin operator $\vec{\mathbf{S}}$ with spin S at site i , with $S(S+1)$ the eigenvalues of $\vec{\mathbf{S}}^2$. J_α is the coupling constant for the α -component of the spin, and translational invariance of J_α has been assumed. $\langle i, j \rangle$ indicates that the summation is over nearest-neighbour pairs of spin only. For $J_x = J_y = 0$ the above model becomes the Ising model, for $J_z = 0$ it is called XY model and for $J_x = J_y = J_\perp$, XXZ model. We will be concerned with isotropic, antiferromagnetic spin interactions,

$$\mathbf{H} = J \sum_{\langle i,j \rangle} \vec{\mathbf{S}}_i \cdot \vec{\mathbf{S}}_j, \quad (3.2)$$

where $J_x = J_y = J_z = J \geq 0$.

In the following two sections the spin operators and their matrix representations in order to construct two-particle and many-body spin Hamiltonians will be presented. Spins of higher magnitude will then be represented by subspins of $S = 1/2$ in Section 3.3. Uniform and mixed spin chains will be introduced in Section 3.4, together with the valence bond picture to describe ground state properties and quantum phase transitions between qualitatively different ground

states. Finally, in Section 3.5 observables of spin chains that are of central importance in this thesis will be described. For general background of quantum mechanics see for example [41].

3.1 Spin

Spin, an intrinsic feature of quantum particles, is associated with classical angular momentum, but unlike its classical counterpart the orientation of spins cannot point everywhere in space. The orientation is quantised and can only take on $2S+1$ discrete values $m = -S, -S+1, \dots, +S$ along one arbitrary quantisation direction.

The spin operator $\vec{\mathbf{S}}_S = (\mathbf{S}_S^x, \mathbf{S}_S^y, \mathbf{S}_S^z)$ of spin size S is a three component vector operator. The matrix elements of \mathbf{S}_S^α in the usual representation where the z -axis is chosen to be the quantisation direction are given by

$$\begin{aligned} \langle S, m' | \mathbf{S}_S^x | S, m \rangle &= \frac{\hbar}{2} \left(\sqrt{S(S+1) - m(m+1)} \cdot \delta_{m', m+1} \right. \\ &\quad \left. + \sqrt{S(S+1) - m(m-1)} \cdot \delta_{m', m-1} \right), \\ \langle S, m' | \mathbf{S}_S^y | S, m \rangle &= \frac{\hbar}{2i} \left(\sqrt{S(S+1) - m(m+1)} \cdot \delta_{m', m+1} \right. \\ &\quad \left. - \sqrt{S(S+1) - m(m-1)} \cdot \delta_{m', m-1} \right), \\ \langle S, m' | \mathbf{S}_S^z | S, m \rangle &= \hbar m \delta_{m', m}. \end{aligned} \quad (3.3)$$

Here, $|S, m\rangle$ is the single particle state from the many-body Ising basis (2.21), \hbar is Planck's constant which will be set to unity further on. \mathbf{S}_S^z is diagonal and all states of basis (2.21) are its eigenvectors. \mathbf{S}_S^x and \mathbf{S}_S^y have non-zero off-diagonal elements and thus mediate between states of different orientation m . This is better reflected by introducing raising and lowering spin operators,

$$\begin{aligned} \mathbf{S}_S^+ &= \mathbf{S}_S^x + i\mathbf{S}_S^y, \\ \mathbf{S}_S^- &= \mathbf{S}_S^x - i\mathbf{S}_S^y. \end{aligned} \quad (3.4)$$

The action of \mathbf{S}_S^\pm on a spin state $|S, m\rangle$ is

$$\mathbf{S}_S^\pm |S, m\rangle \sim \begin{cases} |S, m \pm 1\rangle & \text{for } m \neq \pm S \\ 0 & \text{for } m = \pm S. \end{cases} \quad (3.5)$$

All spin operators obey the following commutation relations:

$$\begin{aligned} [\mathbf{S}_S^\alpha, \mathbf{S}_S^\beta] &= i\varepsilon_{\alpha\beta\gamma} \mathbf{S}_S^\gamma, \\ [\mathbf{S}_S^z, \mathbf{S}_S^\pm] &= \pm \mathbf{S}_S^\pm, \\ [\mathbf{S}_S^+, \mathbf{S}_S^-] &= 2\mathbf{S}_S^z, \\ [\vec{\mathbf{S}}_S^2, \mathbf{S}_S^\pm] &= 0, \end{aligned} \quad (3.6)$$

where $\varepsilon_{\alpha\beta\gamma}$ is the antisymmetric tensor which is 1 for even permutations of $\alpha\beta\gamma$ and -1 for odd permutations.

For the special case of $S = 1/2$ the spin operators can be expressed in the $\mathbf{S}_{1/2}^z$ -basis as $\mathbf{S}_{1/2}^\alpha = \frac{1}{2}\sigma^\alpha$, with the Pauli matrix representation

$$\sigma^x = \begin{pmatrix} 0 & 1 \\ 1 & 0 \end{pmatrix}, \quad \sigma^y = \begin{pmatrix} 0 & -i \\ i & 0 \end{pmatrix}, \quad \sigma^z = \begin{pmatrix} 1 & 0 \\ 0 & -1 \end{pmatrix}. \quad (3.7)$$

Raising and lowering operators are

$$\mathbf{S}_{1/2}^+ = \begin{pmatrix} 0 & 1 \\ 0 & 0 \end{pmatrix}, \quad \mathbf{S}_{1/2}^- = \begin{pmatrix} 0 & 0 \\ 1 & 0 \end{pmatrix}. \quad (3.8)$$

For $S = 1$ and $S = 3/2$, the \mathbf{S}_S^\pm in matrix representation are

$$\begin{aligned} \mathbf{S}_1^+ &= \begin{pmatrix} 0 & \sqrt{2} & 0 \\ 0 & 0 & \sqrt{2} \\ 0 & 0 & 0 \end{pmatrix}, & \mathbf{S}_1^- &= \begin{pmatrix} 0 & 0 & 0 \\ \sqrt{2} & 0 & 0 \\ 0 & \sqrt{2} & 0 \end{pmatrix}, \\ \mathbf{S}_{3/2}^+ &= \begin{pmatrix} 0 & \sqrt{3} & 0 & 0 \\ 0 & 0 & 2 & 0 \\ 0 & 0 & 0 & \sqrt{3} \\ 0 & 0 & 0 & 0 \end{pmatrix}, & \mathbf{S}_{3/2}^- &= \begin{pmatrix} 0 & 0 & 0 & 0 \\ \sqrt{3} & 0 & 0 & 0 \\ 0 & 2 & 0 & 0 \\ 0 & 0 & \sqrt{3} & 0 \end{pmatrix}. \end{aligned} \quad (3.9)$$

Many particle states such as the Ising basis states (2.21) are direct products of single particle states

$$|\phi\rangle = |(S_1, m_1), (S_2, m_2), \dots, (S_N, m_N)\rangle = |S_1, m_1\rangle_1 \otimes |S_2, m_2\rangle_2 \otimes \dots \otimes |S_N, m_N\rangle_N. \quad (3.10)$$

Single particle operators act, of course, only on the corresponding single particle part of many particle states

$$\mathbf{S}_i |\phi\rangle = \mathbb{1} |S_1, m_1\rangle_1 \otimes \dots \otimes \mathbf{S}_i |S_i, m_i\rangle_i \otimes \dots \otimes \mathbb{1} |S_N, m_N\rangle_N, \quad (3.11)$$

where \mathbf{S}_i can be any operator acting on particle i , and $\mathbb{1}$ denotes unit operators \mathbf{S}_i .

3.2 Two-Particle Systems

Two-particle problems are of central importance in this thesis, in particular the case $S_1 = S_2 = 1/2$. For simulational purposes all many-body Hamiltonians will be reduced to repeated two-particle interactions in Chapter 5. Furthermore, in the following section we will see how spins of size $S \geq 1$ can be decomposed into subspins with $S = 1/2$, thus ending up with the simplest two-particle interaction Heisenberg Hamiltonian. In terms of raising and lowering operators, the Hamiltonian (3.2) for two particles reads

$$\mathbf{H}_{12} = J\vec{\mathbf{S}}_1 \cdot \vec{\mathbf{S}}_2 = J \left(\mathbf{S}_1^z \mathbf{S}_2^z + \frac{1}{2} (\mathbf{S}_1^+ \mathbf{S}_2^- + \mathbf{S}_1^- \mathbf{S}_2^+) \right). \quad (3.12)$$

The Ising basis contains four vectors:

$$|\uparrow\uparrow\rangle, |\uparrow\downarrow\rangle, |\downarrow\uparrow\rangle, |\downarrow\downarrow\rangle, \quad (3.13)$$

where \uparrow (\downarrow) stands for $m = +1/2$ ($-1/2$). We will from now on omit the quantum number S in state vectors as well as the subscript of spin operators and only remember it where it seems necessary. In this basis the Hamiltonian has the following matrix representation:

$$\mathbf{H} = \frac{J}{4} \begin{pmatrix} 1 & 0 & 0 & 0 \\ 0 & -1 & 2 & 0 \\ 0 & 2 & -1 & 0 \\ 0 & 0 & 0 & 1 \end{pmatrix}. \quad (3.14)$$

Diagonalisation gives the set of eigenvectors and energies:

$$\begin{aligned} E_{1,2,3} = \frac{J}{4} : \quad & |E_1\rangle = |\uparrow\uparrow\rangle, \\ & |E_2\rangle = \frac{1}{\sqrt{2}} (|\uparrow\downarrow\rangle + |\downarrow\uparrow\rangle), \\ & |E_3\rangle = |\downarrow\downarrow\rangle, \\ E_4 = -\frac{3J}{4} : \quad & |E_4\rangle = \frac{1}{\sqrt{2}} (|\uparrow\downarrow\rangle - |\downarrow\uparrow\rangle). \end{aligned} \quad (3.15)$$

It follows that for $J < 0$ the system is ferromagnetic with threefold degenerate ground state that correspond to three possible orientations of total spin $S_{\text{tot}} = S_1 + S_2 = 1$. For $J > 0$ it is antiferromagnetic with a unique singlet ground state that has total spin $S_{\text{tot}} = S_1 - S_2 = 0$.

Similarly, \mathbf{H} can be constructed for any two-spin system of arbitrary spin size S_1 and S_2 . The dimension of the matrix will be $(2S_1 + 1)(2S_2 + 1)$. For ferromagnetic coupling the ground state will be $(S_1 + S_2)$ -fold degenerate with maximally possible total spin, while in the antiferromagnetic case the ground state degeneracy will be $|S_1 - S_2|$ with minimally possible total spin. The energies of the two cases for the six simplest two-particle systems are listed in Table 3.1.

Table 3.1: Energies of ferromagnetic (FM) and antiferromagnetic (AF) ground states of the six simplest two-particle Hamiltonians, $\mathbf{H} = J\mathbf{S}_1\mathbf{S}_2$. Values are given in units of J , the coupling strength.

$\mathbf{S}_1 - \mathbf{S}_2 :$	$\frac{1}{2} - \frac{1}{2}$	$\frac{1}{2} - 1$	$\frac{1}{2} - \frac{3}{2}$	$1 - 1$	$1 - \frac{3}{2}$	$\frac{3}{2} - \frac{3}{2}$
FM	$\frac{1}{4}$	$\frac{1}{2}$	$\frac{3}{4}$	1	$\frac{3}{2}$	$\frac{9}{4}$
AF	$-\frac{3}{4}$	-1	$-\frac{5}{4}$	-2	$-\frac{5}{2}$	$-\frac{15}{4}$

3.3 Representing Spins of Higher Magnitude

We will now show how a spin of size S can be represented by $2S$ subspins of site $1/2$. In Chapter 5 we will see how correspondingly computer simulations of spin chains with $S_i \geq 1$ can be implemented by using subspins [55, 56]. Section 3.4 introduces singlet couplings [4] between subspins in order to describe antiferromagnetic ground state properties.

A state $|n\rangle$ of $2S$ subspins is

$$|n\rangle = |m_1, m_2, \dots, m_{2S}\rangle, \quad (3.16)$$

where $m_i = \pm 1/2$ gives the orientation of subspin i . The new basis consists of 2^{2S} states and is thus larger than the original one with $2S + 1$ states. This is clearly due to the fact that $2S$ spins of size $s = 1/2$ can also couple to form states of total spin $s_{\text{tot}} < S$. As these states do not serve our purpose to represent spins of size S , they need to be projected out. This is done by the symmetrisation operator [56],

$$\mathbf{P} = \frac{1}{n_{\mathbf{P}}} \sum_{\alpha=0}^{n_{\mathbf{P}}-1} \mathbf{X}_{\alpha}, \quad (3.17)$$

where $\{\mathbf{X}_i\}$ is the complete set of all possible permutations of the spins in a basis vector, with $\mathbf{X}_0 = \mathbb{1}$. $n_{\mathbf{P}} = (2S)!/n_+!n_-!$ is the number of possible permutations of basis vectors with $2S$ subspins of which n_{\pm} have $m = \pm 1/2$. This prefactor $1/n_{\mathbf{P}}$ on the one hand accounts for the normalisation $1/\sqrt{n_{\mathbf{P}}}$ of a symmetrised basis state $\mathbf{P}|n\rangle$, and on the other hand for its multiplicity as $\mathbf{P}|n\rangle$ will appear $n_{\mathbf{P}}$ times in the basis set giving another $1/\sqrt{n_{\mathbf{P}}}$. The matrix elements of \mathbf{P} are

$$\langle m'_1, m'_2, \dots, m'_{2S} | \mathbf{P} | m_1, m_2, \dots, m_{2S} \rangle = \frac{1}{n_{\mathbf{P}}} \delta_{n'_+, n_+}, \quad (3.18)$$

where n'_+ (n_+) is the total number of spins with $m = +1/2$ in the state $\langle m'_1, m'_2, \dots, m'_{2S} |$ ($|m_1, m_2, \dots, m_{2S}\rangle$). For, e.g., $S = 1$ there are two subspins. Choosing the two-particle basis (3.13) the matrix form of \mathbf{P} is

$$\mathbf{P} = \begin{pmatrix} 1 & 0 & 0 & 0 \\ 0 & \frac{1}{2} & \frac{1}{2} & 0 \\ 0 & \frac{1}{2} & \frac{1}{2} & 0 \\ 0 & 0 & 0 & 1 \end{pmatrix}, \quad (3.19)$$

with $\mathbf{P}^2 = \mathbf{P}$ and $\text{Tr } \mathbf{P} = 3 = 2S + 1$ as desired. Spin operators are now decomposed into subspin contributions, to be applied on the projected space

$$\vec{\mathbf{S}} = \vec{\mathbf{s}}_{\text{tot}} = \sum_{i=1}^{2S} \vec{\mathbf{s}}_i, \quad (3.20)$$

and the expectation values of total spin and its component in quantisation direction for the symmetrised basis states are

$$\langle m_1, m_2, \dots, m_{2S} | \vec{\mathbf{S}}^2 \mathbf{P} | m_1, m_2, \dots, m_{2S} \rangle = \frac{1}{n_{\mathbf{P}}} S(S+1), \quad (3.21)$$

$$\langle m_1, m_2, \dots, m_{2S} | \mathbf{S}^z \mathbf{P} | m_1, m_2, \dots, m_{2S} \rangle = \frac{1}{n_{\mathbf{P}}} (n_+ - n_-). \quad (3.22)$$

Note that $[\mathbf{P}, \mathbf{S}^z] = [\mathbf{P}, \vec{\mathbf{S}}^2] = 0$ and $\mathbf{P}^2 = \mathbf{P}$, and therefore it is sufficient to project only once. The two-particle Hamiltonian (3.12) for two large spins S_1 and S_2 becomes the sum of pairwise interacting subspin parts on the projected space

$$\mathbf{H}_{12} = J \left(\sum_{i=1}^{2S_1} \vec{\mathbf{s}}_{i,1} \right) \left(\sum_{j=1}^{2S_2} \vec{\mathbf{s}}_{j,2} \right), \quad (3.23)$$

such that

$$Z = \text{Tr} \left(e^{-\beta \mathbf{H}_{12} \mathbf{P}} \right), \quad (3.24)$$

where the trace has to be performed using the subspin basis.

3.4 Uniform and Mixed Spin Chains – Models A, B and C

The Hamiltonian (3.2) can be readily generalised to chains of different kinds of spin. We will refer to those as mixed or inhomogeneous spin chains, whereas the former will be called uniform or homogeneous. Out of the huge variety of mixed spin chains imaginable we will specialise to three models which are represented by

$$\mathbf{H} = \sum_{i=0}^{L/4} J_1 \vec{\mathbf{S}}_{4i+1}^{S_a} \vec{\mathbf{S}}_{4i+2}^{S_a} + J_2 \vec{\mathbf{S}}_{4i+2}^{S_a} \vec{\mathbf{S}}_{4i+3}^{S_b} + J_1 \vec{\mathbf{S}}_{4i+3}^{S_b} \vec{\mathbf{S}}_{4i+4}^{S_b} + J_2 \vec{\mathbf{S}}_{4i+4}^{S_b} \vec{\mathbf{S}}_{4i+5}^{S_a}, \quad (3.25)$$

where the superscripts S_a and S_b denote the two kinds of spin involved, with $(S_a = 1/2, S_b = 1)$, $(S_a = 1/2, S_b = 3/2)$ and $(S_a = 1, S_b = 3/2)$ which will further be called models **A**, **B** and **C**, respectively. J_1 is the coupling constant between like spins and J_2 between spins of different size. The basis cells of all models are shown in Fig. 3.1. We choose J_1 as energy scale to introduce the dimensionless coupling ratio $\alpha = J_2/J_1$. Definition (3.25) then turns into

$$\mathbf{H} = \sum_{i=0}^{L/2} \vec{\mathbf{S}}_{2i+1} \vec{\mathbf{S}}_{2i+2} + \alpha \vec{\mathbf{S}}_{2i+2} \vec{\mathbf{S}}_{2i+3}. \quad (3.26)$$

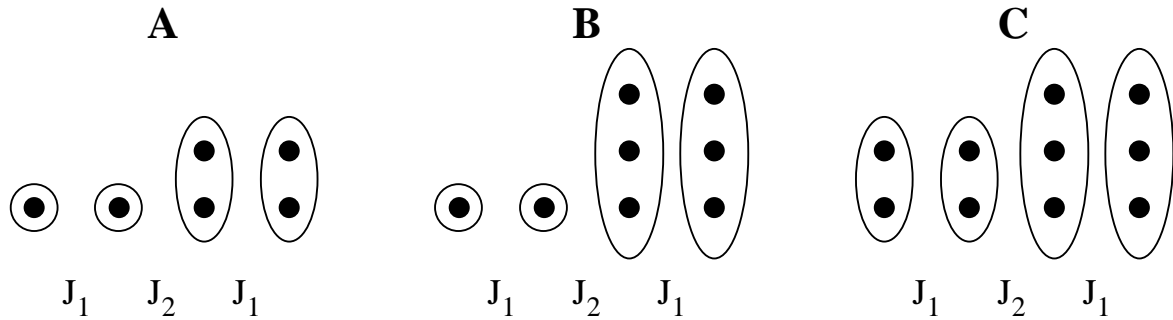


Figure 3.1: Basis cells of the three different mixed spin chains **A**, **B** and **C**. *Filled circles* denote subspins of size $s = 1/2$. J_1 and J_2 indicate the coupling parameters that control the corresponding interaction.

Here we assume the proper spin operator to be applied at each site. Generally, in all of our discussion of uniform and mixed spin chains, periodic boundary conditions will be used. For $S_a = S_b$ we end up with bond-alternating uniform spin chains with alternation parameter α .

Models **A**, **B** and **C** serve as the simplest possible testing ground that includes mixed spins to investigate a certain type of quantum phase transition. The arrangement $S_a - S_a - S_b - S_b$ ensures antiferromagnetic ground states. For alternatingly arranged spin types the ground state would be ferrimagnetic [10, 13]. Therefore, we end up with a Hamiltonian that has broken translational symmetry, yet this symmetry is retained with period 4 (one basis cell). Full rotational symmetry, however, which is typical for the isotropic Heisenberg model is still present.

3.4.1 Ground State and Excitations

Ground state and low-lying excited states are of obvious interest in the low temperature regime. Unlike the FM case, the AF ground state does not exhibit trivial long range order in one dimension. For $S = 1/2$, the classical Néel state ($|\uparrow\downarrow\uparrow\downarrow\dots\rangle$) which does minimise the magnetisation, is not an eigenvector of the Heisenberg Hamiltonian. Take the simple AF-chain with $S = 1/2$ as an example. Its ground state energy can be calculated exactly via the Bethe Ansatz [57, 58, 59]. The energy per site, e_A , in the thermodynamic limit is

$$e_A = J\left(\frac{1}{4} - \ln 2\right). \quad (3.27)$$

The ground state is unique with full rotational symmetry and total magnetisation $m_{\text{tot}} = 0$. In contrast, the energy expectation value of the Néel state is $-J/4$ which is significantly higher. In the thermodynamic limit the spectrum of the uniform antiferromagnetic chain with $S = 1/2$ is continuous, gapless and bounded by

$$\frac{e - e_A}{J} = \begin{cases} \frac{\pi}{2} J |\sin q| & \text{lower bound} \\ \pi J \left|\sin \frac{q}{2}\right| & \text{upper bound,} \end{cases} \quad (3.28)$$

where q is the wave number of the excited state relative to the wave number of the AF ground state. The elementary excitations of spin chains are *quasiparticles* called spinons. These appear pairwise and can be interpreted as moving domain boundaries between Néel ordered phases with momentum q , where $q = k_1 + k_2$ the sum of spinon momenta. The lower boundary shows that for $q = 0, \pi$ there are gapless excitations.

So, even for the simplest antiferromagnetic Heisenberg chain things turn out to be more complicated than the simplicity of its Hamiltonian might tempt to expect. Models with larger spin or higher dimensions are not exactly solved. Even numeric exact diagonalisation of models with larger spins quickly becomes impossible due the fast growing dimensionality of the problem. There are, however, a few strict theorems on what the ground state must look like that apply to models on bipartite lattices. A bipartite lattice can be separated into two sublattices A and B where each site of lattice A only couples to sites that belong to lattice B and vice-versa. One-dimensional chains with nearest-neighbour interaction are trivially always bipartite lattices.

The following theorems and their proofs are given in [1]¹. The proofs make use of a rotation of coordinates on one of the two sublattices:

$$\begin{aligned} \mathbf{S}_i^z &\rightarrow \mathbf{S}_i^z, \\ \mathbf{S}_i^+ &\rightarrow -\mathbf{S}_i^+, \\ \mathbf{S}_i^- &\rightarrow -\mathbf{S}_i^-, \end{aligned} \tag{3.29}$$

where all sites i belong to one of the two sublattices, A or B . They apply to uniform spin chains but can be generalised to mixed chains with no special effort as will shown immediatly. This generalisation, however, does yet not appear to exist in the literature.

Marshall's sign criterion states that at fixed magnetisation M for the lowest energy state

$$\begin{aligned} |\Psi_0^M\rangle &= \sum_n (-1)^{\Gamma_n} f_n^M |\phi_n\rangle, \\ \Gamma_n &= \sum_{i \in B} (S_i + m_i)_n, \end{aligned} \tag{3.30}$$

holds, B denotes one of the two sublattices. $(\dots)_n$ indicates that S_i and m_i are taken from basis state $|\phi_n\rangle$. $f_n^M \geq 0$ can always be chosen. The only “effort” to generalise the above theorem to mixed spin chains was to replace S in the original proof by S_i in order to consider the different size of spin at each site. This theorem states that for given magnetisation M the state with the lowest energy is always the one with the most antisymmetric combination of Ising basis states $|\phi_\alpha\rangle$, as can be seen by closer inspection of the states (3.30).

¹See also the bibliography in [1], Chapter 5

Marshall’s second theorem [60, 10] assures that for the ground state

$$\langle \Psi_0 | \mathbf{S}_{\text{tot}} | \Psi_0 \rangle = \min, \quad (3.31)$$

where “min” indicates the minimally possible value of total spin. In the proof of Marshall’s second theorem it is shown that the energy is a monotonically increasing function of the total spin (see [1], p. 56). At no point of the proof a restriction on the size of each individual spin is needed. Therefore, the above theorem trivially applies to general spin chains. Thus, the ground state of uniform spin chains is a singlet of total spin zero, but also the ground state of general mixed spin chains will, if compatible with the chain composition, always be a singlet of total spin zero.

The third important theorem was found by Lieb *et al.* in 1962 and provides information about the excited states, in particular the first excited state. For the isotropic AFHM (with periodic boundary conditions) of homogeneous one-dimensional half-odd-integer spin chains there exists an excited state the energy of which is of order L^{-1} , with L the chain length. Thus, the spectrum is gapless in the limit $L \rightarrow \infty$, but only for spin $S = 1/2, 3/2, 5/2, \dots$. This is generally referred to as **Lieb-Schultz-Mattis** (LSM) argument. It does not state anything about integer spin chains. It was not until 1983 that Haldane [3] conjectured by semiclassical quantisation of the non-linear σ -model that there actually is a fundamental, intrinsic difference between uniform integer and half-odd integer spin chains with translationally invariant coupling. Uniform integer spin chains do show an excitation gap in their energy spectrum, called Haldane gap, even in the limit $L \rightarrow \infty$. A rigorous proof of this conjecture, however, is still lacking [61].

Let us quickly repeat the principle steps of the LSM argument. We define the unitary “twist operator”,

$$\mathbf{U}_T = \exp \left(i \frac{2\pi}{L} \sum_{j=1}^L j \mathbf{S}_j^z \right). \quad (3.32)$$

\mathbf{U}_T rotates the spins of a chain of length L with relative angle $2\pi/L$ in the x - y -plane between each neighbouring pair. The last spin in the chain is rotated by 2π . Applying this operator to the ground state $|\Psi_0\rangle$ creates an excitation $|\Psi_1\rangle = \mathbf{U}_T |\Psi_0\rangle$ the energy of which is the ground state expectation value of the transformed Hamiltonian $\langle \Psi_0 | \mathbf{U}_T^{-1} \mathbf{H} \mathbf{U}_T | \Psi_0 \rangle$. The transformation changes only the off-diagonal elements of \mathbf{H} by introducing an exponential factor,

$$\langle \phi_m | \mathbf{U}_T^{-1} \mathbf{H} \mathbf{U}_T | \phi_n \rangle = e^{\pm i \frac{2\pi}{L}} \langle \phi_m | \mathbf{H} | \phi_n \rangle, \quad (3.33)$$

the sign of which depends on $|\phi_m\rangle$ and $|\phi_n\rangle$. The ground state expectation value of the twisted \mathbf{H} can be written as

$$\begin{aligned} \langle \Psi_0 | \mathbf{U}_T^{-1} \mathbf{H} \mathbf{U}_T | \Psi_0 \rangle &= E_0^{\text{diag}} + \cos \left(\frac{2\pi}{L} \right) E_0^{\text{offd}} \\ &\approx E_0^{\text{diag}} + \left(1 - \frac{1}{2} \left(\frac{2\pi}{L} \right)^2 \right) E_0^{\text{offd}}, \end{aligned} \quad (3.34)$$

Table 3.2: Implications of LSM argument for half-odd integer and integer spin chains [62].

half-odd integer spin chains	integer spin chains
$S_1^z - M \neq \text{integer}$	$S_1^z - M = \text{integer}$
↓	↓
$z_{L \rightarrow \infty} = 0$	$z_{L \rightarrow \infty} \neq 0$ is possible
↓	↓
states excited by (3.32) are orthogonal to the ground state	states excited by (3.32) are not orthogonal to the ground state
↓	↓
system is gapless	system can be gapped

where E_0^{diag} and E_0^{offd} are the contributions to the ground state energy of the original untwisted Hamiltonian from diagonal and off-diagonal elements, respectively. E_0^{offd} is negative and proportional to L leaving an effective excitation energy of order $1/L$. Still, $|\Psi_1\rangle$ is not necessarily an eigenstate of \mathbf{H} . If, however, ground state and excited state can be shown to be orthogonal, i.e. if $\langle \Psi_0 | \Psi_1 \rangle = 0$, then there exists at least one eigenstate of \mathbf{H} of the same order of energy [62].

Homogeneous spin chains are translationally invariant (with translation operator $\mathbf{T}_1 : \mathbf{S}_j^\alpha \rightarrow \mathbf{S}_{j+1}^\alpha$). Thus, $|\Psi_0\rangle$ must be invariant under simple translation too,

$$z_L := \langle \Psi_0 | \Psi_1 \rangle \stackrel{!}{=} \langle \Psi_0 | \mathbf{T}_1^{-1} \mathbf{U}_T \mathbf{T}_1 | \Psi_0 \rangle = e^{i2\pi(S_1^z - M)} z_L. \quad (3.35)$$

z_L is called **twist order parameter**, M is the magnetisation, which will be zero in case of antiferromagnetic ground states, and S_1^z is the z -component of the spin at site $i = 1$. There are two possible solutions for the last equation: (i) $z_L = 0$ and (ii) the exponential equals unity. In case (i), $|\Psi_0\rangle$ and $|\Psi_1\rangle$ are orthogonal and the spectrum is gapless. In case (ii), $z_L \neq 0$ is possible and the spectrum can be gapped in the limit $L \rightarrow \infty$. For clarity the consequences of the LSM argument are listed in Table 3.2 for the two different cases.

Definition (3.32) gives a hint to the source of this difference, the last spin is rotated by 2π . This is yet not enough for half-odd integer spins to recover their original state $|\Psi\rangle$ but $-|\Psi\rangle$. Only rotations about 4π will end up in the initial state. Thus, a Berry phase factor is introduced that leads to orthogonality of the states excited by (3.32). As claimed in [11] the LSM argument can also be applied to mixed spin chains of type **A**, **B** and **C**. However, translational invariance is only retained with respect to the basis cells of a chain (i.e.: $\mathbf{T}_4 : \mathbf{S}_j^\alpha \rightarrow \mathbf{S}_{j+4}^\alpha$). A closer inspection shows

$$\begin{aligned} \langle \Psi_0 | \mathbf{T}_4^{-1} \mathbf{U}_T \mathbf{T}_4 | \Psi_0 \rangle &= \langle \Psi_0 | \exp \left(i \frac{2\pi}{L} \left(\sum_{j=1}^L (j-4) \mathbf{S}_j^z + L(\mathbf{S}_1^z + \mathbf{S}_2^z + \mathbf{S}_3^z + \mathbf{S}_4^z) \right) \right) | \Psi_0 \rangle = \\ &= \exp(i2\pi(S_{\text{bc}}^z - 4M)) z_L. \end{aligned} \quad (3.36)$$

Here, M again is the magnetisation, whereas S_{bc}^z denotes the total z -component of spin in the first unit cell. As all z component spin operators are diagonal we can replace them by their expectation values. Again, $M = 0$ should hold for the ground state and so gapless phases can only occur for non-integer values of S_{bc}^z . For models **A**, **B** and **C** this is trivially integer valued for $\alpha = 1$, and therefore our mixed spin chains with full translational invariance of coupling constants are gapped. With varying α , however, S_{bc}^z must be replaced by some effective value that depends on α , $S_{\text{eff}}^z(\alpha)$ [11].

3.4.2 Exact Energy Gap of Small Systems

By straightforward diagonalisation with routines from Numerical Recipes [63] the energy gap Δ between ground state and first excited states has been calculated for small volumes of uniform spin chains (Fig. 3.2), for the basis cells of all three mixed spin models and for two basis cells of models **A** and **B** (Fig. 3.3). By introducing α , the uniform chains become bond alternating models. For $S = 1/2$ the minimum must shift to $\alpha = 1$ (i.e. the uniform chain without bond alternation) for infinite system size in order to be consistent with the LSM argument. For the same reason it is clear that the minimum for $S = 1$ cannot converge to $\alpha = 1$ as this chain is gapped for $\alpha = 1$, but has a phase transition at a different value of α . The chain with $S = 3/2$, however, that according to LSM is gapless at $\alpha = 1$ does not yet show the tendency to converge appropriately at system sizes as small as $L = 4, 6$. The infinite system gaps of uniform spin chains with $\alpha = 1$ have been calculated by [53] with quantum Monte Carlo methods: $\Delta = 0.41048(6)$ for $S = 1$, $\Delta = 0.08917(4)$ for $S = 2$ and $\Delta = 0.01002(3)$ for $S = 3$. All three mixed systems show a minimum Δ at some value of α which is the finite size remnant of a gapless point α_c in the thermodynamic limit.

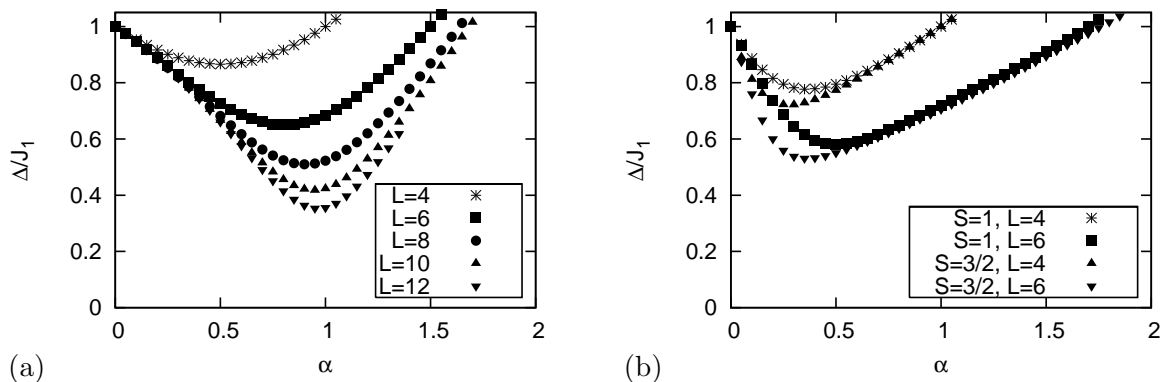


Figure 3.2: Exact excitation gap Δ for small volumes of uniform spin chains with $S = 1/2$ (a) and $S = 1, 3/2$ (b) against α .

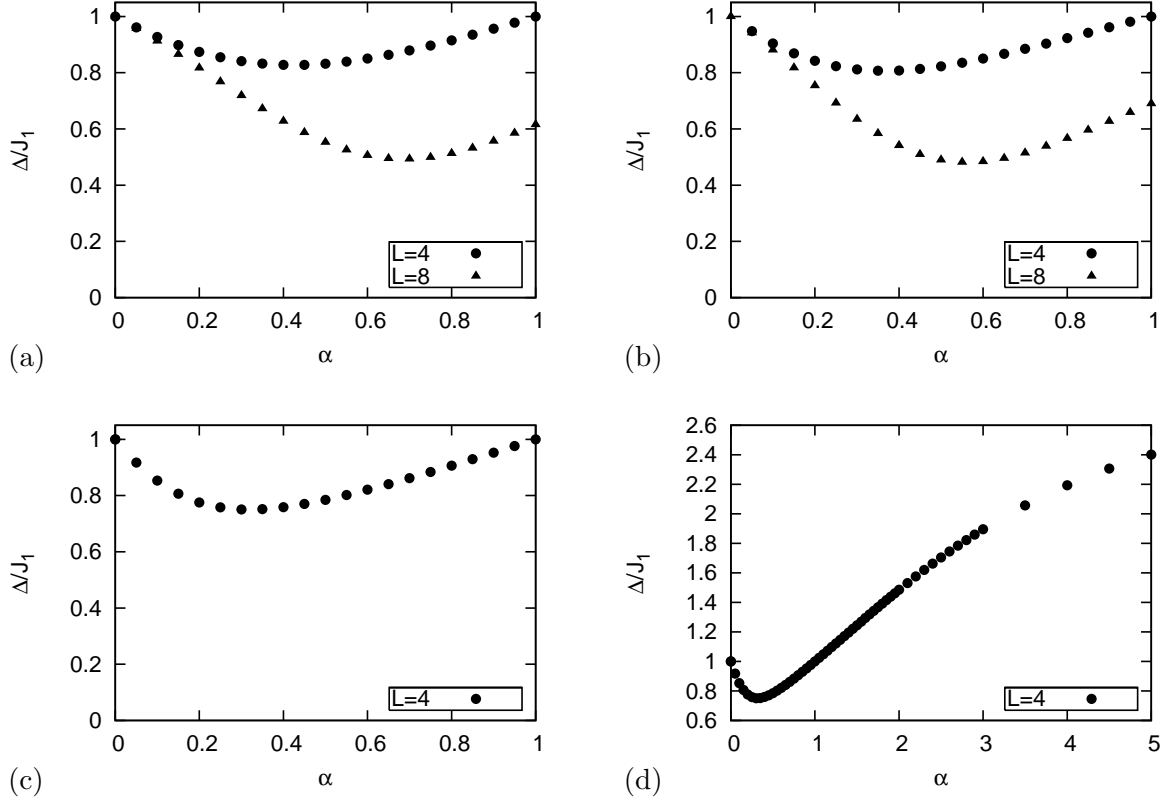


Figure 3.3: Exact excitation gap Δ of the basis cells of mixed spin chains against the coupling ratio α . (a) Model **A** for one and two basis cells. (b) Model **B** for one and two basis cells. Model **C** ((c) and (d)) does yet not show a second minimum of the excitation gap even at large α .

3.4.3 Valence Bond States and Phase Transitions

To qualitatively and intuitively understand the nature of the different phases under consideration, it is convenient to introduce the picture of valence bonds (VB). Pairs of spins with $s = 1/2$ (which are the subspins of higher magnitude spins) combine to form singlet states $\left(\frac{1}{\sqrt{2}}(|\uparrow\downarrow\rangle - |\downarrow\uparrow\rangle)\right)$ called valence bonds.

The operator that creates a VB between sites i and j is defined by

$$\mathbf{B}_{ij}^\dagger |0\rangle := \left(\mathbf{a}_i^\dagger \mathbf{b}_j^\dagger - \mathbf{b}_i^\dagger \mathbf{a}_j^\dagger \right) |0\rangle, \quad (3.37)$$

where \mathbf{a}^\dagger and \mathbf{b}^\dagger are Schwinger boson operators (see e.g. [1], Chapter 7) that create spin-up-like and spin-down-like particles respectively and $|0\rangle$ is the vacuum with respect to bosons. \mathbf{B}_{ij}^\dagger is called a bond operator as it creates a valence bond singlet between sites i and j . A general VB state is then given by

$$|\Psi_{\text{VB}}\rangle = \sum_{\alpha} c_{\alpha} \prod_{(i,j) \in \Lambda_{\alpha}} \mathbf{B}_{ij}^\dagger |0\rangle, \quad (3.38)$$

where the condition $(i, j) \in \Lambda_{\alpha}$ simply means that the bond configuration must be compatible with spin sizes and lattice structure, c_{α} are the corresponding coefficients. The states $|\Psi_{\text{VB}}\rangle$

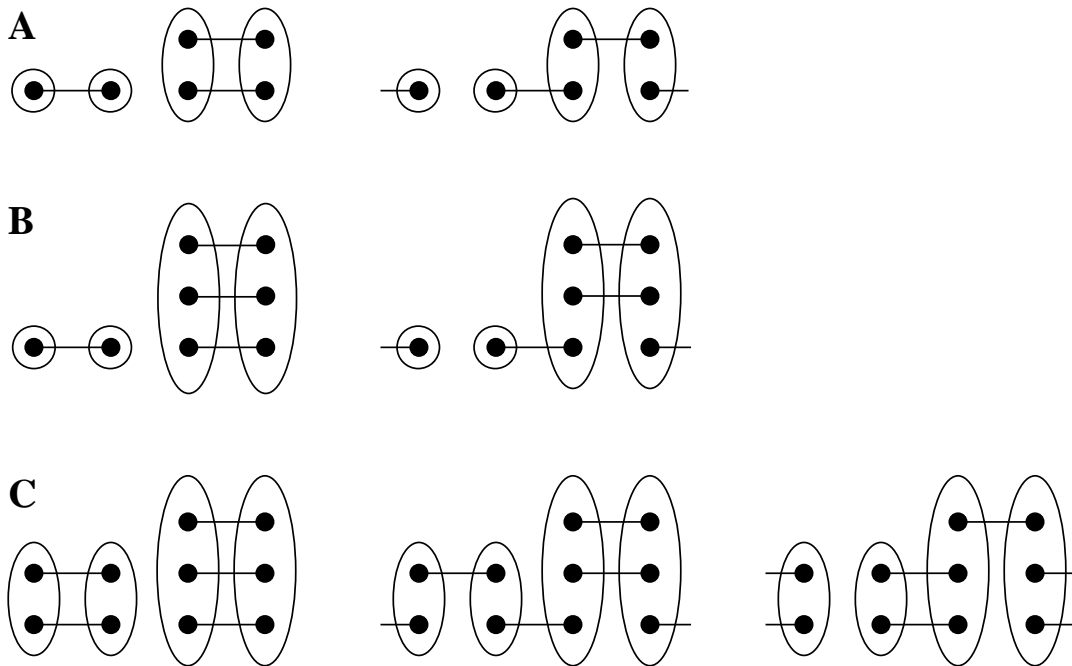


Figure 3.4: Valence bond configurations of the basis cells of mixed spin chains. *Filled circles* represent subspins with $s = 1/2$. Valence bond singlets are represented by lines connecting two subspins at different sites. Model **C** has an additional phase.

include all possible bonds, also between sites separated more than one lattice spacing. It turns out that for many models the coefficients can be set to zero if bonds are included that connect sites of distance more than one lattice spacing. The remaining VB states then form a restricted class of states [62] the constituent wave functions of which are described by

$$|\Psi_{\text{VBS}}^{m,n}\rangle := \frac{1}{\sqrt{\mathcal{N}}} \prod_{k=1}^{L/2} (\mathbf{B}_{2k-1,2k}^\dagger)^m (\mathbf{B}_{2k,2k+1}^\dagger)^n |0\rangle, \quad (3.39)$$

where \mathcal{N} is a normalization factor and m and n again must satisfy spin- and lattice-compatibility conditions in order to create allowed bond configurations. Here, $m + n$ is equal to the number of maximally possible bonds for each basis cell such that all subspins are part of a VB. For $m \neq 0$ and $n \neq 0$, $|\Psi_{\text{VBS}}^{m,n}\rangle$ is generally called a “valence bond solid” (VBS), in case of either $m = 0$ or $n = 0$ one talks about a “valence bond dimer”, which is often not called a VBS. The possible VB configurations of our models are shown in Fig. 3.4. This does not necessarily mean that either of our models *is* in a VB state but rather that its ground state might be approximated by one of the VB states.

VB states are not exact ground states of the AFHM, but they serve as good variational trial states with c_α , the variational parameters. Hamiltonians for which VB states are exact ground states can be constructed. Affleck *et al.* [4, 64] for example proposed a Hamiltonian with biquadratic interactions that include the AFHM as special case. The model is called AKLT-model and shows a VBS ground state for special values of the quadratic term.

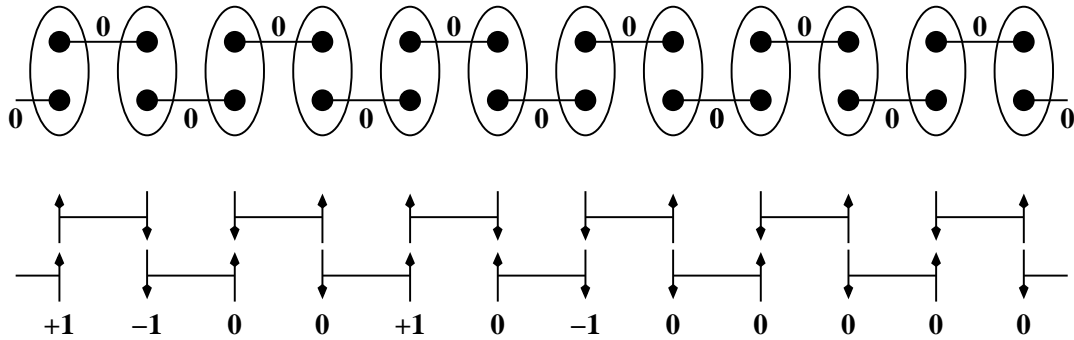


Figure 3.5: Valence bond solid configuration of uniform spin chain with $S = 1$. If this is the ground state VB configuration of the chain, it is said to be in the “Haldane phase”. *Top*: Filled circles denote subspins and lines VB singlets between subspins. The 0’s indicate that the total spin of connected subspins is zero. The entire chain has total spin zero. *Bottom*: Spin configuration that contributes to the VBS. Arrows denote subspins and the number show the total spin orientation m at each site.

In contrast, a model proposed by Majumdar and Ghosh [65] with next-nearest neighbour interaction has a dimerised VB ground state. In case of our models for a coupling ratio $\alpha = 0$, the ground state is trivially best approximated by the dimerised VB configuration, i.e. the left-most configurations in Fig. 3.4.

VBS states are quantum disordered even at $T = 0$ in the sense that the spins form some “liquid Néel” order. This is illustrated by an example for the uniform chain with $S = 1$ in Fig. 3.5. Spins with $m = \pm 1$ occur in alternating order but can be separated by any (random) number of spins with $m = 0$ [61]. Consequently, correlations are short ranged in VBS states. In fact, a VBS state in this case is the superposition of all wave functions that show “liquid Néel” order. The VB picture was extended to a singlet-cluster picture to include also singlet bonds of more than just two sites [13].

Phase Transitions in Models A, B and C

For transitions between different VB configurations to take place at a critical coupling ratio α_c the bonds on one “chain” of subspins must break and rearrange. At the critical point the system then hosts a “subchain” with $s = 1/2$ which gives rise to gapless excitations [12, 13]. By varying the coupling ratio $\alpha = J_2/J_1$ from zero to low non-zero values, spins that are initially uncoupled begin to “feel” each other’s presence. Still, however, the “original” bonds shown by the left-most configurations in Fig. 3.4 dominate until at the critical points α_c both bonds are equally relevant. Further raising the parameter α , leads to another phase where now the bonds between unlike spins come into play (see the second column in Fig. 3.4). In models **A** and **B** the bonds between the two spins of size $S_a = 1/2$ disappear, whereas model **C** enters an intermediate phase with valence bonds between all spins. Even in model **C**, however, the bonds between the smaller spins of size $S_a = 1$ disappear for sufficiently large α .

3.5 Observables

3.5.1 Twist Order Parameter

In Section 3.4.1 we have introduced the twist order parameter as the ground state expectation value of the twist operator,

$$z_L = \langle \Psi_0 | \mathbf{U}_T | \Psi_0 \rangle . \quad (3.40)$$

In [62] it was proposed to use z_L as an order parameter to signal transitions between different VB configurations. z_L in fact, is a complex quantity. For periodic boundary conditions, however, parity symmetry of (3.32) ensures that it is real. Consequently we will only consider the real part of z_L and refer to it by the same name. As different gapped phases are separated by gapless phase boundaries, $z_L = 0$ is a sufficient condition for the critical point. Furthermore, it was shown in [62] for the restricted class of VB states (3.39) of general homogeneous spin chains that

$$\langle \Psi_{\text{VB}}^{(m,n)} | \mathbf{U}_T | \Psi_{\text{VB}}^{(m,n)} \rangle = (-1)^n \left(1 - \mathcal{O}\left(\frac{1}{L}\right) \right) . \quad (3.41)$$

The argument in [62] should also hold for mixed spin chains. Thus, for sufficiently large L the sign of z_L only depends on the number of bonds n (or equivalently m since $m + n$ is fixed), and the transition from one VB state to the logically next can simply be detected by a change of sign of the twist order parameter. Figure 3.4 shows that the number of bonds between two sites changes by one, going from one phase to the next one.

It is important to emphasise here that the above relation is valid only for exact VB states. The ground states of Heisenberg antiferromagnets, however, are only approximated by VB states. It is concluded in [62] that the approximation becomes less adequate for larger spins.

Figure 3.6 shows the real part of z_L for models **A** and **B** as well as uniform spin chains with $S = 1/2, 1, 3/2$ for small chain lengths L obtained from exact diagonalisation. In the special case of uniform coupling at $\alpha = 1$ the $S = 1/2$ chain is gapless and so is the chain with $S = 3/2$ which already shows even at small system sizes². All other chain types shown have gapless phases at values of $\alpha \neq 1$.

²Note that the excitation gap becomes zero only in the infinite-volume limit which is, however, reflected also in finite size systems (see Section 5.5.2).

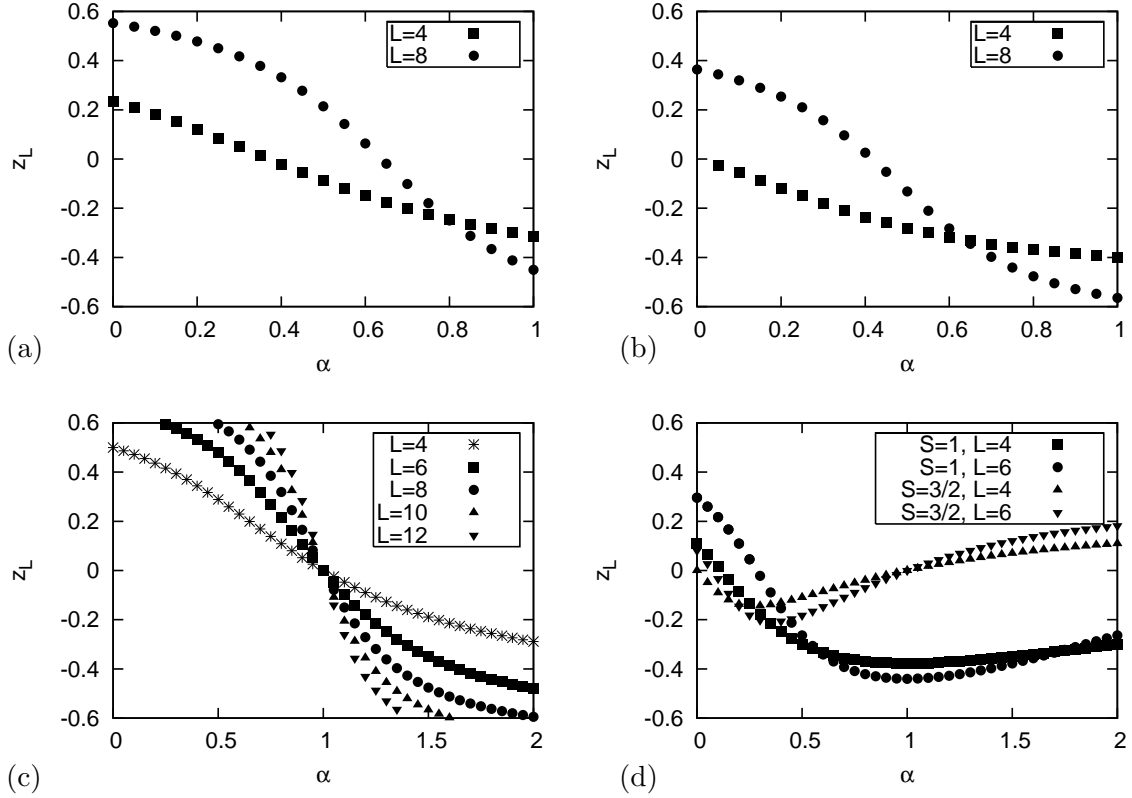


Figure 3.6: Twist order parameter z_L (the real part of it, to be precise) against α , the coupling ratio, for small chain lengths L . Zero points reflect gapless phases in the thermodynamic limit. Models **A** and **B** ((a) and (b)) are gapped for $\alpha = 1$. Uniform spin chains with half-odd integer spins ((c) $S = 1/2$, (d) $S=3/2$) are gapless at $\alpha = 1$. (d) also shows the chain with $S = 1$ with a gapped phase for uniform coupling.

3.5.2 Dynamic Susceptibilities and Correlation Lengths

Expressing the susceptibility in (2.9) in terms of spin operators and taking account of imaginary time we can write the uniform magnetic susceptibility as

$$\chi_u = \frac{1}{\beta L} \sum_{r_0, r} \iint_0^\beta d\tau_0 d\tau \langle \mathbf{S}_{r_0}^z(\tau_0) \mathbf{S}_{r_0+r}^z(\tau_0 + \tau) \rangle - \langle \mathbf{S}_{r_0}^z(\tau_0) \rangle \langle \mathbf{S}_{r_0+r}^z(\tau_0 + \tau) \rangle, \quad (3.42)$$

where the sums run over all sites of a spin chain of length L . Similarly the staggered susceptibility is expressed by

$$\chi_s = \frac{1}{\beta L} \sum_{r_0, r} (-1)^r \iint_0^\beta d\tau_0 d\tau \langle \mathbf{S}_{r_0}^z(\tau_0) \mathbf{S}_{r_0+r}^z(\tau_0 + \tau) \rangle - \langle \mathbf{S}_{r_0}^z(\tau_0) \rangle \langle \mathbf{S}_{r_0+r}^z(\tau_0 + \tau) \rangle. \quad (3.43)$$

These above relations are special cases of a more general kind of susceptibility, the so-called dynamic susceptibility $\chi(k, \omega)$ defined by

$$\chi(k, \omega) = \frac{1}{\beta L} \sum_{r_0, r} \iint_0^\beta d\tau_0 d\tau e^{-i(kr - \omega\tau)} \langle \mathbf{S}_{r_0}^z(\tau_0) \mathbf{S}_{r_0+r}^z(\tau_0 + \tau) \rangle - \langle \mathbf{S}_{r_0}^z(\tau_0) \rangle \langle \mathbf{S}_{r_0+r}^z(\tau_0 + \tau) \rangle. \quad (3.44)$$

Owing to the periodic boundary conditions in both spatial and imaginary time direction the values of k and ω for finite L and β are restricted to integer multiples $2\pi/L$ and $2\pi/\beta$, respectively. The imaginary time frequencies ω are called Matsuraba frequencies. The quantity (3.44) is often referred to as *dynamic structure factor* as it is analogous to the real time dynamic structure factor that is measured in neutron scattering experiments.

The dynamic susceptibilities $\chi(k, \omega)$ give the response of the system to an applied magnetic field that varies in imaginary time with frequency ω and in space with wave number k . For the uniform and staggered magnetic susceptibilities from above we write

$$\chi_u = \chi(0, 0) \quad \text{and} \quad \chi_s = \chi(\pi, 0). \quad (3.45)$$

Obviously, for antiferromagnetic systems the staggered magnetisation $M_s = 1/L \sum_r (-1)^r m_i$, and the staggered susceptibility χ_s are the quantities of interest as they measure the anti-alignment of spins.

In order to calculate the imaginary time correlation length ξ_τ , we can use the dynamic susceptibilities by defining the second-moment estimator [53, 66, 67]:

$$\xi_\tau^{(2)} = \frac{\beta}{2\pi} \sqrt{\frac{\chi(\pi, 0)}{\chi(\pi, 2\pi/\beta)} - 1}. \quad (3.46)$$

For a given L and $\beta \rightarrow \infty$ the second-moment estimator is known to converge against $\xi_{\tau,0} = 1/\Delta$ apart from systematic corrections that become small for large $\xi_{\tau,0}$ [53]. This method can only be applied if there is a finite gap above the first excited state. This is, however, always the case for finite systems which we are concerned with. Δ is the energy gap between the ground state and the first excited state. Even smaller systematic corrections are involved when using the fourth-moment estimator [53]:

$$\xi_\tau^{(4)} = \frac{\beta}{4\pi} \sqrt{3 \frac{\chi(\pi, 0) - \chi(\pi, 2\pi/\beta)}{\chi(\pi, 2\pi/\beta) - \chi(\pi, 4\pi/\beta)} - 1}. \quad (3.47)$$

Similar to (3.46) a second-moment estimator can be constructed for the spatial correlation length ξ by [67, 68, 69]:

$$\xi^{(2)} = \frac{L}{2\pi} \sqrt{\frac{\chi(\pi, 0)}{\chi(\pi + 2\pi/L, 0)} - 1}. \quad (3.48)$$

Second- and fourth-moment estimators need a few remarks. As no fits to the asymptotic behaviour of the correlation function are involved, the moment estimator methods tend to be more stable and simpler to be applied. Systematic errors decrease with large correlation lengths which is especially true in the vicinity of quantum critical points.

Chapter 4

Quantum Critical Phenomena

In this chapter a short introduction to continuous quantum phase transitions will be given. They are also referred to as quantum critical phenomena and have raised considerable interest in the recent years. Even though they occur only at $T = 0$ by definition, quantum critical points can significantly influence the characteristics of a system at finite temperatures [70, 71]. In Section 4.1 parallels and contrasts between classical and quantum phase transitions will briefly be presented. In Section 4.2 the discussion will focus on the models under consideration, i.e. mixed spin chains. The implication of the Mermin–Wagner–Hohenberg theorem will be presented and the problem upon applying it briefly outlined. This chapter largely follows [72]. For an extensive discussion of quantum critical phenomena the reader is referred to [2].

4.1 General Aspects

Classical systems in equilibrium at non-zero temperatures always show temperature driven fluctuations. Upon approaching a critical point T_c the size of fluctuations will grow larger and larger. Precisely at the critical point fluctuations at all length scales occur and the correlation length of fluctuations of the order parameter becomes infinite. The system itself then is scale-invariant, i.e. self-similar on all length scales. At zero temperature nothing fluctuates in classical systems, all degrees of freedom are frozen and the system is in its ground state.

In quantum systems, in contrast, even at $T = 0$ quantum fluctuations of the ground state may still be present due to the Heisenberg uncertainty principle. The scale of order parameter fluctuations and the corresponding correlation length is governed by the coupling strength(s) that are involved. By driving a control parameter towards a quantum critical point (QCP) the scale of quantum fluctuations eventually becomes infinite. The coupling strength(s) may be controlled by parameters such as some dopant concentration of impurities or, as in the classical case, magnetic fields that this time couple to off-diagonal operators.

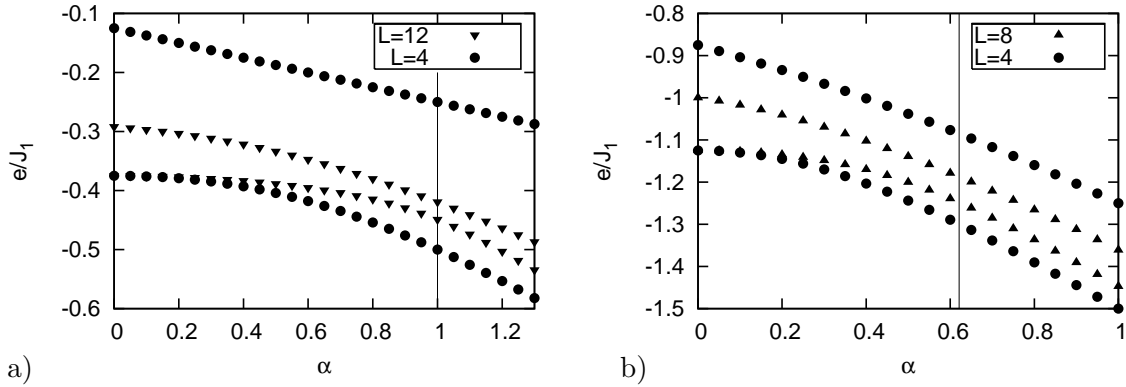


Figure 4.1: Energy per spin of ground state and lowest excited state(s) as a function of the coupling ratio α for small spin chains. Remarkably the vanishing of the energy gap at the critical value α_c (*thin vertical lines*) is already foreseeable for volumes as small as $L = 8, 12$. (a) Uniform spin chain with $S = 1/2$. (b) Mixed spin chain of model **B** with $S_a = 1/2$ and $S_b = 3/2$.

The divergence of the correlation length upon approaching a QCP is described by a power law analogously to the temperature driven classical transition

$$\xi \sim |\alpha - \alpha_c|^{-\nu}, \quad (4.1)$$

where α is the control parameter and α_c its critical value. Similarly the inverse of a characteristic energy scale Δ – that might be the excitation gap – diverges by

$$\frac{1}{\Delta} \sim |\alpha - \alpha_c|^{-z\nu}, \quad (4.2)$$

with z , the dynamic critical exponent that is not to be mistaken for the exponent of auto-correlation of Monte Carlo simulations (see Section 5.1). We have seen in Section 2.3 that quantum systems can be mapped onto classical systems with an extra dimension, imaginary time τ . The imaginary time correlation length of the infinite classical system (i.e. $T = 0$) mapped from Heisenberg spin chains is equal to the inverse excitation gap. More generally, the quantum–classical mapping in some sense maps onto a system with dimension $d+z$ [2, 70, 71].

To be precise, QCPs are defined by non-analytic changes in the ground state energy of a system or one of its derivatives. Thus, by definition all phase transitions and critical phenomena that can be detected at non-zero temperatures are classical. In the simplest case this non-analyticity is due to an excited state becoming the ground state which is called level-crossing. This leads to a first-order phase transition. In contrast, continuous quantum phase transitions are related to a higher-order singularity in the ground state that involve the low-temperature spectrum of the system. In finite systems this is reflected by an avoided level-crossing that becomes “sharp” in the thermodynamic limit [72]. The avoided level-crossing is shown in Fig. 4.1 for two different short spin chains.

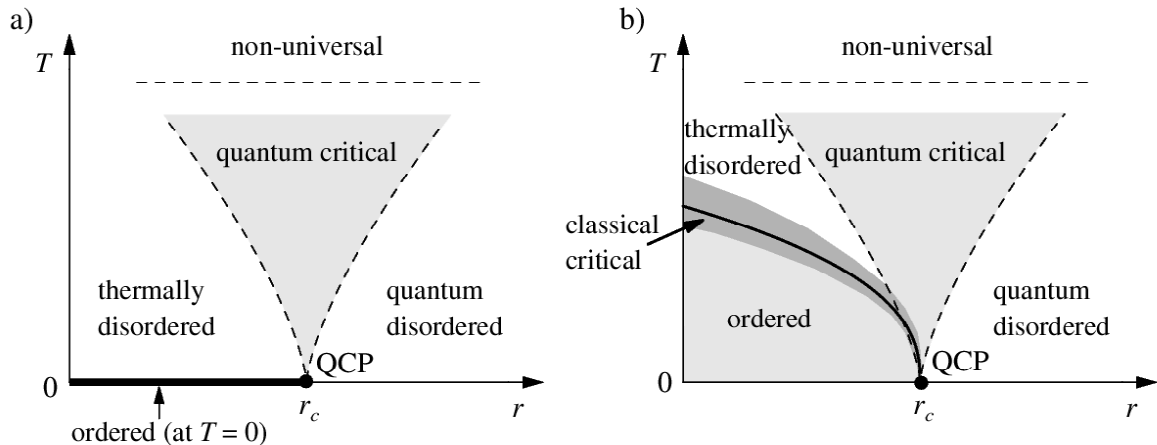


Figure 4.2: Two different cases of the phase diagram around a quantum critical point, r is the control parameter. In the quantum critical region thermal and quantum fluctuations are important. In (a) there is no line of classical phase transitions at non-zero temperatures. This corresponds, e.g., to the quantum (or transverse) Ising model. In contrast, (b) shows non-zero temperature transitions that end at the quantum critical point. The classical theory can be applied in the narrowing shaded region around the critical line. (Image taken from [72].)

Let us quickly consider the generic example of a system that shows a quantum phase transition, the infinite quantum Ising model (also referred to as transverse Ising model) in one dimension. Starting from the classical Ising model an off-diagonal term is introduced by adding a field h that couples to the x -component of spin

$$\mathbf{H}_{\text{QI}} = J \sum_i \mathbf{S}_i^z \mathbf{S}_{i+1}^z + h \sum_i \mathbf{S}_i^x. \quad (4.3)$$

The first term is simply the classical Ising model. The second term introduces quantum fluctuations as it mediates between states up and down. At $T = 0$ the classical Ising model that corresponds to $h = 0$ is magnetically long-range ordered. Quantum fluctuations induced by $h > 0$ eventually destroy this magnetic long-range order at the critical value $h_c = J$, where the system becomes a quantum paramagnet. At non-zero temperatures thermal fluctuations set in that destroy the long-range order on the magnetically ordered side while on the paramagnetic side it is still the quantum fluctuations that dominantly determine the characteristic properties of the system. In the quantum critical region (see Fig. 4.2a), however, that fans out from the quantum critical point, both types of fluctuations are important. The properties of the system strongly depends on the low-lying states that can be thermally excited from the quantum critical ground state. These low-lying excited states cannot be described in terms of quasi-particles but correspond to a critical continuum of excitations [72]. The temperature up to which the quantum critical region extends can be surprisingly high [70, 71] – including room temperature – and depends on the coupling(s) and, in turn, the low-energy spectrum.

Table 4.1: Parallels and contrasts between classical and quantum critical points.

Classical critical points	Quantum critical points
Statics and dynamics decoupled	Statics and dynamics coupled
Thermal fluctuations at $T \neq 0$	Quantum fluctuations at $T = 0$
Scale invariance	Scale invariance
Dimension d	Dimension $d + z$
Divergent correlation length ξ	Divergent correlation lengths ξ and $\xi_\tau \sim \xi^z$
Free energy is non-analytic at $T = T_c$	Ground state energy is non-analytic at $\alpha = \alpha_c$

By quantum–classical mapping the one-dimensional quantum Ising model can be mapped onto a two-dimensional classical Ising model. The length of the extra dimension – imaginary time – is given by the inverse temperature β . The crossover from either side into the quantum critical region takes place as soon as the system “realises” the finiteness of this extra dimension. This happens when the imaginary time correlation length ξ_τ becomes comparable to β .

Systems that permit long-range order, or spontaneously broken symmetry to be more precise, at non-zero temperatures can show a line of classical critical points that ends at the quantum critical point (see Fig. 4.2b). Sufficiently close to this line of critical points thermal fluctuations always dominate, leading to a classical phase transition. The area where the classical theory can be applied narrows for lower temperatures. The crossover here corresponds to a dimensional crossover, and the critical behaviour will be asymptotically described by exponents emerging from d -dimensional systems instead of $d + z$ dimensional ones.

However, not all is well with quantum–classical mapping. There are properties special to quantum systems that cannot be mapped onto classical ones, i.e. are not reflected by the classical system (see [2], Chapter 1). In particular, systems that involve topological Berry phase terms render the quantum theories qualitatively different from their classical counterparts. Such transitions can show so-called local critical behaviour [72]. Furthermore, it is non-trivial to determine dynamic properties of quantum systems from quantum–classical mapping as quantum dynamics is characterised by the phase coherence time that has no classical analogue either. By keeping this in mind, however, it is still possible to gain valuable information about a quantum critical point by analysing the behaviour of the corresponding classical model. Parallels and contrast between classical and quantum critical points are summarised in Table 4.1.

4.2 Quantum Critical Points in Mixed Spin Chains

In mixed spin chains we deal with transitions between ground states that are approximately described by different valence bond configurations. This transition is induced by tuning the bond alternation parameter α . The specific magnitude of spins primarily influences the critical value of α but can also lead to additional critical points. The fact that chains of homogeneous spin size also have gapless critical points as a function of the bond alternation parameter α , indicates that the phenomena under consideration are not restricted to mixed spin chains only. Thus, the inclusion of regular spin impurities does not necessarily mean the rise of new and unobserved effects.

If the mixed spin chain Hamiltonian (3.25) is taken to the extreme limit of $\alpha \rightarrow 0$, the system will merely consist of independent antiferromagnetic pairs of like spins. The system will be dimerised. The free energy density of the models under consideration can then simply be determined from the values given in Table 3.1. The excitation gap Δ , corresponding to one of the independent subsystems being excited to a state of non-zero total spin, then is J_1 for all kinds of mixed or uniform chains. By raising α to small but non-zero values, another antiferromagnetic coupling is introduced that eventually destroys the dimer-like character of the ground state. The energy gap is altered as excitations now can spread over the whole chain. At the critical point the dimer-like VB configuration is eventually broken.

We are also interested in the low-temperature properties of the QCPs found in models **A**, **B** and **C**. As will be shown in Chapters 6 and 7, the twist order parameter that seems well suited to detect transitions between different VB configurations allows for the determination of a “transition” point even at non-zero temperatures. However, if this is just an “echo” of the ground state or maybe also due to properties of excited states needs closer investigation of the low temperature spectra of the infinite chains.

The Mermin–Wagner–Hohenberg theorem [73, 74]¹ that can be used to rule out many types of transitions of Heisenberg models in one and two dimensions does not necessarily exclude a non-zero temperature phase transition in our case. It states that for isotropic Heisenberg models with finite exchange interactions the quantity

$$m(\vec{k}) = \frac{1}{N} \sum_{\vec{r}} \langle m(\vec{r}) e^{i\vec{k}\vec{r}} \rangle, \quad (4.4)$$

cannot take on a non-zero value if no magnetic field is applied in one and two dimensions. Obviously, the above equation defines the lattice magnetisation with respect to an external magnetic field with ordering wavevector \vec{k} . Thus, spontaneous lattice or sublattice magnetisation is ruled out. We will not state the proof but rather refer the reader to the literature. However, it is necessary to emphasise that no assumption on the spin magnitude is made. The

¹See also [1], Chapter 6.

spin magnitude only enters the proof to provide an upper bound in an inequality via

$$N \sum_{\vec{r}} \langle \mathbf{S}_{\vec{r}}^{\alpha} \mathbf{S}_{\vec{r}}^{\alpha} \rangle = S(S+1), \quad (4.5)$$

where \mathbf{S}_i^{α} denotes the α -component of the spin operator $\vec{\mathbf{S}}$ at site i . Here it is assumed that all spins are of the same kind. By replacing $S(S+1)$ by $L/2(S_a(S_a+1) + S_b(S_b+1))$ the theorem is easily extended to mixed spin chains. Thus, it also holds for mixed spin chains. The symmetry that is reflected by (4.4) cannot be spontaneously broken at $T > 0$ in one or two dimensions. The symmetry group of the Heisenberg Hamiltonian is $SU(2)$ and it is argued in [61, 75] that gapped antiferromagnetic ground states are related to breaking a discrete $Z_2 \times Z_2$ subgroup of rotations of π about the quantisation axis. It is not yet obvious that the Mermin–Wagner–Hohenberg theorem explicitly excludes the spontaneous breaking of this symmetry subgroup at non-zero temperatures.

By mapping to imaginary time we deal with a two-dimensional system that is infinite in one dimension (space) and finite or infinite in the second dimension (imaginary time, inverse temperature). At zero temperature the system is effectively two-dimensional but with Ising-like interactions. By raising the temperature this effective dimension is reduced to one. Long-range order in one-dimensional Ising-like systems is not possible. The signature of a critical point, a divergent spatial correlation length, cannot show up at finite temperatures as the second dimension is limited and not infinite and therefore limits the growth of the spatial (and, of course, the temporal) correlation length. This implies that we cannot expect to observe diverging correlation lengths of the mapped classical system at finite temperatures. Which is exactly what we are going to see in Chapters 6 and 7.

Chapter 5

Quantum Monte Carlo

In this chapter the concept of Monte Carlo techniques to evaluate large sums or integrals will be described. The obvious physical candidate is the partition function that rapidly becomes inaccessible to exact analytical or numerical methods even for small system sizes.

Instead of “directly” computing the partition function, one takes another route and evaluates the sum or integral stochastically by creating a suitable set of configurations. The crucial part of Monte Carlo then is to ensure that these configurations obey the probability distribution imposed by the nature of the problem.

We have seen in Section 2.1 that the probability of a given configuration or microstate to occur is

$$p_i = \frac{1}{Z} e^{-\beta E_i}. \quad (5.1)$$

Provided, one succeeds to create a set of N configurations distributed as (5.1), any physical quantity A can then be estimated simply via

$$\langle A \rangle_{\text{MC}} = \frac{1}{N} \sum_{i=1}^N A_i, \quad (5.2)$$

where A_i is the value of quantity A for configuration i , and $\langle \dots \rangle_{\text{MC}}$ denotes the Monte Carlo average. The error of this statistical mean value is given by the square root of the variance σ_A that itself must be treated as a statistical quantity. Its “naive” estimator is [76]

$$\langle \sigma_A \rangle_{\text{MC}} = \frac{1}{N-1} \sum_{i=1}^N (A_i - \langle A_i \rangle_{\text{MC}})^2. \quad (5.3)$$

The standard error then is

$$\varepsilon_A = \sqrt{\frac{\langle \sigma_A \rangle_{\text{MC}}}{N}}. \quad (5.4)$$

We will from now on, for the rest of this chapter, drop the subscript denoting the Monte Carlo average. In Section 5.1 the way how distribution (5.1) can be sampled will principally be shown. In Section 5.2 the Loop Algorithm [6, 7] is introduced. In Section 5.3 the specific

algorithm that was used to produce data sets that are analysed in this thesis will be presented. In Section 5.4 the reliability of the algorithm is confirmed to a certain extent by comparing the quantum Monte Carlo output to results known from exact diagonalisation of small systems. Finally, in Section 5.5 the finite-size scaling analysis applied in this thesis will be described. For a general introduction into Monte Carlo methods in statistical physics see for example [42].

5.1 Traditional Monte Carlo

The problem in (5.1) is that the partition function Z is generally unknown and hard to calculate exactly, and the statistical weight of randomly created configurations cannot be determined directly. This difficulty can be avoided by successively generating configurations of non-zero weight from one another following specific update rules. For systems in equilibrium a detailed balance condition must hold,

$$P_i W_{i \rightarrow f} \stackrel{!}{=} P_f W_{f \rightarrow i}, \quad (5.5)$$

where $P_{i/f}$ is the probability (i.e. the Boltzmann weight (5.1)) of the system to be in the initial/final state of an update process and $W_{i \rightarrow f/f \rightarrow i}$ is the transition rate to go from initial to final/final to initial configuration. Any transition rate that satisfies the above condition and ergodicity, i.e. that any configuration of non-zero weight must be possible to be reached within a finite number of steps, can be taken. One of the most common and known update rates is the Metropolis type,

$$W_{i \rightarrow f} = \min(e^{-\beta(E_f - E_i)}, 1). \quad (5.6)$$

The implementation of Metropolis updates leads to the typical accept/reject step. A new configuration is accepted if $\min(e^{-\beta(E_f - E_i)}, 1) \geq r$, with r a uniformly distributed random number between 0 and 1, and rejected otherwise. In the rejection case the initial configuration is counted again.

Accept/reject-methods usually perform local changes, such as random or successive spin flips for spin lattice models. Obviously, successive configurations are correlated and thus not statistically independent. This leads to a severe error in the estimate of the variance (5.3) that can be corrected by replacing N by [76]

$$N_{\text{eff}} = \frac{N}{2\tau_{\text{int}}}, \quad (5.7)$$

with $\tau_{A,\text{int}}$, the integrated autocorrelation time that is specific for each observable and $\sim \min(L, \xi)^z$. Usually the value of z is around two and larger. Thus, for large systems and close to second-order phase transitions there are strong autocorrelations which immensely reduce the effectiveness of local update algorithms.¹ Autocorrelations are effectively reduced with cluster update methods such as the Swendsen–Wang [77] and Wolff [78] algorithms for

¹Close to second-order phase transitions this phenomenon is called “critical slowing down”.

classical spin systems. By randomly distributing bonds between like spins with a special probability, clusters, that can be highly non-local, are generated and then flipped, no accept/reject step is needed. For quantum spin systems that are spread out into imaginary time the building of clusters is more complex in order to avoid forbidden configurations. In the following section one way to build clusters on quantum spin systems will be discussed by introducing the Loop Algorithm. Global cluster updates greatly reduce autocorrelations and hence allow for effective simulations of large (quantum) systems and systems close to second-order phase transitions.

5.2 Quantum Monte Carlo: Loop Algorithm

To overcome critical slowing down in quantum systems the Loop Algorithm has been designed to perform local and global updates. It was developed for quantum systems and works on a $(d+1)$ -dimensional lattice with classical degrees of freedom where closed loops are constructed and then flipped (updated) with suitable probability. Special quantum features of each model are incorporated into the loop building rules.

The extra dimension has already been introduced in Section 2.3. The d -dimensional quantum spin model ($d = 1$ in our case) is spread out onto a $(d+1)$ -dimensional model with classical degrees of freedom. The Loop Algorithm requires a slightly altered mapping. The presentation of both the discrete time and the continuous time version of the Loop Algorithm in this section will largely follow [7, 8].

5.2.1 Discrete Time

Consider the one-dimensional Heisenberg Hamiltonian for $S = 1/2$. We begin by breaking it up into two pieces:

$$\mathbf{H} = \mathbf{H}_e + \mathbf{H}_o, \quad (5.8)$$

$$\mathbf{H}_{e/o} = J \sum_i \mathbf{S}_{i,i+1} \quad \text{with } i \text{ even/odd.} \quad (5.9)$$

\mathbf{H}_e and \mathbf{H}_o do not commute themselves but contain only two-particle Hamiltonians that commute with each other. We use the Trotter–Suzuki formula for two non-commuting operators \mathbf{A} and \mathbf{B} ,

$$e^{\mathbf{A}+\mathbf{B}} = \lim_{M \rightarrow \infty} \left(e^{\frac{\mathbf{A}}{M}} e^{\frac{\mathbf{B}}{M}} \right)^M, \quad (5.10)$$

to rewrite the quantum partition function as

$$\begin{aligned} Z &= \sum_n \langle \phi_n | e^{-\beta(\mathbf{H}_e + \mathbf{H}_o)} | \phi_n \rangle \\ &= \lim_{M \rightarrow \infty} \sum_n \langle \phi_n | \underbrace{\left(e^{-\frac{\beta}{M} \mathbf{H}_e} e^{-\frac{\beta}{M} \mathbf{H}_o} \right) \dots \left(e^{-\frac{\beta}{M} \mathbf{H}_e} e^{-\frac{\beta}{M} \mathbf{H}_o} \right)}_{M \text{ times}} | \phi_n \rangle. \end{aligned} \quad (5.11)$$

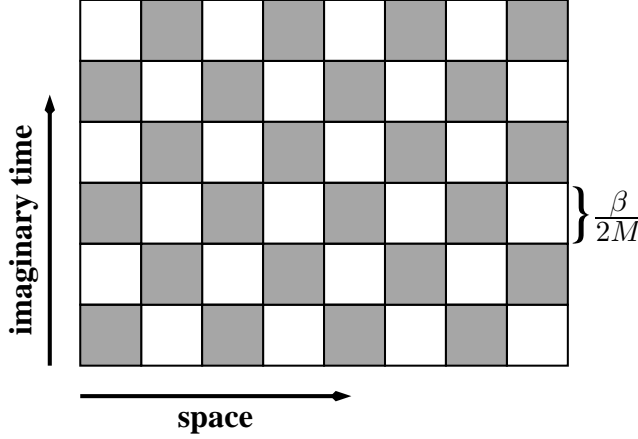


Figure 5.1: Checkerboard of one-dimensional spin chain. Ising spins (\uparrow or \downarrow) live at the corners of each plaquette. Even and odd indexed exponential operators are simply products of their two-particle composite terms, $\exp(J \sum_i \dots) = \prod_i \exp(J \dots)$. The system evolves in imaginary time alternatingly on even and odd indexed plaquettes, i.e. only the shaded plaquettes are relevant. Each row of plaquettes represents an imaginary time step of size $\beta/2M$.

Now we can insert $2M - 1$ complete sets of basis states between each exponential operator to obtain

$$Z = \lim_{M \rightarrow \infty} \sum_{n_0} \dots \sum_{n_{2M-1}} \left[\begin{aligned} &\langle \phi_{n_0} | e^{-\frac{\beta}{M} \mathbf{H}_e} | \phi_{n_1} \rangle \langle \phi_{n_1} | e^{-\frac{\beta}{M} \mathbf{H}_o} | \phi_{n_2} \rangle \\ &\langle \phi_{n_2} | e^{-\frac{\beta}{M} \mathbf{H}_e} | \phi_{n_3} \rangle \langle \phi_{n_3} | e^{-\frac{\beta}{M} \mathbf{H}_o} | \phi_{n_4} \rangle \\ &\vdots \\ &\langle \phi_{n_{2M-2}} | e^{-\frac{\beta}{M} \mathbf{H}_e} | \phi_{n_{2M-1}} \rangle \langle \phi_{n_{2M-1}} | e^{-\frac{\beta}{M} \mathbf{H}_e} | \phi_{n_0} \rangle \end{aligned} \right]. \quad (5.12)$$

Thus, for finite M the quantum partition function is approximated by a path integral in imaginary time over a total of $2M$ discrete steps. Each of these steps is of size $\beta/2M$ and the total length of evolution is β . The benefit from the special breakup (5.8) is that evolution proceeds alternatingly on even and odd sites. This leads to the checkerboard representation which is shown in Fig. 5.1, where only the shaded plaquettes are of interest.

Using a classical basis the spins at each site of this $2M \times N$ lattice are either up or down. The terms in the sum of each exponential commute with each other, so the exponential operators can simply be factorised. The weight of a whole configuration is the product of all plaquette weights W_P that can be determined from the two-particle system Hamiltonian with $S = 1/2$ presented in Section 3.2. Using the eigenbasis (3.15) the quantum statistical operator of the two-particle system simply is

$$e^{-\beta \mathbf{H}} = \begin{pmatrix} e^{-\beta \frac{J}{4}} & 0 & 0 & 0 \\ 0 & e^{-\beta \frac{J}{4}} & 0 & 0 \\ 0 & 0 & e^{-\beta \frac{J}{4}} & 0 \\ 0 & 0 & 0 & e^{\beta \frac{3J}{4}} \end{pmatrix}. \quad (5.13)$$

This can be transformed back into the Ising basis (3.13). The off-diagonal elements, however, then are negative and cannot be interpreted as Boltzmann weights. Therefore a basis rotation

of 180° on one of the two sublattices (see (3.29)) must be performed before to give

$$\mathbf{U}^{-1}e^{-\frac{\beta}{M}\mathbf{H}}\mathbf{U} = e^{-\frac{\beta}{M}\frac{J}{4}} \begin{pmatrix} 1 & 0 & 0 & 0 \\ 0 & \frac{1}{2}(1 + e^{\frac{\beta}{M}J}) & -\frac{1}{2}(1 - e^{\frac{\beta}{M}J}) & 0 \\ 0 & -\frac{1}{2}(1 - e^{\frac{\beta}{M}J}) & \frac{1}{2}(1 + e^{\frac{\beta}{M}J}) & 0 \\ 0 & 0 & 0 & 1 \end{pmatrix}, \quad (5.14)$$

the matrix containing the weights of our four spin plaquettes. If bond alternation is introduced, different weights for $J = J_{e/o}$ must be considered. For each plaquette we have six non-zero matrix elements that, considering spin up/down symmetry, correspond to three different plaquette types. In terms of plaquettes the partition function becomes

$$Z = \sum_{\text{all possible configurations}} \prod_{\text{P}} W_{\text{P}}. \quad (5.15)$$

To generate a new configuration a closed loop of connected sites is constructed and flipped. Starting at an arbitrary site of spin up (down) the plaquette next to it forward (backward) in imaginary time direction will determine the loop's path.

How a loop proceeds (i.e. is constructed) on the lattice is determined by the local detailed balance restriction (5.5) on each plaquette that ensures global detailed balance. The path of the loop is predetermined at plaquettes with all four spins alike and plaquettes with diagonally altering spins. The first of these is called ‘‘forced continuation’’ (FC) as only continuous movement in imaginary time direction will result in a non-zero weight plaquette if spins along the loop are flipped. The latter is the ‘‘forced transition’’ (FT) plaquette. For the same reason as before the loop in this case is forced to jump to the adjacent site in space direction. The remaining plaquette type is called ‘‘optional decay’’ (OD) as (5.5) demands a probability of

$$p = \frac{2}{1 + e^{\frac{\beta}{M}J}}, \quad (5.16)$$

for the loop to go on in imaginary time and $1 - p$ to transit to the adjacent site in space direction. Plaquette types and loop building rules are illustrated in Fig. 5.2. The building rules ensure that the loops always close and the spin configuration is decomposed into a set of closed loops each of which can be flipped with equal probability. To be precise this is only true if no magnetic field is applied as will always be the case here. The set of closed loops is usually referred to as a graph. A typical loop building situation is shown in Fig. 5.3.

Note that our considerations are only valid for the specific case of isotropic spin interactions. For different models with, say, anisotropic spin interactions different plaquette types and different loop building rules can occur. There are two major variants of implementation of a Loop Algorithm. In the multiloop variant the entire spin configuration is decorated with closed loops as discussed above. Each loop is then flipped with a suitable probability ($1/2$ in

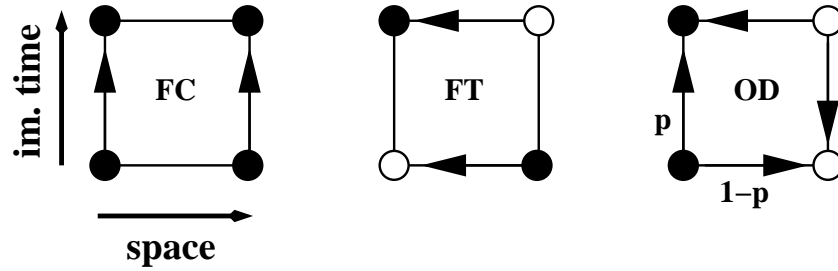


Figure 5.2: Three different plaquette types for antiferromagnetic spin chains with $S = 1/2$: FC...Forced Continuation, FT...Forced Transition, OD...Optional Decay. *Filled (open) circles* denote spin up (down). *Arrows* show the proceeding direction of a loop that enters the plaquette. The total z -component of spin is conserved on each plaquette for imaginary time evolution. If up and down spins are exchanged *arrows* must be reversed.

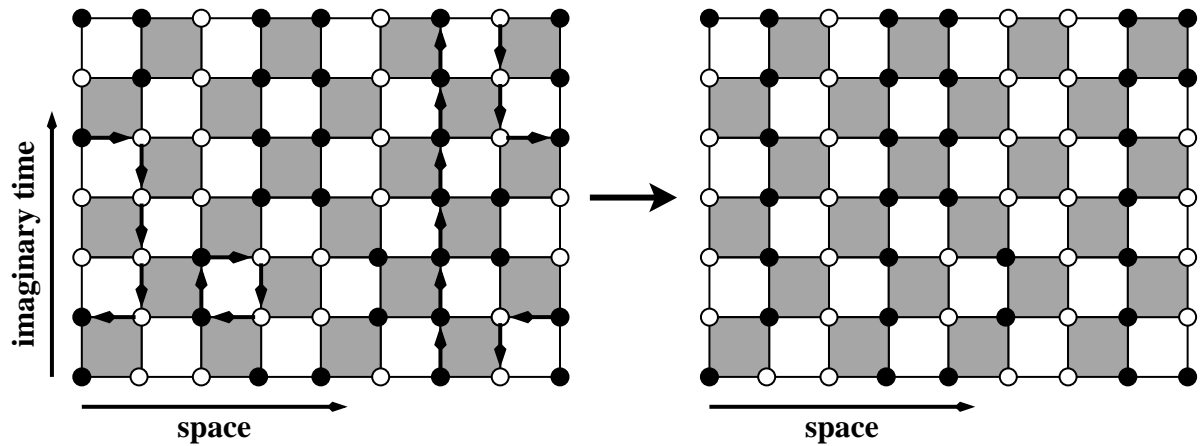


Figure 5.3: Example of loop a update. *Left*: Possible but arbitrary spin configuration of a small system with periodic boundary conditions decorated with some loops. Very small local loops can occur but also loops that wind around in spatial and temporal direction, thus allowing for change of total magnetisation. *Right*: Update result if all three loops shown are flipped. *Filled (open) circles* denote spin up (down).

our case). A slightly easier variant to implement, the single loop algorithm, creates only one single loop that is then flipped with probability one.

So far, loop building rules have only been considered for $S = 1/2$. In principle, one could determine the two-particle quantum statistical operator for any spin size and get the corresponding plaquette weights. The update process, however, poses a tricky problem as one cannot define a direction the loop has to follow. Instead, the subspin representation introduced in Section 3.3 can be used to keep working with $S = 1/2$, i.e. binary variables. The framework was developed in [55, 56] for $S = 1$ and extended to general higher spins in [53].

By introducing subspins, the interaction of two spins of size S_a and S_b is initially decomposed into $4S_a S_b$ contributing terms. For, say, $S = 1$ one can separate direct and crossed interaction terms and let them evolve in separate imaginary time steps each. If M is the Trotter

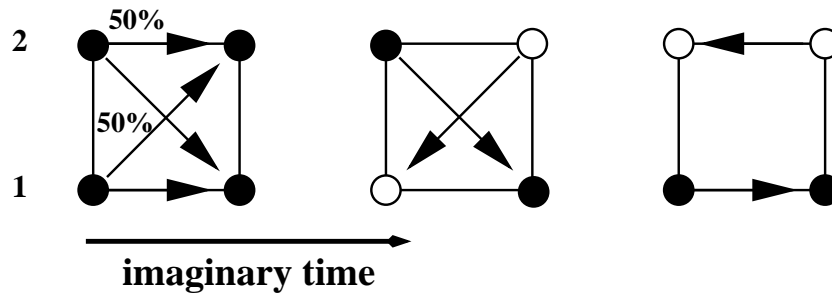


Figure 5.4: Each projector plaquette represents one spin site and its neighbour in imaginary time. *Left:* A loop that enters this kind of plaquette changes its subspin layer with probability $p = 1/2$. *Centre and right:* The loop path is predetermined as indicated. *Filled (open) circles* denote subspin up (down). Flipping all spins results in the same plaquette types with *arrows* reversed.

number, the total number of imaginary time steps then will be $4M$. To avoid unphysical states of spin a projection operator must be applied (see Section 3.3), thus introducing another time slice with projector plaquettes (see Fig. 5.4). The weights of projector plaquettes are given by the matrix elements of the projection operator (3.17). Loop building rules on projector plaquettes are of course designed to satisfy detailed balance and ergodicity. It is sufficient to project only once suitably, e.g., at the imaginary time boundary. A possible plaquette decoration is shown in Fig. 5.5a.

The situation is more intricate if mixed spins chains are to be mapped onto subspin representations as the interactions do not break into the same number of terms. In this case “deserted” subspin sites occur that do not lead into another “active” plaquette. The evolution on these sites corresponds to single particle unit operators that do not change the spin state. A loop that hits such a site must move on in imaginary time (backwards or forwards) until the next “active” plaquette is entered (see Fig. 5.5b). When $S_a = S_b$, one can simplify the simulation by simulating $2S$ spin-1/2 subsystems separately without crossed interactions and just projecting with a permutation operator once.

5.2.2 Continuous Time

The Trotter–Suzuki breakup is exact only in the limit $M \rightarrow \infty$. For finite M the overall error is of order $1/M$. Working with discrete lattices therefore implies the need of extrapolation to infinite Trotter number. This systematic error can directly be eliminated by implementing the limit in the algorithm, thus by working in continuous imaginary time. The lattice of discrete plaquettes then becomes a continuum of imaginary time extent β that consists of infinitesimally small plaquettes [8]. The storage of each lattice spin becomes obsolete. It is sufficient to record the configuration at $\tau = 0$ and store the transition times for each spin.

What happens to the loop is now determined by both neighbouring sites at once. A jump is associated with the change of imaginary time direction, thus can only occur to a site with

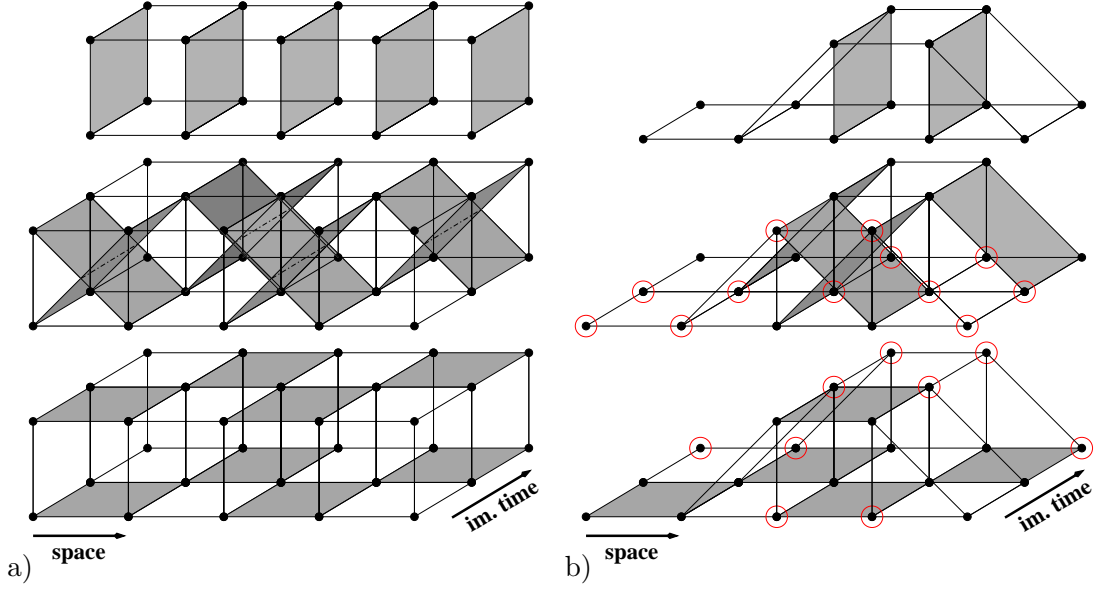


Figure 5.5: Two examples of possible plaquette decompositions. Subspins are shown on the vertical axis. *Top row:* Time slice with projector plaquettes that needs to be included only once. *Middle (bottom) row:* Plaquettes corresponding to crossed (direct) interaction terms for even and odd sites. (a) Uniform spin chain with $S = 1$. (b) Mixed spin chain with $S_a = 1/2$ and $S_b = 1$ (model **A**). Alternatingly arranging slices with direct and crossed plaquettes generates the lattice. *Circles* indicate “deserted” sites that belong only to one “active” plaquette (see text). The location of “deserted” sites on the projector plaquette slice depends on where it is inserted.

opposite spin. FC and FT of simple lattices with $S = 1/2$ remain analogous to the discrete case. As long as both neighboring sites show the same spin state (FC) a loop cannot change site and is forced to move on along imaginary time. A transition is forced (FT) to take place if two neighbouring sites change their sign at exactly the same point in time. If a site of, e.g., spin up is accompanied by one or two sites of opposite orientation (OD) the path needs to be determined stochastically. Imagining the “decay” or transition to take place somewhere inside the plaquette introduces a transition probability per unit time λ . Taking the continuum limit $\beta/M \rightarrow \infty$ gives [8]

$$\lambda_{\text{continuum}} = \lim_{M \rightarrow \infty} \frac{1-p}{\beta/M} = \lim_{M \rightarrow \infty} \left(1 - \frac{2}{1 + e^{\frac{\beta}{M}J}} \right) \frac{M}{\beta} = \frac{J}{2}. \quad (5.17)$$

Thus, optional transitions are “rare” events that are Poisson distributed along OD path segments. Consequently, time intervals between these transitions are distributed exponentially. Generalisation to spins of higher magnitude is straightforward. Each neighbouring subspin of opposite sign permits transitions with probability per unit time $p = J_{e/o}/2$. Continuous imaginary time loop building rules are illustrated in Fig. 5.6 where three pairs of neighbouring spins show generic examples of possible loop paths. Between the first two sites no transition is allowed and the loop continues in time. The next two sites provide a forced transition event. This forced transition however is not necessarily reached by an oncoming loop as optional decay

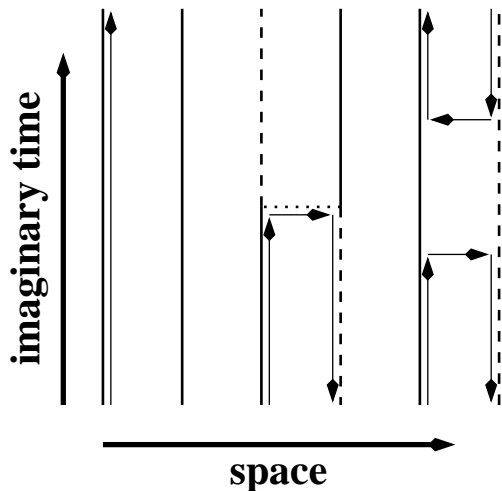


Figure 5.6: Illustration of loop building rules in continuous imaginary time.

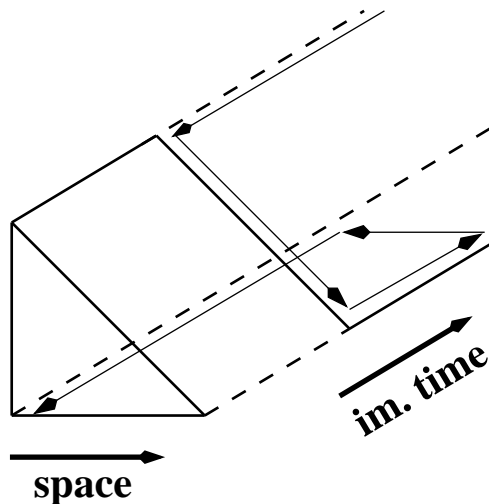


Figure 5.7: Loop path for mixed spin chains in continuous imaginary time.

is possible before. The last pair of sites indicates random transition events between sites of opposite spin due to optional decay. Figure 5.7 shows an example for mixed spin loop movement. The interaction between $S_a = 1/2$ (one subspin) and $S_b = 1$ (two subspins) adds another layer of subspins on which the loop can move. In Fig. 5.7 the loop enters from above and meets a transition that forces its further movement onto to the site with $S = 1/2$ and into reversed direction where it jumps back by optional decay but to the other subspin that time. The main difference, in fact, between spin chains of size $S = 1/2$ and mixed spin chains or uniform ones with larger spins is the lattice that allows for a richer variety of loop decomposition. Furthermore, infinitesimal projector plaquettes need to be included that imply special imaginary time boundary conditions if included at $\tau = \beta$. Wherever included, projector plaquettes mediate “spontaneous” layer shifts that follow the rules shown in Fig. 5.4.

5.2.3 Measurements and Improved Estimators

The Loop Algorithm allows for direct implementation of improved estimators [7] that show smaller variance compared to conventional Monte Carlo averages. Improved estimators use loop properties instead of configuration properties to estimate an observable A by weighted averaging over all 2^n possible configurations C_k that can be reached from a given configuration decorated with a given set of n loops $\{\mathcal{L}_1, \dots, \mathcal{L}_n\}$. So at each Monte Carlo step the weighted average of a large number of configurations is taken which improves the variance of the estimate. This is expressed by

$$A_{\text{imp}} = \sum_{k=1}^{2^n} p(C \rightarrow C_k) A(C_k), \quad (5.18)$$

where $p(C \rightarrow C_k)$ is a suitable probability of getting to configuration C_k from C . In our case $p = 1/2$ for every loop. The spin-spin correlation function in terms of improved estimators

then is

$$(S_i^z S_j^z)_{\text{imp}} = \frac{1}{2^n} \sum_{k=1}^{2^n} (S_i^z S_j^z)_k, \quad (5.19)$$

where $(\dots)_k$ denotes the value for configuration C_k , n is the number of loops. We see that only if site i and j belong to the same loop $(S_i^z S_j^z)_{\text{imp}}$ will be non-zero as in the other case the terms in the sum will cancel. To construct improved estimators of other physical quantities it is necessary to express the quantities with loop properties. This is especially simple for susceptibilities that are proportional to the square of the total magnetisation. Clearly, the total magnetisation is the sum of all loop magnetisations. Note that for antiferromagnetic interactions a loop can only show non-zero uniform magnetisation if it winds around in imaginary time. The uniform lattice magnetisation of one single loop can only take integer multiples of the total length β of the imaginary time dimension. Thus, the uniform susceptibility expressed in loop properties yields the improved estimator

$$\langle \chi_{\text{u,imp}} \rangle = \frac{\beta}{4L} \left\langle \sum_i w_\tau(\mathcal{L}_i)^2 \right\rangle, \quad (5.20)$$

where $w_\tau(\mathcal{L}_i)$ is the temporal winding number of loop \mathcal{L}_i and the sum runs over all loops. The staggered magnetisation of a single loop is (in the antiferromagnetic case) simply given by the total size of the loop and the corresponding improved estimator of the staggered susceptibility reads

$$\langle \chi_{\text{s,imp}} \rangle = \frac{1}{4\beta L} \left\langle \sum_i |\mathcal{L}_i|^2 \right\rangle, \quad (5.21)$$

where $|\mathcal{L}_i|$ denotes the size of loop \mathcal{L}_i . It is important to note that for single loop implementations of the Loop Algorithm improved estimators must be weighted with the inverse probability to pick a single loop as the sum over all loops in the above equations is evaluated stochastically. The chance to pick a single loop is $|\mathcal{L}_i|/\beta L$. So, the single loop improved estimator of the staggered susceptibility is reduced to

$$\langle \chi_{\text{s,imp}} \rangle = \frac{1}{4} \langle |\mathcal{L}_i| \rangle. \quad (5.22)$$

Improved estimators can also be constructed for other physical quantities such as the internal energy. We will, however, not use any for our analysis and refer the reader to [7, 8] for detailed background.

5.3 Algorithm In Use

A continuous time multi loop variant was used to produce data sets. After spreading optional transitions with Poisson probability all loops are identified. Measurements are performed using loop properties and configuration properties. Then each loop is flipped with probability $p = 1/2$.

The algorithm is implemented in FORTRAN code that was originally written by K. Harada² and N. Kawashima³ for the $S = 1/2$ antiferromagnetic Heisenberg model. It was extended to mixed spin chains including spins of higher magnitude by Z.-X. Xu and H. Ying⁴ and passed on to P. Crompton⁵. In cooperation with P. Crompton the author used the algorithm at the computer facilities of the Institute of Theoretical Physics at the University of Leipzig. No further extensions were included and only small changes of the code of model **B** were made for convenience. This code of model **B** was thoroughly checked and analysed by the author and the following descriptions rely on the insight gained from it.

Among other quantities that are measured, dynamic susceptibilities and the twist order parameter are of particular interest. The improved estimators of the staggered and uniform susceptibilities precisely implement (5.20) and (5.21) from above. Furthermore, the dynamic susceptibility $\chi(\pi, 2\pi/\beta)$ is measured by an improved estimator, where the imaginary length $l_j(\mathcal{L}_i; \tau_e, \tau_s)$ of each segment j in imaginary time belonging to a particular loop \mathcal{L}_i is measured as

$$l_j = \frac{e^{-i\frac{2\pi}{\beta}\tau_e} - e^{-i\frac{2\pi}{\beta}\tau_s}}{-i\frac{2\pi}{\beta}} S_j^z(\mathcal{L}_i). \quad (5.23)$$

$\tau_e - \tau_s$ is the imaginary time interval of the corresponding loop segment with constant spin orientation $S_j^z(\mathcal{L}_i)$. Unimproved estimators of the dynamic susceptibilities are implemented for $(k, \omega) = (\pi, 0)$, $(\pi, 2\pi/\beta)$, $(\pi, 4\pi/\beta)$ and $(\pi + 2\pi/L, 0)$ by

$$\langle \chi(k, \omega)_{\text{unimp}} \rangle = \frac{1}{\beta L} \left\langle \left| \sum_{r=1}^L e^{ikr} \int_0^\beta d\tau e^{i\omega\tau} S_r^z(\tau) \right|^2 \right\rangle. \quad (5.24)$$

No improved estimator, so far, has been constructed for the twist order parameter z_L . The measurement simply takes out one time slice at $\tau = \beta/2$ and calculates the expectation value of the twist operator (3.32). By averaging over all quantum Monte Carlo steps an estimate of the thermal average is obtained that for sufficiently large β equals the true twist order parameter z_L . If β is too small, contributions from excited states will also be included in the measurement. Both real and imaginary part of the complex quantity z_L are recorded. The imaginary part, however, is consistently zero throughout all measurements which is why we will always refer to the real part when using the symbol z_L .

All simulation runs started with all subspins being up. After 10^4 runs for thermalisation 10^5 updates were performed and measurements taken at each configuration. The mean value of ten successive steps was calculated and stored to finally give 10^4 values for further statistical analysis. Models **A** and **C** were simulated by P. Crompton within a temperature range of

²Kenji Harada, Dept. of Applied Analysis and Complex Dynamical Systems, Kyoto University, Japan

³Naoki Kawashima, Center for Nonlinear Studies, Toho University, Japan

⁴Zhao-Xin Xu and He-Ping Ying, Institute of Model Physics, Zhejiang University, China

⁵Peter Crompton, Institute of Theoretical Physics, Leipzig University, Germany

$T = 0.01 \dots 0.15$ for chains lengths of $L = 16, 32, 64, 128, 256$, while runs of model **B** were done by the author within the same temperature range and additional lattice size $L = 512$.

5.4 Test of the Algorithm

As the algorithm was not designed and implemented by the author himself it seemed desirable to perform test runs at certain parameter values. Ground state energy and excitation gap at $\alpha = 0$ ($J_1 = 1, J_2 = 0$) are known *a priori* for all three models as the systems decouple into $L/2$ two-particle systems if the chain length is L . Thus, by simulating larger chains better statistics is obtained but the results must remain the same. For model **B** we can therefore expect the ground state energy per spin to be $e_0 = -1.125$ for $\alpha = 0$ (see Table 3.1). Performing 10^5 measurements (after 10^4 sweeps for equilibration) with 256 pairs of spins (i.e. $L = 512$) at a temperature $T = 0.01$ produces an energy estimate of

$$e_0 = -1.124980(25), \quad (5.25)$$

in units of J_1 . The error was calculated with the jackknife method (see next Section) with an effective bin width of 200. Additionally for $J_1 = 0, J_2 = 1$ ($\alpha \rightarrow \infty$) the ground state energy per spin is $e_0 = -0.625$ (see Table 3.1). The energy estimate of the algorithm in this case is

$$e_0 = -0.624996(21). \quad (5.26)$$

Both results agree with the exact values in four digits and we can conclude that for sufficiently large statistics the algorithm produces consistent energy estimates.

For both values of α and all models we further know that the exact excitation gap must be $\Delta = 1$ in units of J_1 or J_2 , respectively. This is the gap for a simple two-particle system between the state with total magnetisation $M = 0$ and the state with $M = 1/2$. Thus, we can safely assume the dimerised models simulated at $T = 0.01$ to be in the ground state. The unimproved second-moment estimator $\xi_{\tau, \text{unimp}}$ of the imaginary time correlation length yields for $\alpha = 0$ and the same ‘‘system size’’ and number of measurements as before

$$\frac{1}{\xi_{\tau, \text{unimp}}} = \Delta_{\text{unimp}} = 1.47(50). \quad (5.27)$$

This is rather poor and no really accurate information could possibly be drawn at least for this specific value of α . In contrast, the improved estimator $\xi_{\tau, \text{imp}}$ gives

$$\frac{1}{\xi_{\tau, \text{imp}}} = \Delta_{\text{imp}} = 1.00090(76), \quad (5.28)$$

which is much more accurate, as could be expected. Yet there remains a significant difference to the exact value. Assuming that the bin width of the jackknife method is chosen sufficiently

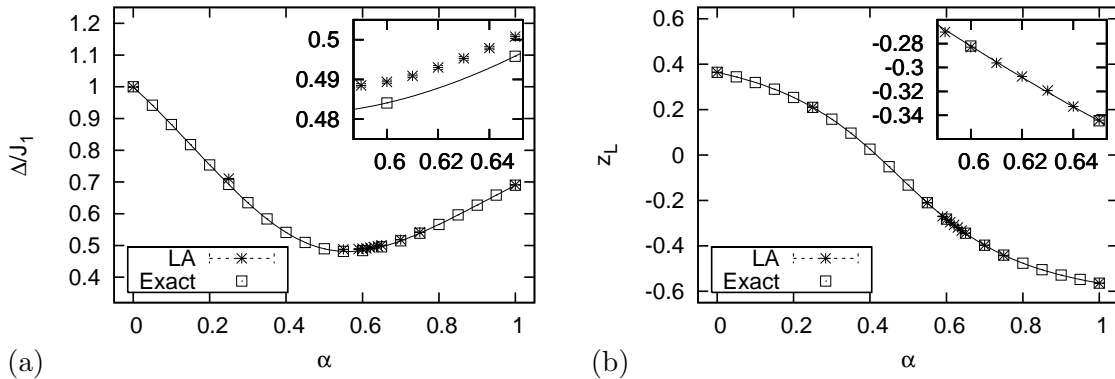


Figure 5.8: Comparison of algorithm output and exact results for model **B** of length $L = 8$ at $T = 0.01$. The *lines* represent the interpolation of 21 equally spaced data points (*boxes*) from exact diagonalisation at $T = 0$. (a) Excitation gap Δ , measured by the improved second-moment estimator $\xi_{\tau, \text{imp}}$. (b) Twist order parameter z_L .

large in order to exclude any autocorrelation effects⁶ it is most likely that this systematic difference roots back onto the second-moment definition of the correlation length estimator. Due to the low temperature and short chain length it can safely be assumed that the improved second-moment estimator is converged and will not change further at even lower temperatures.

Figure 5.8 shows the comparison of algorithm output and exact results of the excitation gap Δ and the twist order parameter z_L for a range of the coupling ratio $0 \leq \alpha \leq 1$. The system size is chosen to be $L = 8$ and the temperature is $T = 0.01$. No significant difference can be detected for z_L , while Δ exhibits a similar but larger deviation as before now for all values of α (see inset in Fig.5.8).

5.5 Analysis of Simulational Data

5.5.1 Jackknife Method

As we have seen, successive configurations created with Monte Carlo algorithms suffer from autocorrelations, thus they are not statistically independent. This must be taken into account for error estimation. A procedure to get a reasonable estimate is provided by the jackknife method [76]. The full set of N configurations is divided into n subsets of width N/n sufficiently larger than the autocorrelation time. Then a new set of n averages $A_{J,i}$ is built by successively omitting one of the subsets. These new values then should be statistically dependent with mean value

$$\langle A \rangle = \langle A \rangle_J - n(\langle A \rangle_{\text{MC}} - \langle A \rangle_J), \quad (5.29)$$

⁶The autocorrelation of the Loop Algorithm should be negligible!

with $\langle A \rangle_{\text{MC}}$ the usual Monte Carlo average and $\langle A \rangle_{\text{J}} = 1/n \sum_{i=1}^k A_{\text{J},i}$ the average over the jackknifed set of new values. The bias is given by $n(\langle A \rangle_{\text{MC}} - \langle A \rangle_{\text{J}})$. The true variance of the mean is given by

$$\Delta A = (k-1) \left(\frac{1}{n} \sum_{i=1}^n A_{\text{J},i}^2 - \langle A \rangle_{\text{J}}^2 \right). \quad (5.30)$$

As the Loop Algorithm has only very short autocorrelation anyway this seems to be too much of an effort. Usual Monte Carlo error estimates should be reliable enough. Jackknife, however, can also be applied if error estimates of complicated functions of mean values are desired. Such functions, for example, can be interpolations of data sets to find zeroes. The interpolation of statistical data with errors is possible. It is, however, much easier to perform standard interpolations, that neglect the error estimates of the data points, on jackknifed subsets and then estimate errors of parameters with the jackknife error formula. Furthermore, (5.29) signals a bias if $\langle A \rangle_{\text{MC}} \neq \langle A \rangle_{\text{J}}$. Such a bias can be due to measuring while the system has not yet equilibrated.

5.5.2 Finite-Size Scaling

Computer simulations and experiments are naturally restricted to finite size. While in experiments, however, the system size can very often be considered approximately infinite, the length scale of simulations almost certainly gives rise to significant finite size effects. Periodic boundary conditions only exclude surface effects but do not change the situation in terms of system size. Finite-size scaling [79, 80] is a powerful method to extract infinite system information from finite-size data. An introduction into scaling and finite-size scaling can be found for example in [38], Chapter 5, which the beginning of this section is partly based on.

True singularities at critical points can only occur in the thermodynamic limit. In finite systems these singularities are rounded to some finite values and shifted, thus for diverging quantities A , peaks can be located. The well-established theory of finite size scaling states that the height of the peaks grows as

$$A_{\text{max}}(L) \sim L^{\varrho/\nu}, \quad (5.31)$$

where L is the linear system size, ν is the critical exponent of the correlation length and the physical quantity A diverges as $\sim |\alpha - \alpha_c|^\varrho$ upon approaching the critical point. Furthermore the peaks will be shifted by a factor $\sim L^{-1/\nu}$. Defining pseudo-critical points $\alpha^*(L)$ such that the function $A(\alpha, L)$ attains its maximum at $\alpha = \alpha^*(L)$, we can relate them to the true critical point α_c by

$$\alpha^*(L) = \alpha_c + bL^{-1/\nu}, \quad (5.32)$$

with b , a constant. Remarkably, the above relation implies for the shift behaviour the same dependence on L for all diverging physical quantities. This is true for most systems and observables, but not necessarily for all. Take the pseudo-critical points defined by the zero

points of the twist order parameter. Clearly, the diverging quantity in this case should be the first derivative, yet peaks of the slope of the twist order parameter do not coincide with the zero points. We will, however, apply finite-size scaling analysis to the zero points definition and cannot *a priori* assume that they shift according to (5.32) but rather introduce the more general relation

$$\alpha^*(L) = \alpha_c + bL^{-\theta}, \quad (5.33)$$

with θ the shift exponent.

The relations stated so far are true only at $T = 0$. By quantum–classical mapping the imaginary time direction then is infinite and a quantum chain of finite length L has effective dimension z . The simulational measurements, however, are carried out at $T > 0$ and therefore the effective dimension of the system is zero. In order to derive valid finite-size scaling arguments, we need to investigate the influence of non-zero temperature. We know that the temperature enters as an inverse length to the power z . Thus, the homogeneity law for the singular part of the free energy density f of a classical system in d dimensions [81, 82],

$$f(|r|) = \lambda^{-d} f(|r| \lambda^{1/\nu}), \quad (5.34)$$

where λ is the scale factor and $r = \alpha - \alpha_c$, can be generalised to quantum systems at non-zero temperatures [72]:

$$f(|r|, T) = \lambda^{-(d+z)} f(|r| \lambda^{1/\nu}, T \lambda^z). \quad (5.35)$$

The scaling relation for the correlation length ξ reads (see [38], p. 196):

$$\xi(|r|) = \lambda \xi(|r| \lambda^{1/\nu}). \quad (5.36)$$

Choosing $\lambda = L$ this relation is exploited within the method of finite-size scaling, which can also be expressed by

$$\xi(|r|, L^{-1}) = \lambda \xi(|r| \lambda^{1/\nu}, L^{-1} \lambda). \quad (5.37)$$

This defines a generalised homogeneous function. Additionally incorporating T as argument, analogously to the free energy density, we arrive at

$$\xi(|r|, L^{-1}, T) = \lambda \xi(|r| \lambda^{1/\nu}, L^{-1} \lambda, T \lambda^z), \quad (5.38)$$

which we will assume to hold in the vicinity of a (quantum) quantum critical point. Note that for the correlatin length the dimension d does not enter the scaling relation. Choosing $\lambda = |r|^{-\nu}$, we obtain

$$\begin{aligned} \xi(|r|, L^{-1}, T) &= |r|^{-\nu} \xi\left(1, L^{-1} |r|^{-\nu}, T |r|^{-z\nu}\right) \\ &= |r|^{-\nu} \tilde{\xi}\left(1, \frac{\xi(|r|)}{L}, \frac{\xi_\tau(|r|)}{\beta}\right). \end{aligned} \quad (5.39)$$

In the second line we have used that $|r|^{-\nu} \sim \xi(|r|)$, and $|r|^{-z\nu} \sim \xi_\tau(|r|)$, where $\xi(|r|)$ and $\xi_\tau(|r|)$ are the spatial and temporal correlation lengths of the infinite chain at $T = 0$. If the chain length L and the inverse temperature β are much larger than the corresponding correlation lengths, the scaling function $\xi(1, y, z)$ will reduce to a mere proportionality constant:

$$\xi(1, y, z) \approx \xi(1, 0, 0). \quad (5.40)$$

Clearly, this is not valid close to the critical point where the true correlation lengths of the infinite chain at $T = 0$ exceed L and β . By choosing $\lambda = L$ and $\lambda = T^{-1/z} = \beta^{1/z}$ in (5.38), respectively, we obtain the finite-size scaling ansatz relations

$$\xi(|r|, L^{-1}, \beta^{-1}) = L \xi\left(|r| L^{1/\nu}, 1, \frac{L^z}{\beta}\right), \quad (5.41)$$

and

$$\xi(|r|, L^{-1}, \beta^{-1}) = \beta^{1/z} \xi\left(|r| \beta^{1/z\nu}, \frac{\beta^{1/z}}{L}, 1\right). \quad (5.42)$$

There are two possible ways to proceed now. The usual and actually more exact way is to choose a constant aspect ratio L^z/β which renders the two above equations equivalent. The other one is to assume either L or β infinite. For either way we choose we end up with the well-known finite-size scaling ansatz

$$\xi(|r|, L^{-1}, T) = \text{const.} \times L \tilde{\xi}\left(|r| L^{1/\nu}\right), \quad (5.43)$$

where $\tilde{\xi}$ is the proper scaling function that only depends on the scaling variable $|r| L^{1/\nu}$. This relation strictly holds for the aspect ratio L^z/β kept at a suitable constant value and is asymptotically true for $\beta \gg L^z$. If in contrast $L \gg \beta^{1/z}$, the ansatz is modified to

$$\xi(|r|, L^{-1}, T) = \text{const.} \times \beta^{1/z} \tilde{\xi}\left(|r| \beta^{1/z\nu}\right). \quad (5.44)$$

This way we are equipped with a tool to do finite-size scaling analysis by either varying the chain length or the inverse temperature while the other is kept at large fixed value. The extent to which the analysis is approximately valid is signalled by the dependence of the correlation length on L or β . As long as the measured value of the correlation length depends linearly on either L or β the system does not yet “realise” that the dimension that is kept constant is actually finite.

If L and β are of comparable size we need to be careful as the location of the peaks may certainly be influenced. As soon as, say L , becomes larger than β – the above assumption of a linear dependence of the correlation length on L for a fixed value of β then is not valid anymore anyway – the shift of the pseudo-critical points will be blocked and, of course, not approach the true critical value anymore. If and how this modification of the shift depends

on the ratio L/β we cannot tell. Taking the derivative of (5.39) with respect to α yields a condition for the location of the maxima

$$\xi\left(1, \frac{|r_{\max}|^{-\nu}}{L}, \frac{|r_{\max}|^{-z\nu}}{\beta}\right) + |r|^{-\nu} \left(\frac{\xi_y^{(\max)}}{L} + \frac{\xi_z^{(\max)}}{\beta} |r|^{-\nu(z-1)}\right) = 0, \quad (5.45)$$

where $\xi_{y/z}^{(\max)}$ stands for the derivative of $\xi(1, y, z)$ from (5.39) with respect to y/z at $r = r_{\max}$. We now assume $z = 1$, and that (5.39) is proportional to L to get

$$|r_{\max}|^{2\nu} \sim \frac{1}{L} \left(\frac{\xi_y^{(\max)}}{L} + \frac{\xi_z^{(\max)}}{\beta_0}\right), \quad (5.46)$$

for constant inverse temperature β_0 . If instead the chain length is kept constant at $L = L_0$ the growth of the maxima is proportional to β leading to an analogous relation

$$|r_{\max}|^{2\nu} \sim \frac{1}{\beta} \left(\frac{\xi_y^{(\max)}}{L_0} + \frac{\xi_z^{(\max)}}{\beta}\right). \quad (5.47)$$

Note that as we assume $z = 1$ this discussion also applies for the temporal correlation length ξ_τ .

The values of $\xi_{y/z}^{(\max)}$ are yet not independent of L and β . We know that in the limit $\beta_0 \rightarrow \infty$ relation (5.43) must be recovered and that for finite β_0 , r_{\max} cannot become arbitrarily small. In principle we could make approximate assumptions on the L - and β -dependence of $\xi_{y/z}^{(\max)}$ in order to use (5.46). Functions thus resulting, however, lead to extremely ill-posed non-linear fits and are therefore not exploited in the present study. We will rather rely on (5.32) and (5.33), respectively, for data points where the condition of linear dependence of the correlation length on L or β holds sufficiently well.

Consequently, the second order finite-size scaling relation which we will fit the pseudo-critical points to reads

$$\alpha^*(l) = \alpha_c + \frac{b}{l^\theta}, \quad (5.48)$$

where $l = L$ (or β) with β (or L) assumed to be sufficiently large for the influence on the shift to be neglected. The critical coupling ratio α_c , the shift exponent θ , and b are the fit parameters. This gives a non-linear three-parameter fit that in general tends to be unstable but still not as ill-posed as fits potentially derived from (5.46). One of the parameters can be eliminated by subtracting two equations for different values of l ,

$$\Delta\alpha := \alpha^*(l_1) - \alpha^*(l_2) = \frac{b}{l_1^\theta} - \frac{b}{l_2^\theta}. \quad (5.49)$$

Rewriting this, we get

$$\Delta\alpha = \frac{b}{l_1^\theta} \left(1 - \left(\frac{l_1}{l_2}\right)^\theta\right). \quad (5.50)$$

Choosing a constant ratio $l_1/l_2 = 1/2$, and taking the logarithm gives

$$\log \Delta\alpha = -\theta \log l_1 + \log \left(b - \frac{b}{2^\theta}\right). \quad (5.51)$$

This is a linear fit with slope $-\theta$. The shift exponent can be extracted this way. The remaining scaling fit is a more stable two parameter fit that can be used to determine the critical coupling ratio.

By following the ideas of [83] further trial fit functions have been designed to test for dominant asymptotic behaviour in $1/L$ or $\log(L)/L^2$ (for $\beta \approx \infty$),

$$\alpha_c(L) = \alpha_c + a/L + b/L^\theta, \quad (5.52)$$

$$\alpha_c(L) = \alpha_c + a/L + b \log(L)/L^2. \quad (5.53)$$

The parameters θ , a and b are strongly correlated which basically means that a slight change in, say, θ can be undone by a corresponding changes in a and b . This leads to huge error estimates in particular for a and b . Calculating θ separately using (5.51) gives an estimate which can be fed especially into (5.48) but also into (5.52). The remaining parameters then show smaller correlations. However, one needs to keep in mind that the uncertainty in θ obtained from (5.51) is not reflected by those fits, and that the linear procedure described above is, in fact, not valid for $a \neq 0$:

$$\alpha_c(L) = \alpha_c + b/L^{\theta^{(lin)}}, \quad (5.54)$$

$$\alpha_c(L) = \alpha_c + a/L + b/L^{\theta^{(lin)}}. \quad (5.55)$$

Furthermore, in order to stabilise the fit, the value of θ obtained from (5.48) can be fed into (5.52):

$$\alpha_c(L) = \alpha_c + a/L + b/L^{\theta^{(1)}}. \quad (5.56)$$

This set of trial fit functions – among others – has been applied with “full force” to pseudo-critical points determined from the twist order parameter and the second- and fourth-moment estimators of the correlation lengths at various temperatures. The underlying assumption of a single line of true critical points that extends into regions of non-zero temperature is, however, not supported by the data that clearly show saturating correlation lengths. The output of this procedure is tabulated in Appendix A.

Chapter 6

Results of Model B

After having explained the basic ideas in order to understand the models and the methods of data production and analysis, the results of model **B** will be presented and carefully discussed in this chapter.

Starting out with the twist order parameter in Section 6.1 the first estimates of the critical coupling ratio α and the shift exponent θ are shown. We identify a temperature induced effect that clearly indicates the breakdown of scaling at non-zero temperatures. This breakdown is confirmed in Section 6.2 where the results of the analysis of both the spatial and imaginary temporal correlation lengths are shown and discussed. The staggered susceptibility is briefly discussed in Section 6.3. In Section 6.4 a few results from the usual finite-size scaling analysis with constant aspect ratio are presented, which completes this chapter.

All estimates discussed in this and the next chapter have been obtained from 10^5 measurements after 10^4 sweeps for equilibration (see Section 5.3).

6.1 Twist Order Parameter

As mentioned in Section 5.3, the twist order parameter does not exactly measure the ground state property but a thermal average. Thus, we expect to see temperature effects as soon as the energy gap becomes comparable to the temperature. We do not *a priori* know that the twist order parameter is pushed to zero by averaging over low-lying excited states and therefore cannot predict that at non-zero temperatures z_L vanishes with increasing chain length.

In Fig. 6.1 we see the behaviour of the twist order parameter z_L as a function of α for two different temperatures and chains lengths $L = 16, \dots, 512$. The expected smooth change of sign is accurately reproduced. The locations of zero points that define pseudo-critical points of finite systems could be determined precisely by means of jackknifed cubic spline interpolation for all temperatures as high as $T = 0.075$. This might – against all odds and better knowledge – tempt to apply the machinery of scaling functions derived in Section 5.5.2 at various non-zero

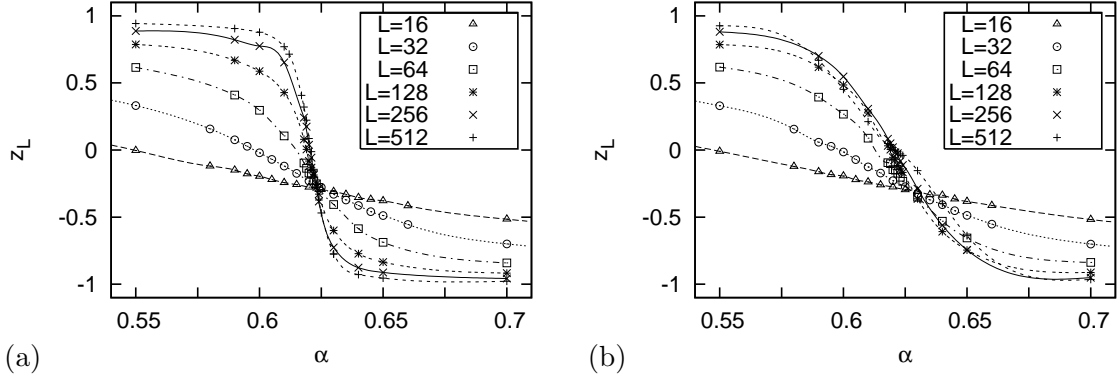


Figure 6.1: Twist order parameter z_L as function of the coupling ratio α . *Lines* are simple interpolations to guide the eye. (a) $T=0.01$, (b) $T=0.025$.

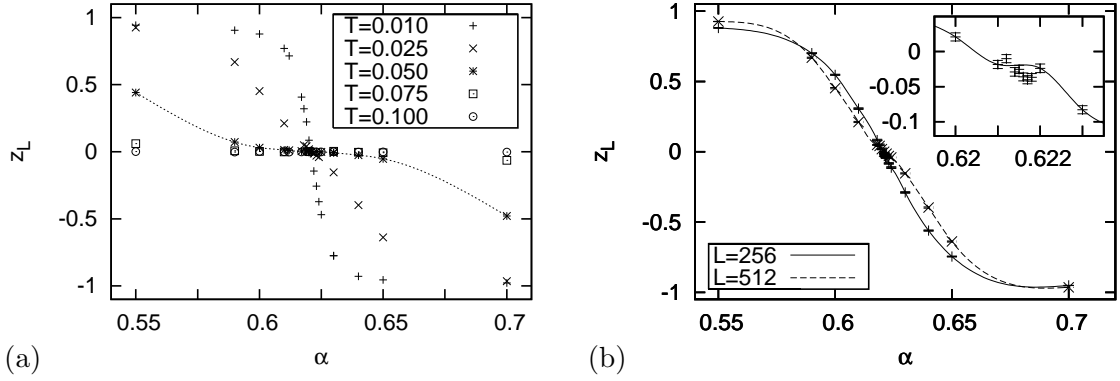


Figure 6.2: Temperature induced formation of a plateau in $z_L(\alpha, T)$. (a) $L=512$, the *dotted line* emphasises the temperature effect at $T = 0.05$. (b) $T = 0.025$, comparison of temperature effect for two different chain lengths. For $L = 256$ the *inset* shows additional data points between $\alpha = 0.621$ and $\alpha = 0.622$, whereas the interpolating *line* does not consider those points in between. While for $L = 512$ the beginning of a plateau-like shape is clearly visible it can be hardly resolved for $L = 256$.

temperatures. “Shift exponents” and “critical coupling ratios” resulting from this “brute-force” analysis are listed in Appendix A.

The careful reader, however, might have noticed in Fig. 6.1b that the slope of $z_L(\alpha)$ for $L = 512$ is not monotonic anymore, indicating a temperature effect that is shown in Fig. 6.2. For the longest chain with length $L = 512$ this temperature induced plateau-like shape of the twist order parameter as a function of α becomes apparent at temperature $T = 0.05$ (dotted line in Fig. 6.2a). The plateau might indicate that for small but sufficiently large temperatures it is possible that there exists a finite interval of α for which the twist order parameter z_L becomes zero. This, of course, would make the definition of pseudo-critical points as the zeros of $z_L(\alpha)$ problematic as no zeros could possibly be located anymore. Even if the detection of zeros, however, is still feasible the building of the plateau-like shape will certainly influence the

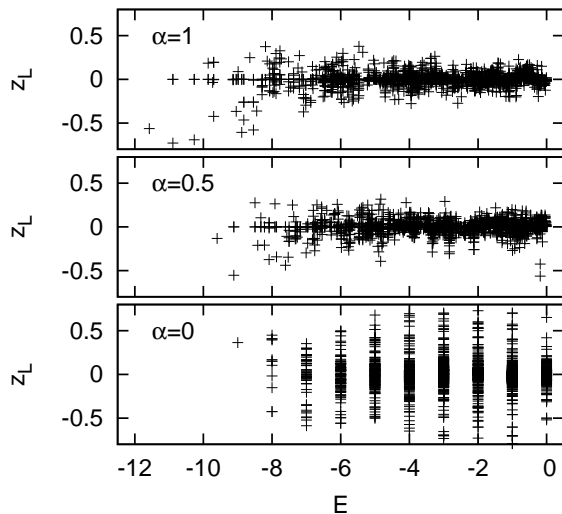


Figure 6.3: Exact spectrum of the twist order parameter of model **B** with $L = 8$ for three different values of the coupling ratio and energies lower than zero. For sufficiently large temperatures excited states will contribute to the thermal average of $z_L(\alpha, T)$ and eventually push it to zero. The structure of the low energy spectrum and the twist order parameter value of low-lying excited states is of crucial importance for the temperature behaviour of z_L .

location of the zeros we are interested in. Yet we can hope that this influence remains small in the lowest temperature regions measured. Figure 6.2b shows a close-up of what is possibly a very small plateau of the chain with $L = 256$ at $T = 0.025$. Its influence on the location of the zero point might be within the statistical accuracy of the analysis.

Any temperature effect in the measured quantity $z_L(\alpha, T)$ is clearly due to low-lying excited states. Consequently, by measuring the thermal average one gathers information about the structure of these low-lying excited states. Figure 6.3, where the exact twist order parameter spectrum of model **B** is shown for a chain of length $L = 8$, illustrates how low-lying excited states influence the thermal average of z_L . For, e.g., $\alpha = 1$ the twist order parameter will take on a negative non-zero value up to a certain temperature. For $\alpha = 0$ this value will be positive up to a certain temperature that, however, will be a different one since the first set of excited states already spreads around zero. Unfortunately, we do not know the exact values of z_L for excited states of larger systems and thus to extrapolate this picture in particular to the thermodynamic limit remains pure speculation. Yet we have seen in Fig. 6.2 that a plateau-like shape develops with increasing temperature and increasing lattice size that eventually might replace any defined zero point of $z_L(\alpha)$ by an interval of non-zero measure where $z_L \equiv 0$. In order to quantify this assumption we need to investigate the slope of $z_L(\alpha)$ and therefore define the susceptibility-like quantity

$$\chi_{z_L}(\alpha, T) = \frac{\partial z_L(\alpha, T)}{\partial \alpha}. \quad (6.1)$$

It can be expected that $\chi_{z_L}(\alpha = \alpha^*, T)$ develops maxima that, in principle, could be used to determine the points of crossover “ α_c ” (or critical points if there are any) at non-zero temperature if they appear at finite and non-zero values of α . We will, however, not proceed in this direction as the slopes of z_L could only be determined rather inaccurately and remain on a qualitative level. The slopes of the zero points could be estimated from the cubic splines themselves if the interpolation was sufficiently smooth, otherwise line fits of data points close

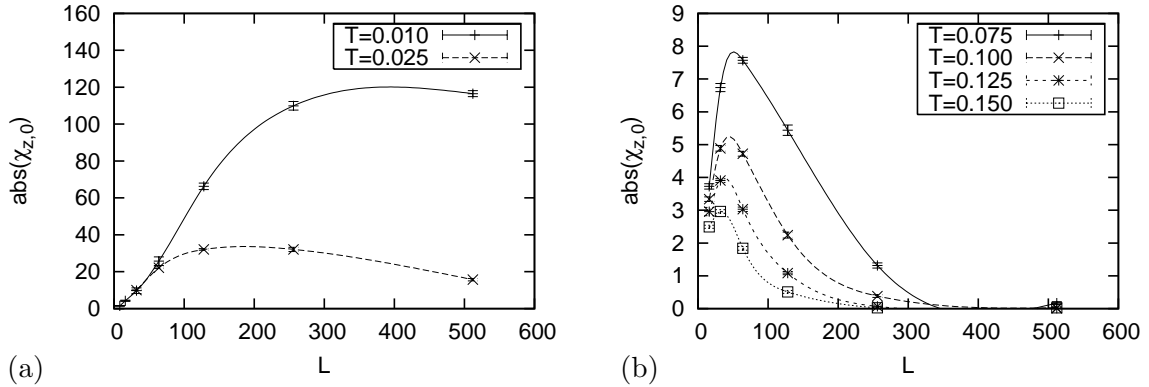


Figure 6.4: Temperature and system size dependence of the twist order parameter’s slope at the zero point. For higher temperatures the breakdown of “divergence” happens at smaller chain lengths. *Lines* are simple interpolations to guide the eye.

to the zero transitions were used. The results are shown in Fig. 6.4. For smaller temperatures the peaks that can be seen shift to longer chains. Obviously the slope vanishes for large L and relatively high temperatures (Fig. 6.4b), but also for low temperatures (Fig. 6.4a) it is reasonable to expect that for sufficiently long chains the slope will eventually become zero. The value of L at which the maximum slope at a given temperature occurs seems to depend linearly on the temperature. This is illustrated in Fig. 6.5 where the data points are roughly estimated from the interpolation curves in Fig. 6.4. A linear fit gives the approximate relation

$$L \approx 4\beta, \quad (6.2)$$

which can be used to determine which values of L are considered to be low (or high) at a given inverse temperature β .

Let us now discuss the results of the analysis of zero points. Table 6.1 shows the results of non-linear least χ^2 fits to trial fit function (5.48) performed with Levenberg-Marquardt routines from Numerical Recipes [63]. Errors are estimated by the diagonal elements of the covariance matrix. All estimates of the critical coupling ratio α_c are surprisingly consistent. By

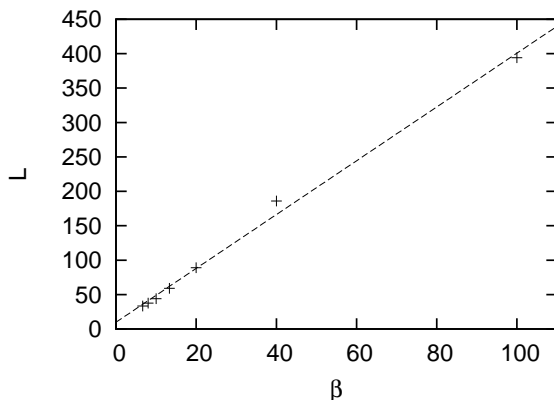


Figure 6.5: Chain length L and inverse temperature β at which the maximum absolute value of the slope $|\chi_{z_L,0}|$ at the zero point of the twist order parameter occurs. Data points are roughly estimated from the interpolations of Fig. 6.4. The linear fit (*dashed line*) gives a slope of ≈ 4 . Chain lengths below (above) the *dashed line* are considered to be small (large) relative to a given inverse temperature.

Table 6.1: Results of fitting the pseudo-critical points of the twist order parameter to the finite-size scaling relation without corrections (5.48) at constant temperature $T = 0.01$. $L \dots$ chain lengths included in the fit, $\alpha_c \dots$ fit parameter – critical coupling ratio, $b \dots$ fit parameter, $\theta \dots$ fit parameter – shift exponent, $\chi_{\text{pdof}}^2 \dots$ chi-squared per degree of freedom; $\theta^{(\text{lin})} \dots$ shift exponent from linear fit (see Section 5.5.2).

L	α_c	b	θ	χ_{pdof}^2	$\theta^{(\text{lin})}$
8–512	0.6213(1)	-6.0(3)	1.60(2)	3.96	1.64(4)
8–256	0.6214(2)	-5.7(4)	1.59(2)	4.01	1.65(6)
8–128	0.6219(3)	-5.2(4)	1.55(3)	1.41	1.55(3)
8–64	0.6224(8)	-5.1(5)	1.53(4)	2.36	1.54(5)
16–512	0.6212(1)	-7.2(6)	1.66(3)	1.63	1.68(5)
32–512	0.6211(1)	-9.2(1.8)	1.73(6)	1.24	1.70(9)
64–512	0.6210(2)	-18.7(10.8)	1.89(15)	0.80	1.72(18)

successively omitting the longer chains in the scaling fits, the value of the critical coupling ratio increases slightly while the shift exponent decreases. This suggests that by measuring at too high temperature the location of the zeros of the twist order parameter is maybe systematically underestimated. The fit of pseudo-critical points up to $L = 128$ seems to give the best result in the sense that in this case the estimate of the shift exponent from non-linear and linear procedure are perfectly consistent. Figure 6.6 shows the temperature dependence of the pseudo-critical points. For chain lengths as large as $L = 256$ it is possible that within the level of accuracy the points determined at the lowest temperature of $T = 0.01$ represent the true zero temperature value, i.e. that no significant change will be detected when further lowering T . Even for $L = 512$, where there is a clearly visible temperature related drift for $T \geq 0.030$, the value might still be reliable within the range of accuracy. Thus, we might conclude that the fit that includes the pseudo-critical points of all chain lengths is still meaningful.

Table 6.2 shows the results of trial fit function (5.52) with a linear correction term in $1/L$. The correction terms a are not consistently non-zero for fits that include small chain lengths

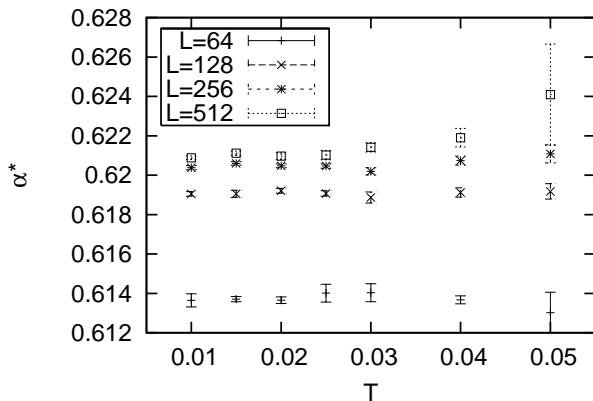


Figure 6.6: Temperature dependence of pseudo-critical points determined from the location of zero points of the twist order parameter.

Table 6.2: Results of fitting the pseudo-critical points of the twist order parameter to the finite-size scaling relation with corrections in $1/L$, (5.52), at constant temperature $T = 0.01$. $L \dots$ chain lengths included in the fit, $\alpha_c \dots$ fit parameter – critical coupling ratio, $a \dots$ fit parameter fo the correction term that is linear in $1/L$, $b \dots$ fit paramter, $\theta \dots$ fit parameter – shift exponent, $\chi_{\text{pdof}}^2 \dots$ chi-squared per degree of freedom.

L	α_c	a	b	θ	χ_{pdof}^2
8–512	0.6207(3)	0.48(20)	-4.9(3)	1.40(6)	1.01
8–256	0.6202(5)	0.84(45)	-4.9(2)	1.33(9)	0.64
8–128	0.6205(14)	0.67(84)	-4.9(3)	1.36(16)	1.23
16–512	0.6208(3)	0.28(22)	-5.5(8)	1.49(10)	0.94
32–512	0.6208(5)	0.29(56)	-5.5(3.2)	1.49(32)	1.87

Table 6.3: Same as Table 6.2 but fitted to (5.55) with fixed exponent θ from Table 6.1 (see Section 5.5.2).

L	α_c	a	b	$\theta^{(1)}$	χ_{pdof}^2
8–512	0.6212(2)	0.025(26)	-6.1(2)	1.60	3.72
8–256	0.6213(2)	0.025(35)	-5.9(2)	1.59	3.82
8–128	0.6219(4)	0.009(51)	-5.3(3)	1.55	1.40
8–64	0.6222(12)	0.015(93)	-5.1(4)	1.53	2.34
16–512	0.6211(2)	0.012(29)	-7.3(3)	1.66	1.57
32–512	0.6211(2)	0.005(40)	-9.3(6)	1.73	1.23
64–512	0.6210(2)	-0.007(64)	-18.4(2.8)	1.89	0.78

which does actually not support the idea the is a corresponding correction term. Remarkably, the fit that includes the chain lengths $L = 8, \dots, 64$ only (not listed in Table 6.2) produces a shift parameter $\theta = 1.06(32)$, which does indicate that for small chain lengths there is indeed a dominant linear behaviour in $1/L$. Yet the fit in this case is a four parameter fit of four data points which is why error estimates are rather questionable and $\chi_{\text{pdof}}^2 = 0$ by definition. In any case, fits to (5.52) produce smaller shift exponents and slightly smaller estimates of the critical coupling. For comparison the results of fits to (5.55) that uses the shift exponent from (5.48) are shown in Table 6.3. It can be seen that the correction terms a are much smaller and consistently zero when error estimates are taken into account for all fits. This means that after fitting to the uncorrected finite-size scaling relation (5.48) the term linear in $1/L$ is not accepted. The asymptotic convergence is dominated by the term that includes the shift exponent.

In summary of the most significant results, we obtain a critical coupling ratio

$$\alpha_c = 0.6219(3), \quad (6.3)$$

and a shift exponent that yields the critical exponent ν of the correlaion length if $\theta = 1/\nu$

holds for the zeros of the twist order parameter,

$$\theta = 1.55(3) \xrightarrow{(5.32)} \nu = 0.65(2), \quad (6.4)$$

if chain lengths $L \leq 128$ are, considered and

$$\alpha_c = 0.6210(2), \quad (6.5)$$

and

$$\theta = 1.89(15) \xrightarrow{(5.32)} \nu = 0.53(5), \quad (6.6)$$

if chain lengths $L \geq 64$ are considered. Estimates of ν clearly only hold if the shift of the zero locations is indeed proportional to $L^{-1/\nu}$. Recalling relation (3.41) indicates that the second value of α_c is more significant which is also supported by the fits to (5.52) listed in Table 6.2 that produce slightly lower but consistent estimates. The analysis, however, is inconclusive in terms of the shift exponent, yet we can conclude that a corresponding estimate of ν leads to a value significantly smaller than one. In the following we will look at the correlation lengths where we can expect the shift exponent to be $1/\nu$ and compare the results.

6.2 Correlation Lengths

We will discuss the analysis of the second- and fourth-moment estimators of the imaginary time correlation length ξ_τ , and the second-moment estimator of the spatial correlation length ξ in this section. Wherever possible, improved estimators have been fed into the definitions of the estimators, i.e. $\chi_{\text{imp}}(\pi, 0)$ and $\chi_{\text{imp}}(\pi, 2\pi/\beta)$ have been used to calculate the improved second-moment estimator $\xi_{\tau, \text{imp}}^{(2)}$ whereas $\chi_{\text{unimp}}(\pi, 4\pi/\beta)$ had to be used to give a partly improved fourth-moment estimator $\xi_{\tau, \text{part}}^{(4)}$. Similarly, due to the lack of the corresponding improved estimator, the spatial correlation length is represented by the partly improved second-moment estimator $\xi_{\text{part}}^{(2)}$ that uses $\chi_{\text{imp}}(\pi, 0)$ and $\chi_{\text{unimp}}(\pi + 2\pi/L)$. Throughout this analysis, position and height of peaks have been determined by fitting data points around the maximum to even fourth-order polynomials using the Levenberg–Marquardt method [63]. All errors are, again, estimated by the diagonal elements of the covariance matrix.

6.2.1 Imaginary Time Correlation Length at Fixed Temperature

In Figs. 6.7 and 6.8 we see the improved second-moment and the partly improved fourth-moment estimator of the imaginary time correlation length, respectively. The fourth-moment estimator involves smaller systematic errors and the higher values therefore are more accurate in that sense. But the use of unimproved estimators renders its statistical error estimates larger, making an exact localisation of the peaks more inaccurate. The growth of the correlation length with growing chain length L is limited depending on the temperature that is kept fixed. It can

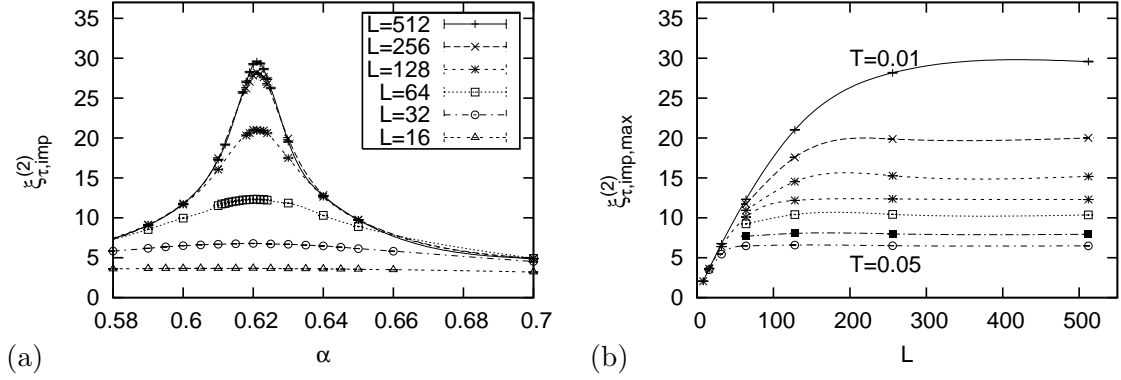


Figure 6.7: Improved second-moment estimator of the imaginary time correlation length ξ_{τ} at fixed temperature. *Lines* are simple interpolations to guide the eye. (a) Dependence on the coupling ratio α for various chain lengths L at $T = 0.01$ ($\beta = 100$). (b) Height of the maxima against L for $T = 0.01, 0.015, 0.02, 0.025, 0.03, 0.04, 0.05$ ($\beta = 100, \dots, 20$).

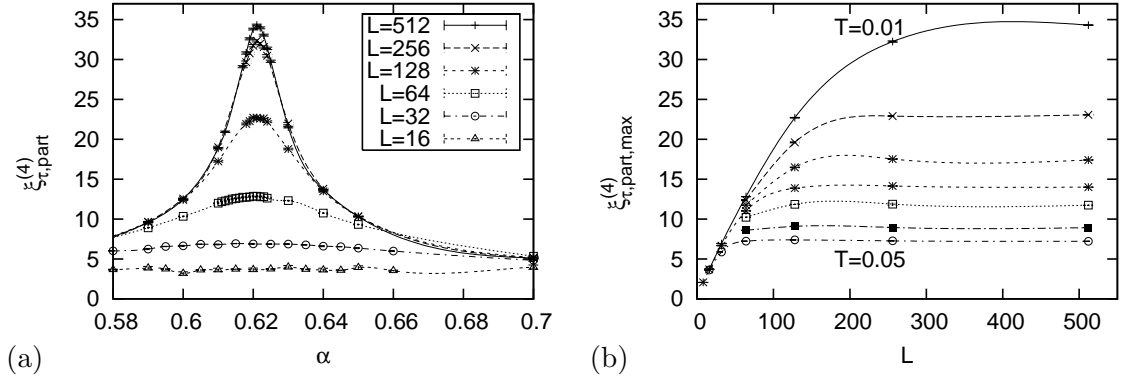


Figure 6.8: Same as Fig. 6.7, but for the partly improved fourth-moment estimator.

be seen and checked numerically that for $\beta = 100$ ($T = 0.01$) the expected linear dependence on L (5.31) is – at most – reproduced by chain lengths up to $L = 64$ which leaves four data points to be fitted in order to extract the value of the exponent ν . This is, in fact, not surprising. A chain length $L = 128$ exceeds the length of the imaginary time direction $\beta = 100$ and significant limitation effects are to be expected. Even for $L = 64$ the imaginary time direction is not really long enough and the linear dependence is not very well reproduced. A fit proportional to L^x that includes the four smallest chains ($L = 8, \dots, 64$) gives $x = 0.88(2)$ with $\chi_{\text{pdof}}^2 = 0.003$ if error estimates are not considered, i.e. all errors are set to unity, and even worse results if error estimates are included. Nonetheless, the remaining four data points have been fed into the finite-size scaling fits derived in Section 5.5.2 the result of which is shown in Fig. 6.9. Fitting to (5.48) with $l = L$ gives the critical coupling ratio for the improved second-moment estimator of the imaginary time correlation length

$$\alpha_c = 0.6216(2), \quad (6.7)$$

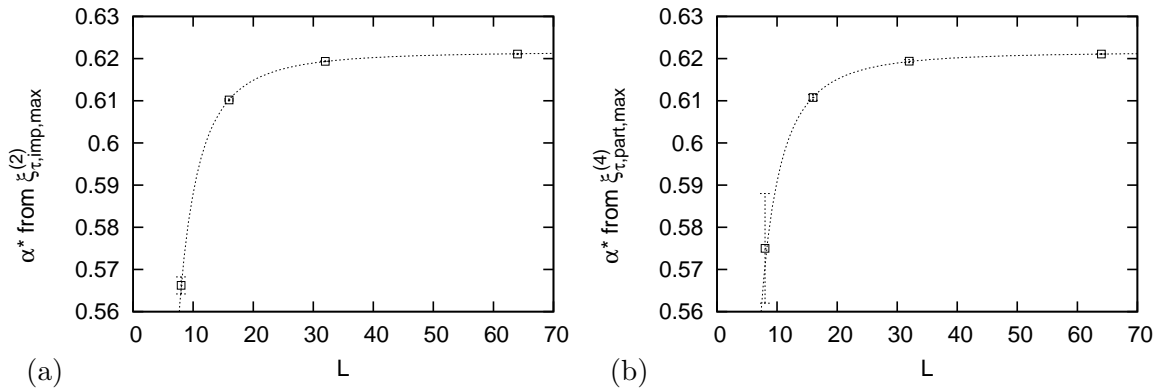


Figure 6.9: Peak locations of the imaginary time correlation length ξ_τ at fixed $\beta = 100$ ($T = 0.01$). Lines show fits to the finite-size scaling function (5.48). (a) Improved second-moment estimator. (b) Partly improved fourth-moment estimator.

and the corresponding shift exponent

$$\theta = 2.3(1) \quad \longrightarrow \quad \nu = 0.43(2). \quad (6.8)$$

For the partly improved fourth-moment estimator we get

$$\alpha_c = 0.6216(3), \quad (6.9)$$

and

$$\theta = 2.2(3) \quad \longrightarrow \quad \nu = 0.45(7). \quad (6.10)$$

While the estimates of the critical coupling ratio are very close to those determined from the twist order parameter, the shift exponent seems to be higher but is still consistent with (6.6). In Table 6.1 we have seen that when omitting small chains the shift exponent takes on larger values. It is therefore possible that if we had defined pseudo-critical points as the maxima of the twist order parameter's absolute slope, those points would indeed show the same shift as the peak locations of the correlation length. The zeros of the twist order parameter, however, show an error of order $1/L$ that significantly alters the shift behaviour of overly small chains.

6.2.2 Imaginary Time Correlation Length for Fixed Chain Length

We now want to change our perspective and keep the chain length L at a fixed value while observing the dependence on β . We will benefit from this as a lot more data points can be included in the finite-size scaling analysis. The longest chain simulated for model **B** is of length $L = 512$ which is still larger than $\beta = 100$. It is pointed out in Section 5.5.2 that it should be possible to apply exactly same the fit functions in a region where the linear dependence on β is reproduced. Provided the dynamic critical exponent z is unity, the shift exponent will be $1/\nu$. The dependence of the correlation length estimators on β at fixed chain length L is shown in Figs. 6.10 and 6.11. The aspect ratio now much better approximates the condition $L/\beta \approx \infty$ and linear dependence of the peak heights on β is reproduced for more data sets. A test fit ($L = 512, \beta = 6.67, \dots, 100$) to a “faked” linear function in β that is proportional to β^x gives a value of $x = 0.993(2)$ and $\chi_{\text{pdof}}^2 = 2.65$. Even though this result does not consistently prove linear dependence it is better than before, and we will take it as assuring enough to keep the data points of all temperatures for a fixed chain length of $L = 512$ in order to perform the

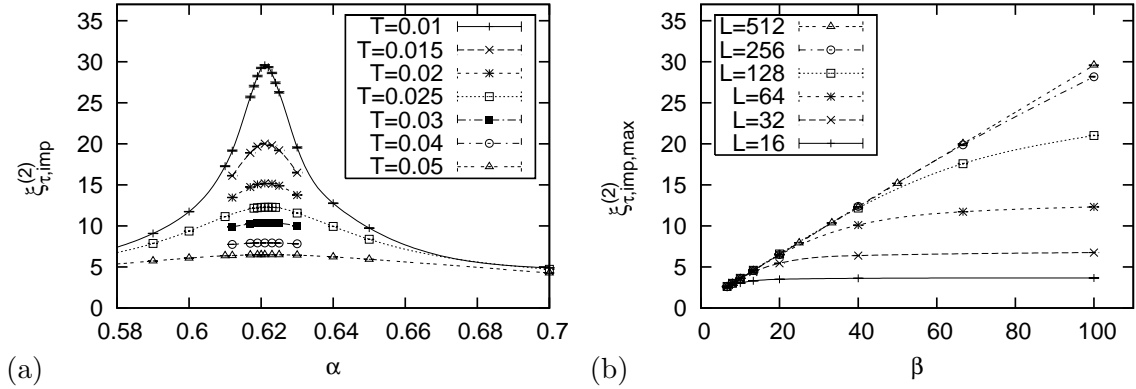


Figure 6.10: Improved second-moment estimator of the imaginary time correlation length ξ_τ at fixed chain length. *Lines* are simple interpolations to guide the eye. (a) Dependence on the coupling ratio α for various temperatures and $L = 512$. (b) Height of the maxima against inverse temperature β for $L = 16, \dots, 512$.

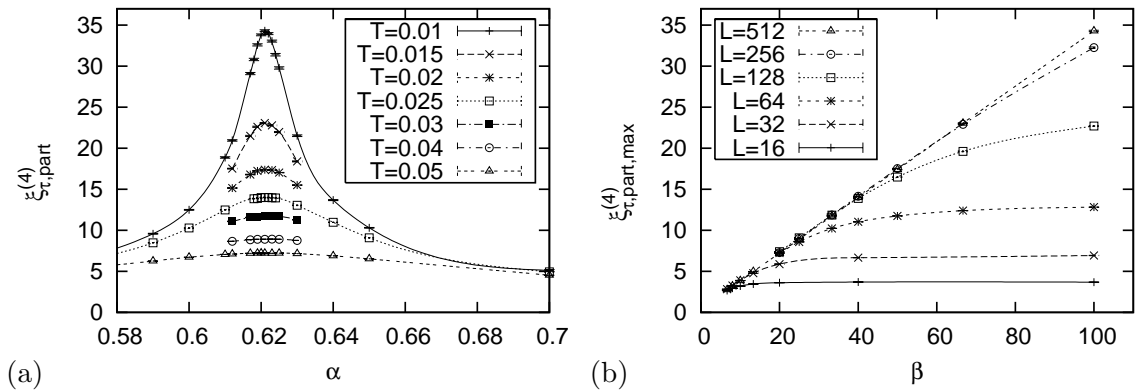


Figure 6.11: Same as Fig. 6.10, but for the partly improved fourth-moment estimator.

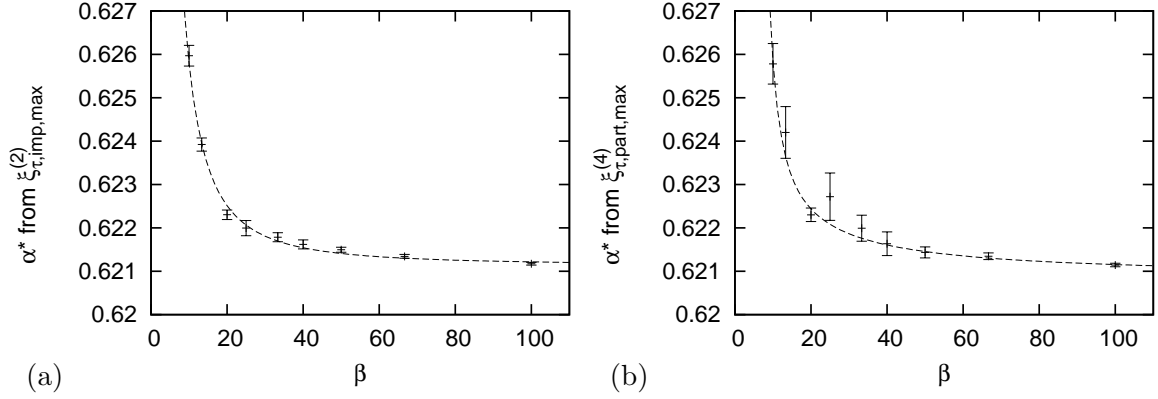


Figure 6.12: Peak locations of the imaginary time correlation length ξ_τ at fixed $L = 512$. *Lines* show fits to the finite-size scaling function (5.48). A qualitative change of the β -dependence can be observed at $\beta \approx 20$. (a) Improved second-moment estimator. (b) Partly improved fourth-moment estimator.

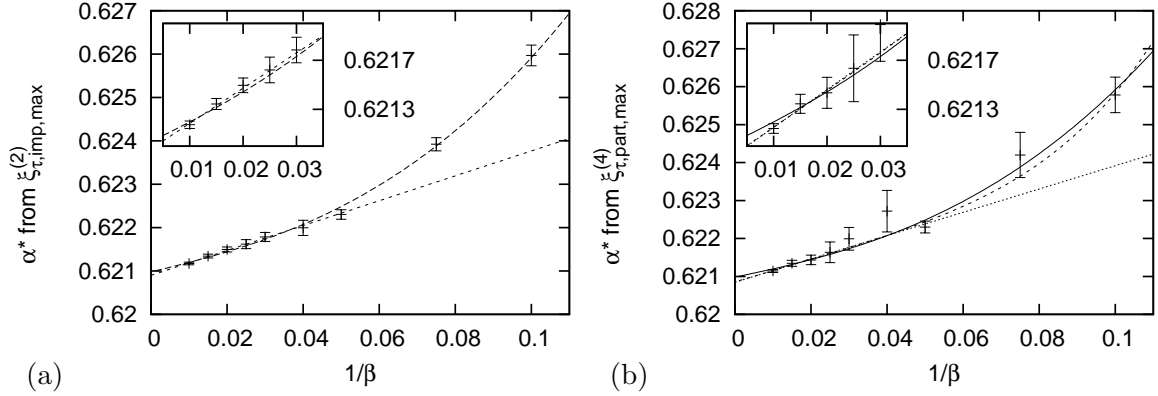


Figure 6.13: Same as Fig. 6.12, but plotted against the temperature $T = 1/\beta$. The change of the shift behaviour can now be seen more clearly even for the improved second-moment estimator in (a). The *solid line* in (b) is the non-linear finite-size scaling fit from (a).

analysis of the peak locations. The results of the finite-size scaling fits are shown in Fig. 6.12. Fitting to (5.48) – where now $l = \beta$ – gives

$$\alpha_c = 0.62117(4), \quad (6.11)$$

and

$$\theta = 1.92(8) \quad \longrightarrow \quad \nu = 0.52(3). \quad (6.12)$$

for the improved second-moment estimator and

$$\alpha_c = 0.62107(7), \quad (6.13)$$

and

$$\theta = 1.66(19) \quad \longrightarrow \quad \nu = 0.60(7). \quad (6.14)$$

for the partly improved fourth-moment estimator. These values of the shift exponent come consistently close to the ones determined from the twist order parameter in the preceding

section (when small chains are omitted). This indicates that the zeros of the twist order parameter possibly do asymptotically shift with the same exponent as the correlation length.

We note, however, that there seems to be a qualitative change of the shift behaviour occurring at $\beta \approx 20$. Plotting the peak locations of the correlation length estimators against the temperature (i.e. $1/\beta$) this becomes even more obvious. For the larger values of β (small T) the shift of the pseudo-critical points of the improved second-moment estimator seems to be linear in $1/\beta$ (see Fig. 6.13). This would imply the shift exponent θ and, correspondingly, the critical exponent ν to be unity. The method of determination of the peak heights and locations has been checked thoroughly in order to exclude systematic errors from this side. A possible interpretation on the one hand is that we observe a crossover effect that becomes apparent at $\beta \approx 20$ from effectively two to one dimensional classical behaviour, i.e. that the system begins to “feel” the finiteness of the spatial dimension at surprisingly high temperatures. On the other hand we need to be careful as the linearity in $1/\beta$ is only induced by the data point at $\beta = 20$. The non-linear behaviour, however, does not get strong support either. The two values of β that dominate the bend of the curve are very small compared to the chain length of $L = 512$.

6.2.3 Spatial Correlation Length

So far, we have only discussed the imaginary time correlation length ξ_τ . Analysing the spatial correlation length ξ we basically observe the same behaviour. If we keep the temperature fixed at the lowest value simulated (i.e. at the highest value of β) the spatial correlation length measured by the partly improved second-moment estimator will saturate (Fig. 6.14). The values it takes on are generally about twice as high as those of its temporal counterpart.

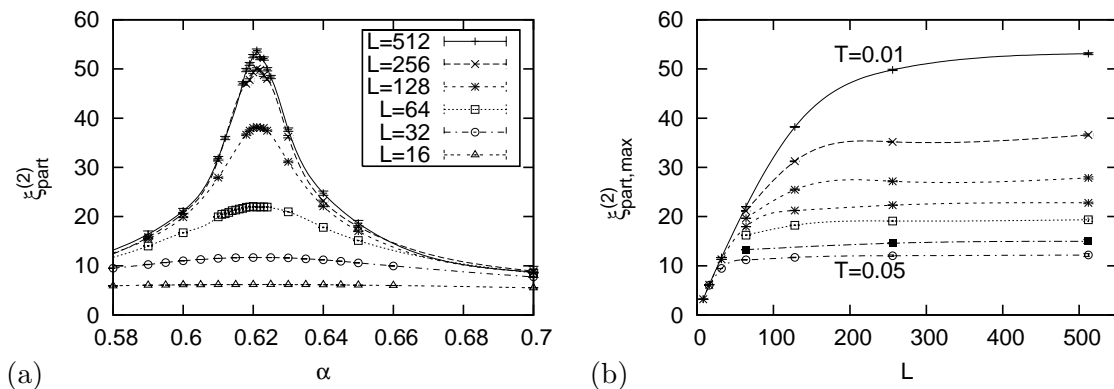


Figure 6.14: Partly improved second-moment estimator of the spatial correlation length ξ at fixed temperature. Lines are simple interpolations to guide the eye. (a) Dependence on the coupling ratio α for various chain lengths L at $T = 0.01$ ($\beta = 100$). (b) Height of the maxima against L for $T = 0.01, 0.015, 0.02, 0.025, 0.03, 0.04, 0.05$ ($\beta = 100, \dots, 20$).

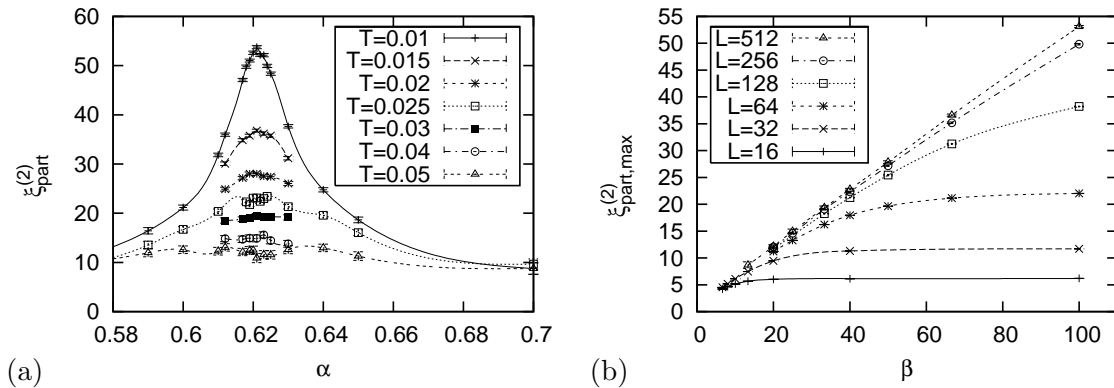


Figure 6.15: Partly improved second-moment estimator of the spatial correlation length ξ at fixed chain length. *Lines* are simple interpolations to guide the eye. (a) Dependence on the coupling ratio α for various temperatures and $L = 512$. (b) Height of the maxima against inverse temperature β for $L = 16, \dots, 512$.

Linear dependence on the chain length L is again – at most – reproduced up to values as high as $L = 64$. The numerical check of linearity – a fit proportional to L^x not considering the error estimates of the pseudo-critical points – produces $x = 0.900(5)$ with $\chi_{\text{pdof}}^2 = 0.0003$. The finite-size scaling analysis without correction terms gives

$$\alpha_c = 0.6217(1), \quad (6.15)$$

and

$$\theta = 2.9(4) \quad \longrightarrow \quad \nu = 0.34(5). \quad (6.16)$$

The shift exponent differs significantly from the values obtained so far. Changing the scaling perspective again we can keep the chain length fixed at $L = 512$ (see Fig. 6.15) to hope for better data sets of more points. Even though the linearity check is more promising than before with the exponent $x = 0.94(1)$ and χ_{pdof}^2 – thus showing that linear dependence on β is better reproduced – the locations of the critical points do not give a sufficiently smooth function to be fitted. As shown in Fig. 6.16b only the five highest values of β have been fed into (5.48) to give

$$\alpha_c = 0.6211(2), \quad (6.17)$$

and

$$\theta = 3.3(1.5) \quad \longrightarrow \quad \nu = 0.30(14). \quad (6.18)$$

The reason for this high uncertainty of peak locations at small β can be seen in Fig. 6.15a. Even though the error estimates are reasonably small the partly improved second-moment estimator of the spatial correlation length strongly varies in the vicinity of the peak. It is very likely that this roots back onto the use of the unimproved estimator $\chi_{\text{unimp}}(\pi + 2\pi/L, 0)$ in order to calculate the partly improved second-moment estimator $\xi_{\text{part}}^{(2)}$.

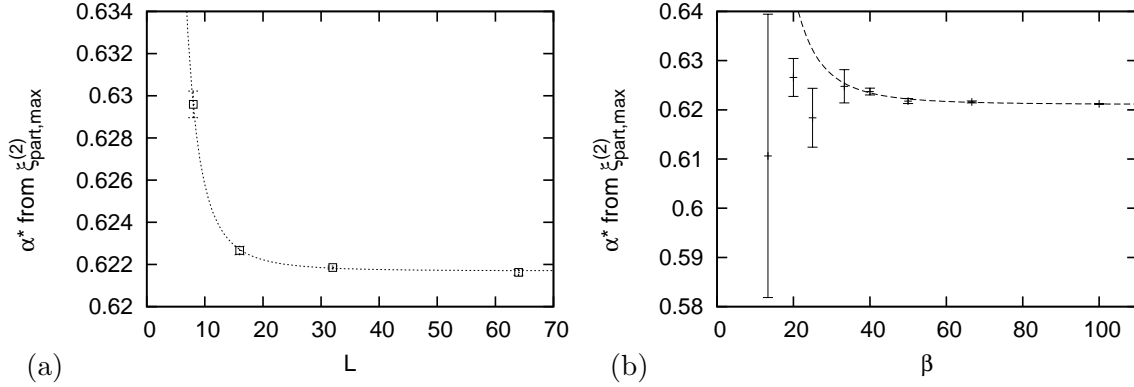


Figure 6.16: Peak locations of the partly improved second-moment estimator of the spatial correlation length. *Curves* show the corresponding finite-size scaling fits (5.48). (a) As a function of chain length at $T = 0.01$ ($\beta = 100$). (b) As a function of inverse temperature β for chain length $L = 512$.

6.2.4 Corrections to Scaling and Linearity Check

Results of all fit functions including the ones with correction terms are listed in Tables 6.4 and 6.5 for the imaginary time correlation length. Fits to the pure finite-size scaling relation (5.48) without correction terms produce lower estimates of the shift exponent if the chain length is kept fixed. The values thus obtained also agree better with the ones obtained from the twist order parameter when small chains are omitted. Including the term linear in $1/\beta$ and letting the shift exponent be a free fit parameter – fit function (5.52) – gives a consistently non-zero parameter a but a significantly higher shift exponent. Furthermore we note that the exponent estimates from the linear procedure show surprisingly low values. This indicates that we have indeed resolved two terms with different asymptotic behaviour. The onset of dominant linearity in $1/\beta$ for $\beta > 20$ might be the crossover from effectively two to one dimensional classical behaviour. The problem then is that we cannot take the shift exponent obtained from those fits and draw precise conclusions about the critical exponent ν . However, as the various values of the shift exponent differ widely anyway, precise conclusions concerning ν remain inconclusive so far.

Fit (5.56) takes the exponent estimate from (5.48) and does not output a significant correction term. Once the exponent is fixed at its value from (5.48), the term linear in $1/\beta$ or $1/L$ is not accepted. This, in turn, does not support the assumption of the onset of dimensional crossover but that instead the peak locations' shift is controlled by one single term with the exponent not being one.

All tests of linearity are listed in Tables 6.6 and 6.7. It can be seen that the results are much better if we keep the chain length constant. In this case the aspect ratio better approximates the condition $\beta/L \approx \infty$ and finite-size scaling fits according to the functions explained in Section 5.5.2 are more reliable to be applied.

Table 6.4: Finite-size scaling fit results of both the improved second-moment estimator $\xi_{\tau,\text{imp}}^{(2)}$ and the partly improved fourth-moment estimator $\xi_{\tau,\text{part}}^{(4)}$ of the imaginary time correlation length. The inverse temperature is kept fixed at $\beta = 100$. Four chain lengths included: $L = 8, \dots, 64$. The fit to (5.52) is a four parameter fit of four data points, consequently its χ_{pdof}^2 is zero by definition. Fits to (5.54) and (5.55) use the exponent estimated by the linear procedure explained in Section 5.5.2: $\theta^{(\text{lin})} = 2.34(5)$ for $\xi_{\tau,\text{imp}}^{(2)}$ and $\theta^{(\text{lin})} = 2.21(9)$ for $\xi_{\tau,\text{part}}^{(4)}$.

Obs.	Fit	α_c	a	b	θ	χ_{pdof}^2
$\xi_{\tau,\text{imp}}^{(2)}$	(5.48)	0.6216(2)	–	–6.7(1.1)	2.3(1)	0.60
	(5.52)	0.6212(7)	0.036(52)	–5.4(1.7)	2.2(2)	–
	(5.53)	0.6189(5)	0.295(29)	–2.6(2)	–	18.44
	(5.54)	0.6216(1)	–	–7.3(2)	–	0.43
	(5.55)	0.6216(3)	–0.003(14)	–7.2(4)	–	0.81
	(5.56)	0.6215(3)	0.004(14)	–6.8(4)	–	0.53
$\xi_{\tau,\text{part}}^{(4)}$	(5.48)	0.6216(3)	–	–5.3(4.1)	2.3(3)	0.19
	(5.52)	0.6206(28)	0.12(45)	–2.6(4.4)	1.8(1.2)	–
	(5.53)	0.6200(10)	0.20(9)	–2.0(5)	–	0.15
	(5.54)	0.6216(2)	–	–4.9(4)	–	0.10
	(5.55)	0.6214(7)	0.01(5)	–5.2(1.2)	–	0.15
	(5.56)	0.6215(7)	0.01(5)	–5.5(1.3)	–	0.18

Table 6.5: Same as Table 6.4 but with the chain length kept fixed at $L = 512$. Temperatures included in the fits: $T = 0.01, 0.015, 0.02, 0.025, 0.03, 0.04, 0.05, 0.75, 0.100, 0.125$ (i.e. $\beta = 8, \dots, 100$). $\theta^{(\text{lin})} = 1.48(24)$ for $\xi_{\tau,\text{imp}}^{(2)}$ and $\theta^{(\text{lin})} = 1.27(74)$ for $\xi_{\tau,\text{part}}^{(4)}$.

Obs.	Fit	α_c	a	b	θ	χ_{pdof}^2
$\xi_{\tau,\text{imp}}^{(2)}$	(5.48)	0.62117(4)	–	0.405(73)	1.92(8)	1.78
	(5.52)	0.62098(8)	0.021(6)	1.28(86)	2.66(38)	1.15
	(5.53)	0.62127(7)	–0.017(6)	0.29(3)	–	3.26
	(5.54)	0.62100(3)	–	0.147(4)	–	5.07
	(5.55)	0.62129(7)	–0.034(8)	0.25(3)	–	2.88
	(5.56)	0.62114(6)	0.003(4)	0.38(4)	–	1.72
$\xi_{\tau,\text{part}}^{(4)}$	(5.48)	0.62107(7)	–	0.21(10)	1.66(19)	0.92
	(5.52)	0.62088(12)	0.028(11)	3.2(11.9)	3.2(1.9)	0.78
	(5.53)	0.62107(12)	0.001(13)	0.19(6)	–	1.00
	(5.54)	0.62092(5)	–	0.079(6)	–	1.29
	(5.55)	0.62115(15)	–0.046(28)	0.17(6)	–	1.07
	(5.56)	0.62104(11)	0.003(12)	0.195(59)	–	0.91

Table 6.6: Check of linearity of the peaks of the correlation length estimators. The peak height at the pseudo-critical points in dependence of $l = L$ or $l = \beta$ are fitted to $f(l) = a + b * l^x$, with a , b and x the fit parameters. Chain lengths included for $l = L$: 8, 16, 32, 64. Temperatures included for $l = \beta$: 0.01, 0.015, 0.02, 0.025, 0.03, 0.04, 0.05, 0.75, 0.100, 0.125, 0.150 (i.e. $\beta = 6.67, \dots, 100$). Error estimates of the peak heights are being considered.

Observable	l	a	b	x	χ_{pdof}^2
$\xi_{\tau, \text{imp}}^{(2)}$	L	0.21(8)	0.28(3)	0.91(3)	183.4
	β	0.642(6)	0.299(2)	0.993(2)	2.6
$\xi_{\tau, \text{part}}^{(4)}$	L	-0.98(56)	0.52(11)	0.79(4)	33.5
	β	0.549(6)	0.326(2)	1.008(2)	0.5
$\xi_{\text{part}}^{(2)}$	L	-0.27(4)	0.54(2)	0.893(6)	12.0
	β	0.69(32)	0.69(4)	0.94(2)	0.1

Table 6.7: Same as Table 6.6, but with error estimates of the peak heights not being considered.

Observable	l	a	b	x	χ_{pdof}^2
$\xi_{\tau, \text{imp}}^{(2)}$	L	0.06(12)	0.32(3)	0.88(2)	0.00131
	β	0.635(10)	0.299(2)	0.993(1)	0.00008
$\xi_{\tau, \text{part}}^{(4)}$	L	-0.86(41)	0.51(8)	0.79(3)	0.01176
	β	0.50(2)	0.335(3)	1.002(2)	0.00026
$\xi_{\text{part}}^{(2)}$	L	-0.21(5)	0.53(1)	0.900(5)	0.00024
	β	0.89(22)	0.66(3)	0.95(1)	0.00082

6.3 Staggered Susceptibility

To complete the presentation of the observables of model **B** let us briefly look at the staggered susceptibility χ_s . This quantity is measured directly by one single improved estimator and therefore gives very accurate data points. Height and location of maxima could be determined with proper accuracy. From finite-size scaling theory we expect that the height of the maxima grows proportional to $L^{\gamma/\nu}$ and the locations shift with the same shift exponent as the correlation length.

In Fig. 6.17 we see again saturation of the observable for all temperatures. Keeping the temperature fixed the staggered susceptibility ceases to grow at some value of L . This confirms that there is no critical point at non-zero temperatures in the classical system which we mapped the quantum spin chain onto. As we wish to extract the exponent γ we cannot make an assumption on the L -dependence of χ_s in order to check how many data points can be included in the corresponding finite-size scaling fits. We must rely on the knowledge obtained so far from analysing the correlation lengths. If we – following the discussion of the preceding section – take the correlation to be approximately linear in L for the chain lengths $L = 8, \dots, 64$

we can measure the L -dependence of the staggered susceptibility's peak heights for $\beta = 100$. For these four data points we get

$$\frac{\gamma}{\nu} = 1.02(2), \quad (6.19)$$

when the very small error estimates of the heights are included. Inclusion of error estimates leads to a ridiculously high $\chi_{\text{pdof}}^2 = 327.6$. Not considering the error estimates gives

$$\frac{\gamma}{\nu} = 0.99(2), \quad (6.20)$$

with $\chi_{\text{pdof}}^2 = 0.05$. The height of the maxima of χ_s seems dominantly linear in L at $T = 0.01$ as long as we only consider chains with $L \leq 64$.

This result is confirmed if we look at the β -dependence of the peak heights at fixed chain length $L = 512$ (Fig. 6.18). Including all data points (i.e. $\beta = 6.67, \dots, 100$) and considering error estimates we get

$$\frac{\gamma}{\nu} = 1.050(3) \quad (6.21)$$

with $\chi_{\text{pdof}}^2 = 8.54$ which again is rather high. Neglecting the error estimates gives

$$\frac{\gamma}{\nu} = 1.055(2) \quad (6.22)$$

with $\chi_{\text{pdof}}^2 = 0.01$. This exponent ratio is very close to one but not consistently so anymore. Omitting the highest temperature (smallest β) gives the same exponents with even better values of χ_{pdof}^2 .

Thus, we observe linear dependence of the staggered susceptibility on L or β if the other is kept fixed as long as we keep the ratio L/β or β/L sufficiently large. Crossover effects that we observed in the preceding section are not reflected so far by the staggered susceptibility. It, however, turns out that the location of the peaks, in contrast to the height, seems more

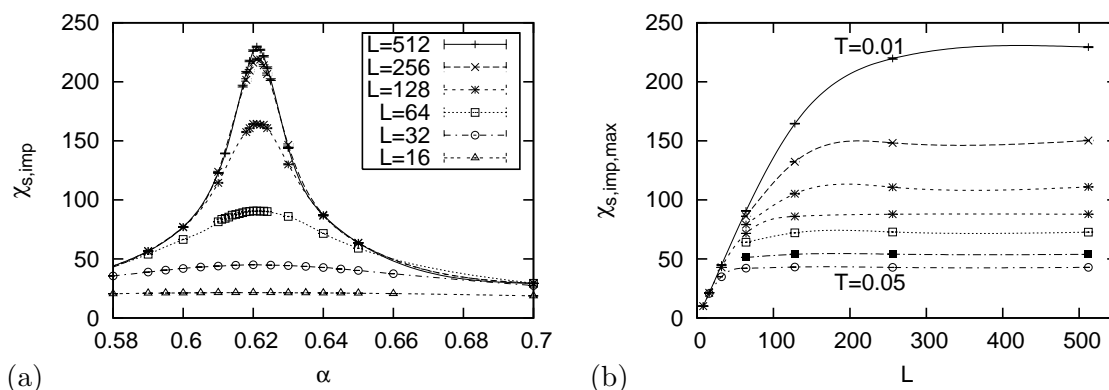


Figure 6.17: Improved estimator of the staggered susceptibility at fixed temperature. *Lines* are simple interpolations to guide the eye. (a) Dependence on the coupling ratio α for various chain lengths L at $T = 0.01$ ($\beta = 100$). (b) Peak heights as function of the chain length for temperatures $T = 0.01, 0.015, 0.02, 0.025, 0.03, 0.04, 0.05$ ($\beta = 20, \dots, 100$).

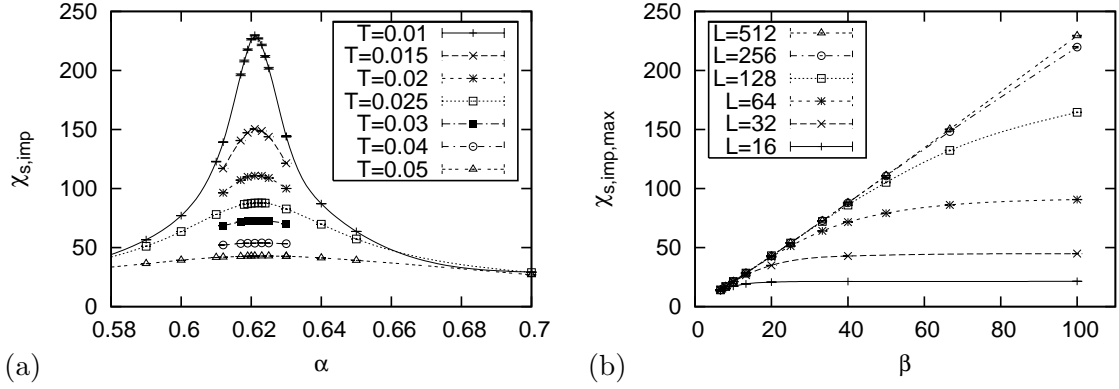


Figure 6.18: Improved estimator of the staggered susceptibility at fixed chain length. *Lines* are simple interpolations to guide the eye. (a) Dependence on the coupling ratio α for various temperature T and $L = 512$. (b) Peak heights as function of the inverse temperature β for various fixed chain lengths L .

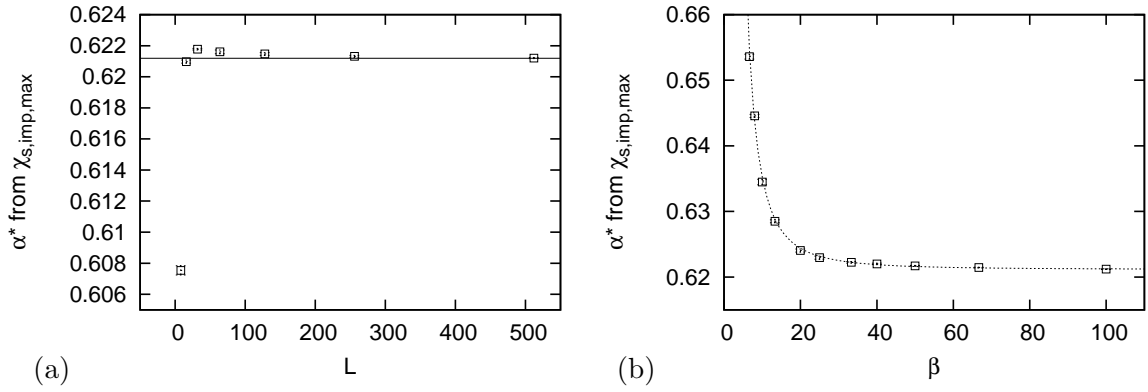


Figure 6.19: Peak locations of the staggered susceptibility. *Curves* show the corresponding finite-size scaling fits (5.48) (a) As a function of chain length at $T = 0.01$ ($\beta = 100$). *The line* indicates the value of α_c from the finite-size scaling fit with constant chain length. (b) As a function of inverse temperature β for chain length $L = 512$.

sensitive to crossover effects. We see in Fig. 6.19a that the peak locations are not monotonic with L for $\beta = 100$. Already at $L = 64$ which is still smaller than $\beta = 100$ the shift behaviour is significantly altered. This is exactly what could be observed also for the correlation lengths at higher temperatures. While in the case of the correlation length it was not possible to exclude systematic errors in the determination of the peaks due to larger error estimates, the staggered susceptibility allows for precise determination of the peaks and their location. Consequently, we must accept the non-monotonic behaviour and interpret it as the physical result of the finite chains at the given inverse temperature of $\beta = 100$. The corresponding finite-size scaling fits are difficult and in fact do not work well in that case. The tables listed in the appendix show the resulting parameters of those fits of the correlation length. No fits of this kind have been undertaken for the staggered susceptibility.

Table 6.8: Finite-size scaling fit results of the staggered susceptibility χ_s . The chain length is kept fixed at $L = 512$. Temperatures included in the fits: $T = 0.01, 0.015, 0.02, 0.025, 0.03, 0.04, 0.05, 0.75, 0.1, 0.125, 0.15$ (i.e. $\beta = 6.67, \dots, 100$). Fits to (5.54) and (5.55) use the exponent estimated by the linear procedure explained in Section 5.5.2: $\theta^{(lin)} = 1.81(22)$.

Fit	α_c	a	b	θ	χ_{pdof}^2
(5.48)	0.62115(4)	–	1.85(13)	2.12(4)	3.84
(5.52)	0.62106(11)	0.009(12)	2.06(33)	2.20(11)	4.29
(5.53)	0.62191(8)	–0.109(7)	1.10(3)	–	14.79
(5.54)	0.62090(3)	–	0.98(1)	–	15.05
(5.55)	0.62146(7)	–0.047(5)	1.22(3)	–	5.87
(5.56)	0.62113(6)	0.001(4)	1.84(4)	–	3.83

The shift of the peak locations remains monotonic if we fix the chain length at its largest value of $L = 512$ (Fig. 6.19). The results of applying all finite-size scaling fits are listed in Table 6.8. The overall very high values of χ_{pdof}^2 are due to the small error estimates of the peak locations.

6.4 Analysis With Constant Aspect Ratio

Originally in this analysis, we were also interested in the low-temperature properties of the three Heisenberg spin chains. Various values of chain length and temperature were chosen to yield series of data points of different chain length at a given, constant and low temperature. We have seen that at fixed temperature scaling breaks down, i.e. the correlation length ceases to grow linearly with L , for chain lengths that become sufficiently long. From a rough estimate based on the slope of the twist order parameter we guessed that this breakdown occurs for chain lengths $L \approx 4\beta$. The linearity of the correlation length has been used to approximately determine how many data points can be reliably fed into the finite-size scaling fits from Section 5.5.2. Unfortunately, we had to realise that at most four data points survived.

In order to keep more data points we tried to change our perspective. Interpreting the inverse temperature as length scale we performed the finite-size scaling analysis with β instead of L , which this time is kept fixed at $L = 512$. Indeed, almost all data points could be used for the analysis.

The usual way of finite-size scaling is to vary L and β simultaneously and keep the aspect ratio $R = L/\beta$ constant. This corresponds to simultaneously taking the thermodynamic limit $L \rightarrow \infty$ as well as the temperature limit $T \rightarrow 0$ ($\beta \rightarrow \infty$). This way finite-size scaling gives information about the zero temperature quantum phase transition.

However, due to the specific of choice chain lengths and temperatures we have at most

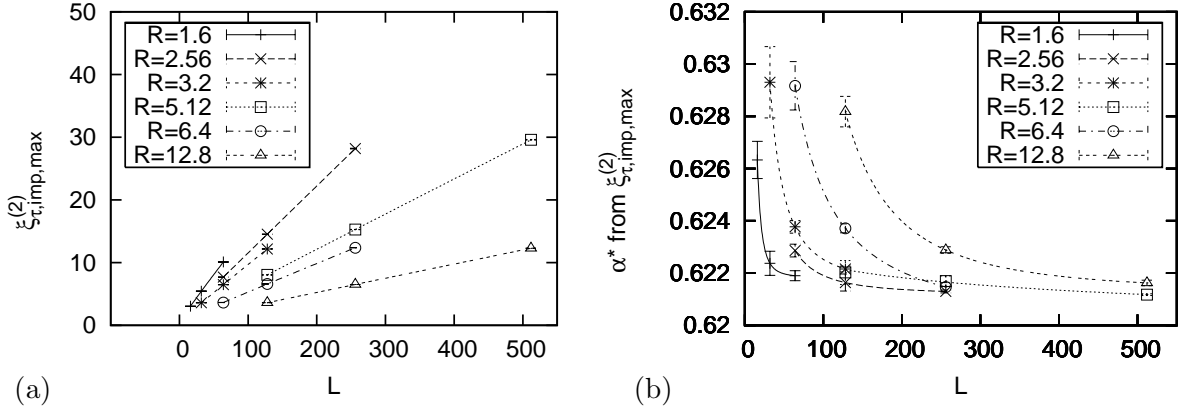


Figure 6.20: Maxima of the second-moment estimator of the imaginary time correlation length as function of the chain length L for six different aspect ratios $R = L/\beta$. (a) Height of the maxima. (b) Location of the maxima. *Curves* show finite-size scaling fits.

three data points that can be fed into the uncorrected finite-size scaling fit (5.48). This results in a three parameter fit of three data points. In Fig. 6.20a the height of the maxima of the imaginary time correlation length for six different constant aspect ratios $R = L/\beta$ is shown. We note that for each value of R the correlation length measured by the improved second-moment estimator $\xi_{\tau, \text{imp}}^{(2)}$ does grow linearly with the system size, as expected. The corresponding shift of the location of the maxima is shown in Fig. 6.20b and it can be seen that the shift is qualitatively and quantitatively different for each different value of the aspect ratio R . Furthermore, due to the lack of data points the non-linear finite-size scaling fits are unstable and error estimates are unreliable. The estimates for the shift exponent θ from analysing the location of the maxima of the temporal correlation length are listed in the upper part of Table 6.9. In contrast to the maxima determined from the correlation length, the zeros determined from the twist order parameter do qualitatively show the same shift behaviour for each value of R . Figure 6.21 shows that for each aspect ratio the locations of the pseudo-critical almost fall on one line (two values of R are omitted for clarity). However, we still do not have more than three data points to fit and therefore cannot precisely determine an exponent or give

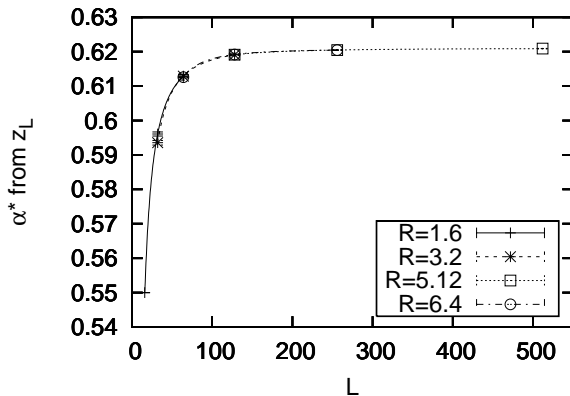


Figure 6.21: Location of the pseudo-critical points determined from the twist order parameter z_L as function of the chain length L for constant aspect ratio $R = L/\beta$. In contrast to the critical points determined from the second moment estimator of the correlation length these critical points almost fall on one line regardless of the value of the aspect ratio R .

Table 6.9: Estimates of the shift exponent θ determined from finite-size scaling fits without corrections – (5.48) – of the pseudo-critical points of the second-moment estimator of the correlation length $\xi_{\tau,\text{imp}}^{(2)}$ and the twist order parameter z_L . The aspect ratio $R = L/\beta$ is kept fixed. $L \dots$ chain lengths included in the fit.

Observable	R	L	θ
$\xi_{\tau,\text{imp}}^{(2)}$	1.6	16, 32, 64	3.05
	2.56	64, 128, 256	1.85
	3.2	32, 64, 128	1.78
	5.12	128, 256, 512	0.01
	6.4	64, 128, 256	1.28
	12.8	128, 256, 512	2.07
z_L	1.6	16, 32, 64	1.46
	2.56	64, 128, 256	2.43
	3.2	32, 64, 128	1.65
	5.12	128, 256, 512	1.73
	6.4	64, 128, 256	2.35
	12.8	128, 256, 512	7.31

reliable error estimates which is why they are not reported here. The estimates for the shift exponent θ determined from the twist order parameter are listed in the lower part of Table 6.9.

All fits started with the same initial value of the shift exponent $\theta_0 = 1$. Meaningless values in Table 6.9 such $\theta = 0.01$ and $\theta = 7.31$ are clearly due to the lack of data points. For further analysis, however, it should be worthwhile to securely establish the zero temperature critical value of the coupling ratio α and especially precisely determine the critical exponent ν (i.e. the inverse shift exponent θ) by performing finite-size scaling analysis with constant aspect ratio $R = L/\beta$.

Chapter 7

Results of Models A and C

For models **A** and **C** data is available for $L = 16, 32, 64, 128$ and 256 . We will see that this is still sufficient to produce some estimates of critical coupling ratios and exponents. Results are qualitatively the same as for model **B** and merely differ in the numeric output. Model **C**, however, shows two transitions as we expected from the VBS picture in Section 3.4.3. Furthermore, it exhibits the largest values of correlation lengths and susceptibilities and is most sensitive to finite-size effects of all three models considered.

7.1 Twist Order Parameter

Let us start with the twist order parameter which is likely to give the most accurate estimate of the critical coupling ratios. Its α -dependence at $T = 0.01$ ($\beta = 100$) and the corresponding finite-size scaling fits are shown in Fig. 7.1 for model **A** and Figs. 7.2 and 7.3 for model **C**. No temperature induced plateaus could be resolved and therefore – following the discussion of model **B** – we assume that the detected zero transitions approximate the ground state value with sufficient accuracy for all chain lengths.

The inclusion of all available chain lengths in the finite-size scaling analysis of the pseudo-critical points using (5.48) gives for the critical coupling ratio of model **A**

$$\alpha_c = 0.7624(3), \quad (7.1)$$

and the shift exponent

$$\theta = 1.72(11) \quad \longrightarrow \quad \nu = 0.58(4), \quad (7.2)$$

with $\chi_{\text{pdof}}^2 = 0.02$. The analysis of the first (left) transition of model **C** yields

$$\alpha_c = 0.4836(5), \quad (7.3)$$

and

$$\theta = 1.32(5) \quad \longrightarrow \quad \nu = 0.76(3), \quad (7.4)$$

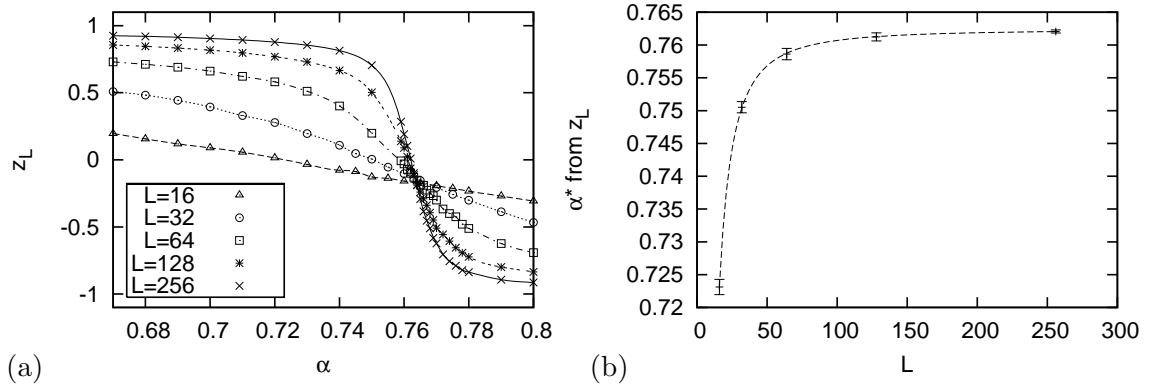


Figure 7.1: Twist order parameter z_L of model **A**. (a) Dependence on the coupling ratio α for various chain lengths L and temperature $T = 0.01$ ($\beta = 100$). Lines are simple interpolations to guide the eye. (b) Pseudo-critical points α^* . The curve is the finite-size scaling fit (5.48) without corrections.

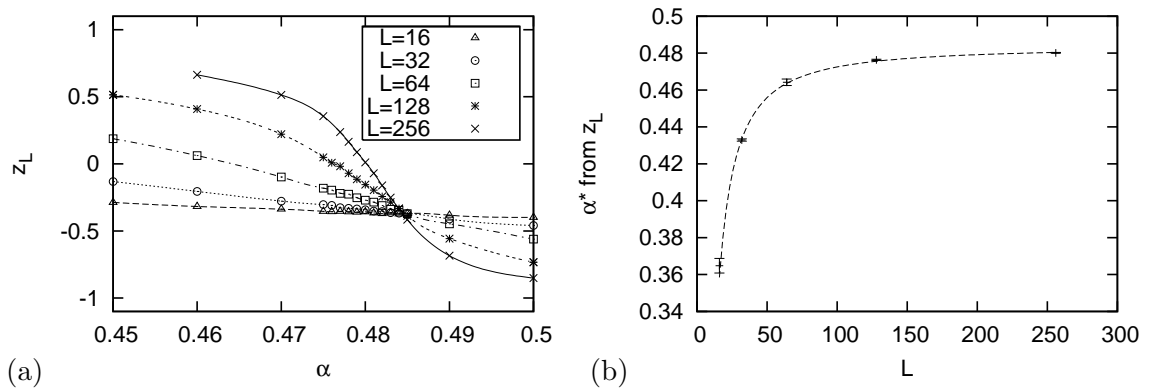


Figure 7.2: Same as Fig. 7.1, but for model **C** – left transition.

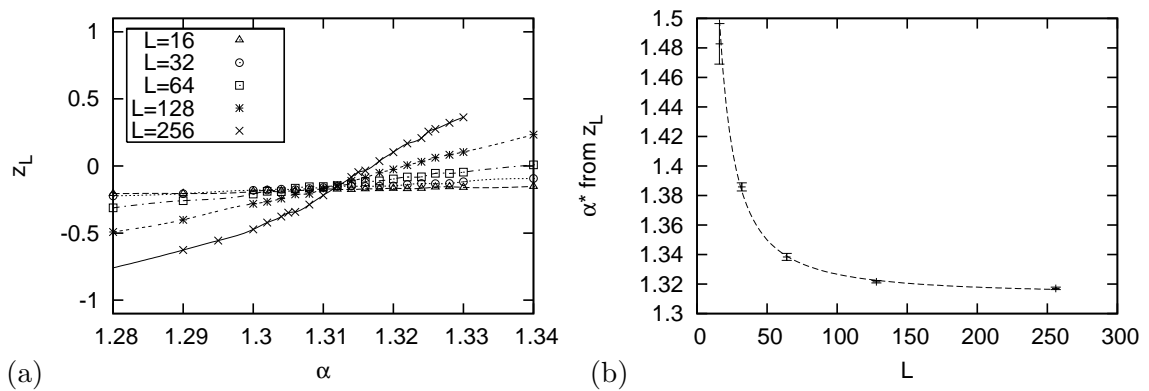


Figure 7.3: Same as Fig. 7.1, but for model **C** – right transition.

Table 7.1: Results of fitting the pseudo-critical points of the twist order parameter to the finite-size scaling relation without corrections (5.48) at fixed temperature $T = 0.01$. $L \dots$ chain lengths included in the fit, $\alpha_c \dots$ fit parameter – critical coupling ratio, $b \dots$ fit parameter, $\theta \dots$ fit parameter – shift exponent, $\chi_{\text{pdof}}^2 \dots$ chi-squared per degree of freedom; $\theta^{(lin)} \dots$ shift exponent from linear fit (see Section 5.5.2).

Model	L	α_c	b	θ	χ_{pdof}^2
A	8–256	0.7624(3)	–4.5(6)	1.71(5)	0.02
	16–256	0.7624(3)	– 4.5(1.5)	1.72(10)	0.02
	32–256	0.7625(5)	–3.6(4.9)	1.65(39)	0.00
	8–128	0.7624(7)	–4.5(7)	1.72(6)	0.02
	16–128	0.7623(9)	–4.7(2.0)	1.73(16)	0.02
C	16–256	0.4836(5)	–4.9(8)	1.32(5)	4.46
	32–256	0.4823(6)	–9.5(2.8)	1.52(9)	2.71
	16–128	0.4866(14)	–3.3(7)	1.19(7)	0.41
	16–256	1.3126(14)	9.4(2.9)	1.41(10)	2.38
	32–256	1.3146(15)	21.6(12.0)	1.65(17)	0.34
	16–128	1.3266(14)	5.6(2.4)	1.24(14)	1.04

with $\chi_{\text{pdof}}^2 = 4.46$. For the second (right) transition of model **C** we obtain

$$\alpha_c = 1.3126(14), \quad (7.5)$$

and

$$\theta = 1.41(10) \quad \longrightarrow \quad \nu = 0.71(6), \quad (7.6)$$

with $\chi_{\text{pdof}}^2 = 2.38$.

If we now investigate, as for model **B**, what happens when omitting either the shortest or the longest chain, we detect no significant change in the parameters for model **A**, at least within the error estimates that become larger. Analogously testing the finite-size scaling fits of model **C** by omitting either the shortest or longest chain results in the same qualitative changes as for model **B**, i.e. that the shift exponent changes to smaller values if we fit the four data points of $L = 16, \dots, 128$ and tends to become larger if we fit the four data points of $L = 32, \dots, 256$. Numbers that underline our discussion are listed in Table 7.1. We note that even though the shift exponents of model **C**'s two transitions seem to differ they are consistently the same at least within error estimates. It is further possible that the shift exponents of all three models are very close to each other if not the same when only chains of sufficiently large length are considered.

7.2 Correlation Lengths and Susceptibility

We will complete the presentation of results by quickly looking at the improved second-moment estimator of the imaginary time correlation length and the staggered susceptibility of models **A** and **C**. We have learned in the discussion of model **B** that performing our finite-size scaling analysis along the spatial direction by keeping the temperature at a fixed value leads to severe problems that at most permit to use four data points in the analysis. A “brute-force” analysis was carried out for various estimators of the correlation length at different temperatures. The corresponding fits to all trial fit functions mostly behave rather poorly and are listed in the tables of Appendix A. Those numbers witness the breakdown of scaling, i.e. that no true critical point could be detected in the non-zero temperature range under consideration. At non-zero temperature we do not detect divergencies of the correlation lengths or the susceptibilities in the classical system which the quantum spin chain is mapped onto. As $L = 8$ is not included for models **A** and **C** – no exact results have been calculated for either of the two diverging observables – we are left with just three data points where one (for $L = 64$) is highly insecure to be used. This is why we will only look at the results for the modified finite-size scaling analysis where the chain length is kept fixed at its presently largest value $L = 256$.

The results of model **A** are presented in Figs. 7.4 and 7.5. Even for the largest value of β the susceptibility depends almost linearly on β while for the imaginary time correlation length a small deviation can already be seen. The curves that are shown in Fig. 7.5b show the finite-size scaling fits without corrections fitted to all data points but the one of $\beta = 100$. Still this data point lies well within the range of the fit. Thus, by assuming that the finite-size scaling assumption holds within the range of $6.67 \leq \beta \leq 40$ the imaginary time correlation length yields

$$\alpha_c = 0.7619(3), \quad (7.7)$$

and

$$\theta = 1.22(10) \quad \longrightarrow \quad \nu = 0.82(7), \quad (7.8)$$

with $\chi_{\text{pdof}}^2 = 1.49$, while from the susceptibility of model **A** we obtain

$$\alpha_c = 0.7625(3), \quad (7.9)$$

and

$$\theta = 1.79(7) \quad \longrightarrow \quad \nu = 0.57(7), \quad (7.10)$$

with $\chi_{\text{pdof}}^2 = 0.42$. The two estimates of the shift exponent θ differ significantly which makes it impossible to give a definite value of ν . However, the exponent obtained from the staggered susceptibility is perfectly consistent with the values obtained from the twist order parameter (see Table 7.1).

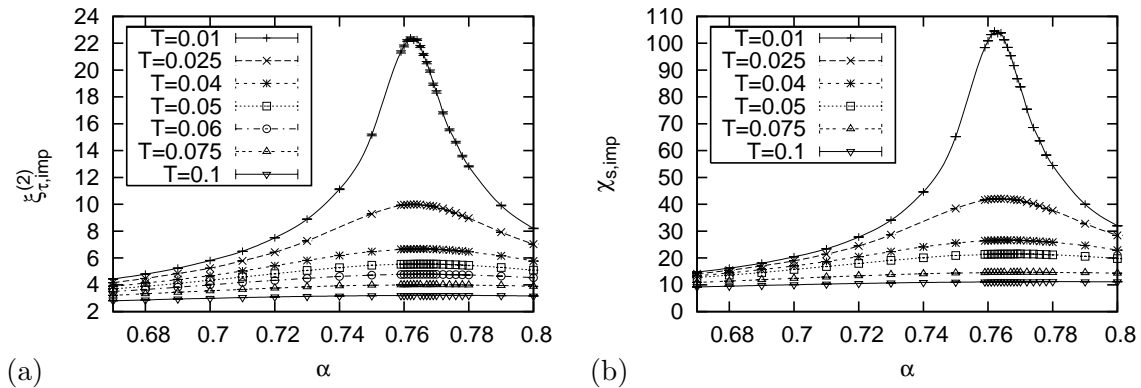


Figure 7.4: Improved estimators of the imaginary time correlation length (a) and the staggered susceptibility (b) of model **A** for various temperatures. The chain length is $L = 256$.

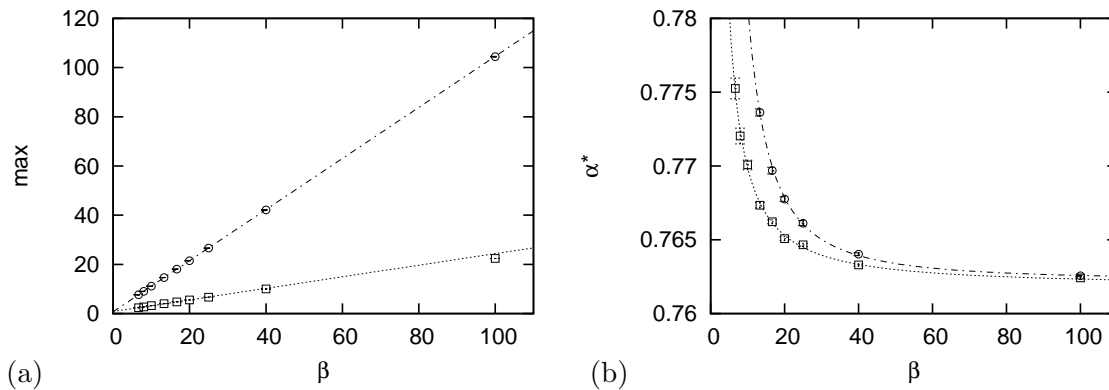


Figure 7.5: Pseudo-critical points of model **A** determined from the imaginary time correlation length (*boxes*) and the staggered susceptibility (*circles*) for $L = 256$. (a) Height of the maxima that define the pseudo-critical points against the inverse temperature β . *Straight lines* are linear fits of all data points shown, error estimates are considered in the fit. In contrast to the correlation length, the maximum of the susceptibility still grows linearly for the largest value of β . (b) Locations of the pseudo-critical points with the corresponding finite-size scaling fits (5.48) without corrections (*curves*).

In Figs. 7.6–7.9 the results of model **C** are shown. In Fig. 7.9 the linear dependence in β of both the imaginary time correlation length and the susceptibility clearly is not reproduced anymore at large values of the inverse temperature. In this case it is obvious that including the data points of $\beta = 100$ in the finite-size scaling fits of the location of the pseudo-critical points will give misleading results. Omitting that value the fit without corrections gives

$$\alpha_c = 0.4819(2), \quad (7.11)$$

and

$$\theta = 2.71(14) \quad \longrightarrow \quad \nu = 0.37(2), \quad (7.12)$$

with $\chi_{\text{pdof}}^2 = 4.74$ for the imaginary time correlation length of the left transition of model **C**.

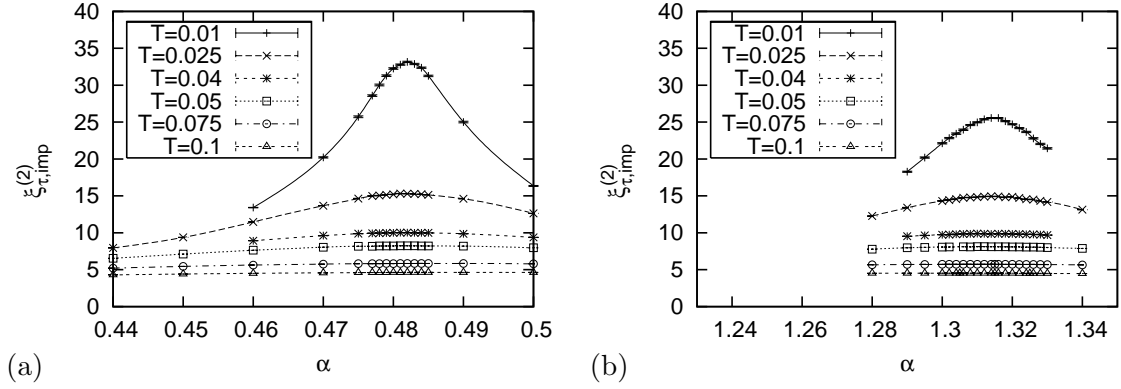


Figure 7.6: Improved second-moment estimator of the imaginary time correlation length of model **C** for various temperatures and the chain length kept fixed at $L = 256$. As was expected two peaks develop. (a) Left transition. (b) Right transition.

The corresponding fit of the right transition of model **C** gives

$$\alpha_c = 1.315(3), \quad (7.13)$$

and

$$\theta = 2.70(25) \quad \longrightarrow \quad \nu = 0.37(4), \quad (7.14)$$

with $\chi_{\text{pdof}}^2 = 1.20$. From the staggered susceptibility we get

$$\alpha_c = 0.4823(2), \quad (7.15)$$

and

$$\theta = 2.45(6) \quad \longrightarrow \quad \nu = 0.41(1), \quad (7.16)$$

with $\chi_{\text{pdof}}^2 = 3.38$ for the left transition and

$$\alpha_c = 1.3147(5), \quad (7.17)$$

and

$$\theta = 1.93(20) \quad \longrightarrow \quad \nu = 0.51(6), \quad (7.18)$$

with $\chi_{\text{pdof}}^2 = 1.08$ for the right transition.

We see that the analysis of the pseudo-critical points of the correlation length gives the same estimates of the shift exponent for both transitions whereas the data of the susceptibility yield different values. However, all values but the last one are drastically different from the ones obtained from the twist order parameter (see Table 7.1).

After having presented the most important results we will discuss the situation in the following and final chapter and try to give some reasons for the problems.

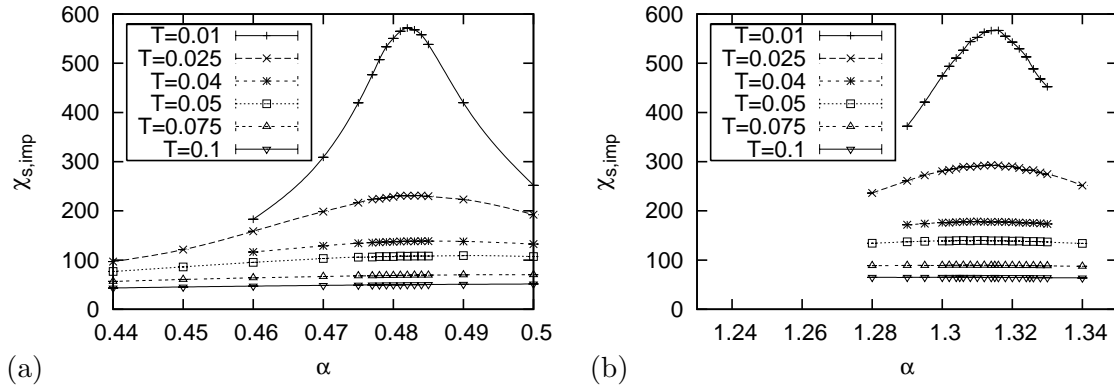


Figure 7.7: Staggered susceptibility of model C for various temperatures and the chain length kept fixed at $L = 256$. (a) Left transition. (b) Right transition.

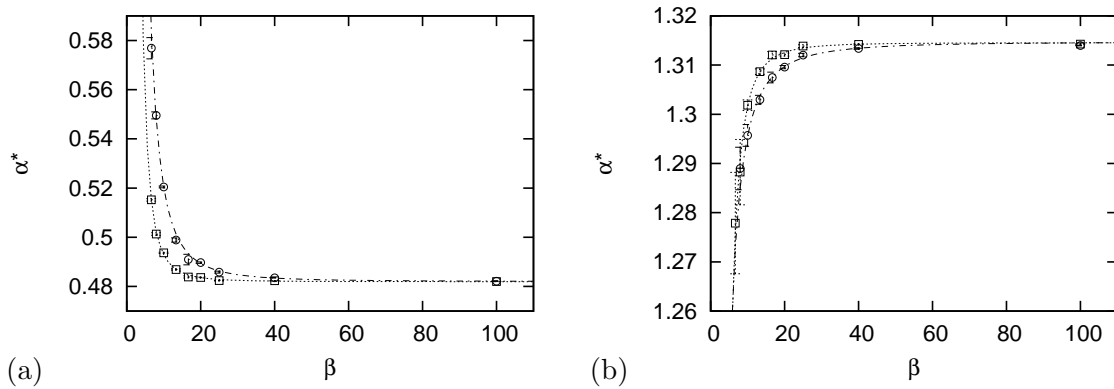


Figure 7.8: Location of pseudo-critical points α^* as function of the inverse temperature β (for $L = 256$). Circles show the points determined from the imaginary time correlation length, boxes those from the susceptibility. Curves show the corresponding finite-size scaling fits (5.48) without corrections. (a) Left transition. (b) Right transition.

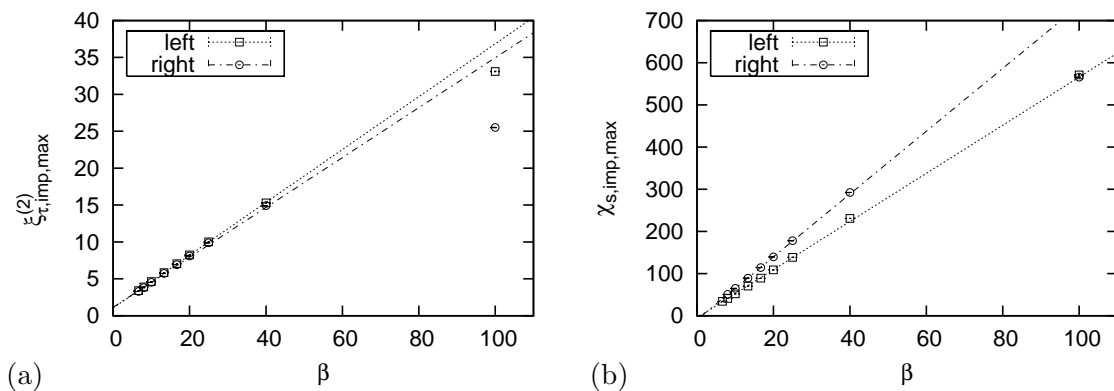


Figure 7.9: Maximum peak height of the imaginary time correlation length (a) and the staggered susceptibility (b) of model C against the inverse temperature β for $L = 256$. Data points of the susceptibility for $\beta = 100$ fall on top of each other. Lines show linear fits of all data points with error estimates of the peak height being considered.

Chapter 8

Discussion

8.1 Conclusions

The detailed analysis of model **B** has shown that the twist order parameter z_L presented in Section 3.5.1 indeed serves as a good order parameter to localise quantum critical coupling ratios α_c of mixed spin chains. As was expected one transition has been detected for models **A** and **B** and two for model **C**. The estimates obtained for the critical coupling ratio are especially accurate for model **B** where a chain length of $L = 512$ was included in the analysis. The shift exponent of the pseudo-critical points determined from zero points of $z_L(\alpha)$ is significantly altered if short chains of models **B** and **C** are included in the fits. In model **A**, which involves the smallest spins, this error is least apparent. It is assumed that this is due to a systematic error of order $1/L$ present in (3.41). Thus, in analysing the shift behaviour one needs to be careful and possibly only take longer chains into account in order to extract a reliable value of the exponent. By doing so it was found that the shift of all three models is controlled by exponents the values of which are very close to each other.

The detailed analysis of model **B** showed the temperature induced building of a plateau-like shape of $z_L(\alpha)$. By measuring a thermal average of the twist order parameter the corresponding properties of low-lying excited states are involved. This offers a possibility to classify “phases” in terms of the twist order parameter even at non-zero temperatures if the extent of the plateau remains finite in the thermodynamic limit. It can yet not be told if this really happens. The conjectured scenario is schematically depicted in Fig. 8.1. It was shown that this formation of a plateau significantly changes the location of zero points which is why it is, of course, not possible to do finite-size scaling analysis in order to extract exponents of the quantum critical point if the temperatures were too high.

The results of the diverging quantities – spatial and temporal correlation length and staggered susceptibility – showed beyond doubt that within the temperature range measured no criticality, i.e. divergence, could be detected. Thus, the classical systems which the quantum

spin chains are mapped onto do not show critical points at non-zero temperatures. For a classical system with finite extent in the imaginary time direction, the idea of a line of critical points with continuously varying exponents is not supported by the data. The saturation of the correlation lengths and the susceptibility fits the same picture. By analysing the linearity of the correlation length in dependence of L at fixed temperature and of β for fixed chain length we could approximately locate the region where the finiteness of the fixed dimension becomes apparent and thus determines the system's behaviour.

The finite-size scaling analysis, carried out for fixed non-zero values of temperature, must therefore be interpreted with special caution. From the twist order parameter we get shift exponents that decrease with increasing temperature. However, the saturation of actually diverging quantities leaves no other choice than to interpret the phenomena observed as crossovers. The dimensional crossover is from two- to one-dimensional classical behaviour. With growing chain lengths the pseudo-critical points at first follow the shift enforced by the quantum critical point's exponent (i.e. two-dimensional classical). With the chain length becoming comparable to the imaginary time length, however, the shift is modified. Even if correction terms made up for the qualitative change of the shift – which is not the case – the asymptotic values of the coupling ratio could not be interpreted as critical values at non-zero temperature, due to the lack of criticality in the correlation lengths and staggered susceptibility. In order to resolve the influence of the quantum critical point's exponent ν (i.e. at $T = 0$) at low non-zero temperature, its zero temperature value needs to be undoubtedly determined and known before.

The use of improved estimators proved vital for the calculation of the correlation lengths in order to avoid inappropriately large sample sizes. The second- and fourth-moment estimators are very sensitive to the errors of the input quantities. For this reason only the improved second-moment estimator was used in the analysis of models **A** and **C**.

The chosen way of analysis of the peak locations of the diverging quantities proved difficult. In order to include as many data points as possible to give stable fits, we applied the

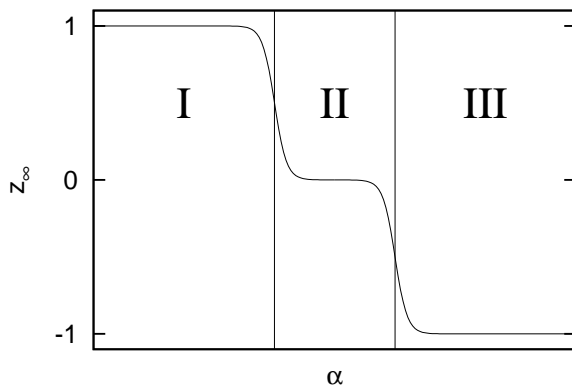


Figure 8.1: Schematic picture of the conjectured twist order parameter dependence on α at low non-zero temperatures in the thermodynamic limit ($L \rightarrow \infty$) that would apply to models **A** and **B**. It has to be further investigated if region I remains finite and if at the “transitions” between the different regions the slope becomes infinite or not. Additionally we do not yet know if the slope is zero in region II within a finite interval of α of non-zero measure.

condition that the aspect ratio L/β is approximately either zero or infinite. Both conditions are only insufficiently fulfilled by most of the values of chain length and inverse temperature simulated. Thus, the crossover effects from two to one dimensional behaviour observed could not be unambiguously resolved within the methods applied. This means that the shift of pseudo-critical points is first determined by the exponents of the zero-temperature (i.e. two dimensional) system but finally, with the aspect ratio coming closer to one, by the “exponents” of the system at non-zero temperature. As we concluded before that no criticality was detected we cannot define critical exponents of the system at non-zero temperature. Model **B** showed a significant linear dependence of the location of pseudo-critical points for large β when the chain length is kept fixed. This would imply a linear shift in the region where β is comparable to L . This hypothesis, however, was not investigated further, and due to the lack of appropriate data sets no analysis of that kind was done for models **A** and **C**.

For comparison, selected estimates of the critical coupling ratios from fitting to (5.48) of the models and observables under consideration are listed in Table 8.1, as well as the corresponding estimates of the shift exponents. Those values do not represent the best or most accurate estimates but those the author considers to be the most reliable ones within the context of discussion. The twist order parameter values of model **B** result from fitting the pseudo-critical points of chain lengths $L = 32, \dots, 512$ while those for the other two models result from fits including chain lengths $L = 32, \dots, 256$. The estimates for the diverging quantities result from the modified finite-size scaling analysis with chain length kept fixed at $L = 512$ for model **B** and at $L = 256$ for models **A** and **C**. Inverse temperatures included in the fits are $\beta = 6.67, \dots, 100$ and $\beta = 6.67, \dots, 40$, respectively.

We note that in the analysis of the staggered susceptibility of all three models no other than linear dependence on L or β with the other kept fixed has been measured, which is relevant for the critical exponent γ of the susceptibility. Within the accuracy of the analysis this implies that the critical exponents of the correlation length and the one of the susceptibility take on approximately the same value, i.e. $\nu \approx \gamma$.

Leaving all the above discussion aside large logarithmic corrections from fits to (5.53) can be observed for the twist order parameter of all three models (see Tables A.3, A.6, A.9 and A.10) – the origin of which remains yet unclear to the author – while the corresponding terms are significantly smaller for the imaginary time correlation length. This logarithmic term in (5.53) does not compete with a term that has a free exponent, and we cannot directly contrast it to the parameter values obtained from the fit without corrections, (5.48).

Finally, a few remarks on the attempts to identify correction terms with the trial fit functions presented in Section 5.5.2 are needed. Results are tabulated in Appendix A. One major problem lies in the nature of non-linear fits that tend to be unstable with highly correlated parameters. Even though the asymptotic value of the coupling ratio, i.e. α_c , is relatively

Table 8.1: Comparison of the critical coupling ratios α_c and the shift exponents θ (error estimates are the results of the fitting procedure) of all three models. Values from finite-size scaling analysis of the location of pseudo-critical points of the twist order parameter z_L , the improved second-moment estimator of the imaginary time correlation length $\xi_{\tau,\text{imp}}^{(2)}$ and the improved estimator of the staggered susceptibility $\chi_{s,\text{imp}}$. (See text.)

Model	Observable	α_c	θ
A	z_L	0.7625(5)	1.65(39)
	$\xi_{\tau,\text{imp}}^{(2)}$	0.7619(3)	1.22(10)
	$\chi_{s,\text{imp}}$	0.7625(3)	1.79(7)
B	z_L	0.6211(1)	1.73(6)
	$\xi_{\tau,\text{imp}}^{(2)}$	0.6212(1)	1.92(8)
	$\chi_{s,\text{imp}}$	0.6212(1)	2.12(4)
C	z_L	0.4823(6)	1.52(9)
	$\xi_{\tau,\text{imp}}^{(2)}$	0.4819(2)	2.71(14)
	$\chi_{s,\text{imp}}$	0.4823(2)	2.45(6)
	z_L	1.3146(15)	1.65(17)
	$\xi_{\tau,\text{imp}}^{(2)}$	1.3145(21)	2.70(25)
	$\chi_{s,\text{imp}}$	1.3147(5)	1.93(2)

well-behaved, as it is “pinned” by its value of the longest chain or largest β , the value obtained from finite-size scaling depends, of course, on the type of fit function used. Especially for model **B** we could include $L = 512$ in the analysis and therefore get very accurate and consistent estimates of the critical coupling ratio α_c . We must, however, keep in mind that for a chain of length $L = 512$ there might already be a very small systematic error due to the temperature induced plateau. In the context of our discussion in Chapter 6, however, we concluded that this systematic error is sufficiently small and cannot be resolved. The situation is not as good for the critical exponent ν . We have seen that no definite value could be determined. This, in turn, makes it difficult to definitely draw conclusions about the presence of correction terms as more free fit parameters become involved. Thus, in order to securely determine leading corrections it seems necessary to get an independent estimate of at least the critical coupling ratio α_c , and feed it into fits that include corrections. Even better it would be to have an independent estimate of the critical exponent ν that generically controls the shift behaviour of the pseudo-critical points. Thus equipped, precise identification of leading corrections would be feasible.

8.2 Summary and Outlook

Antiferromagnetic mixed Heisenberg spin chains have been investigated by means of continuous imaginary time quantum Monte Carlo. Data sets thus produced have been analysed by the finite-size scaling method with and without correction terms. For models **A** and **B** (**C**) we identify 2(3) different gapped phases depending on the coupling ratio α and separated by 1(2) gapless phase boundaries at a critical value α_c [84, 85]. For models **A** and **C** the critical points have been studied before in [14] with the same algorithm. Exact calculations have been done in [11] and [12, 13] where in both cases a condition on gaplessness was derived by mapping onto the non-linear σ -model. Those results compared to the ones obtained from quantum Monte Carlo are shown in Table 8.2. Yet qualitatively confirming our results there remains a significant quantitative difference.

There are quantum critical points at $T = 0$, but no line of critical points at low non-zero temperatures. The particular choice of chain lengths and temperatures simulated did not provide sufficiently many data points for the usual finite-size scaling analysis with constant aspect ratio. In order to avoid further simulation of data sets at the end of the work a modified way of finite-size scaling was applied. The condition of the aspect ratio being approximately infinite is, however, only insufficiently well satisfied, and this renders the estimates of critical exponents, largely inconclusive.

The twist order parameter as presented in Section 3.5.1 proved a precise tool in order to detect pseudo-critical points. Its low temperature properties should be the subject of future investigation. It remains to be clarified if it is possible to “label” low-lying excited states in terms of the valence bond picture. It will be interesting to investigate the meaning of the temperature induced plateau-like shape of the twist order parameter discussed in Section 6.1. As reported in [86], VBS order is retained up to low non-zero temperature on the bilayer honeycomb lattice with $S = 1/2$. Above some temperature the VBS order is destroyed by droplet-like excitations that connect different symmetry related ground states. Whether such phenomena related to “deconfined” quantum criticality [86] are relevant in the one-dimensional case of uniform and mixed Heisenberg spin chains remains an interesting question to be investigated. Furthermore,

Table 8.2: Critical values of the coupling ratio α_c derived from field theoretic investigation compared to results from quantum Monte Carlo in this thesis. At $\alpha = \alpha_c$ two gapped phases are separated by a gapless boundary. Model **C** has two gapless boundaries (see Section 3.4.3).

Model	Fukui [11]	Takano [12, 13]	Quantum Monte Carlo
A	0.625	0.5714	0.7625(5)
B	0.5556	0.4286	0.6211(1)
C	0.2708	0.2553	0.4823(6)
	1.625	1.7143	1.3146(15)

it shall be enlightening to extend studies to general two dimensional Heisenberg systems of mixed spins.

Independent determination of the critical coupling ratio(s) could be done by calculating the Binder cumulant. Securely established values then could be fed into finite-size scaling fits equipped with various – though reasonable – correction terms.

In order to reliably compare and relate critical coupling ratios and exponents obtained from the twist order parameter to those obtained from diverging quantities, such as the correlation lengths and staggered susceptibilities it is highly desirable to determine precise values for the quantum critical point directly at $T = 0$. Using continuous time quantum Monte Carlo, i.e. the Loop Algorithm, it proved vital to use improved estimators of dynamic susceptibilities. Keeping the aspect ratio at a suitable and constant value and simulating up to sufficiently large systems should allow for simultaneous extrapolation to both the thermodynamic limit and the limit $T \rightarrow 0$ and provide proper estimates of the parameters of interest. Alternatively, the Loop Algorithm allows for direct implementation of the above limits [87]. Measurements of the twist order parameter could either be implemented as in the present algorithm of finite systems with segments of varying spatial extent (i.e. with open boundary conditions) and analysed by finite-size scaling methods, or, if possible, formulated in terms of cluster properties and measured via improved estimators. Quantum Monte Carlo methods could further be supplemented by density matrix renormalisation group calculations [88].

In any case, precise knowledge of zero temperature values is crucially important when trying to resolve low temperature properties of mixed quantum Heisenberg spin chains.

Appendix A

Finite-Size Scaling at Fixed Temperatures

The following tables show the results of fits to the finite-size scaling relations presented in Section 5.5.2. It was tried to resolve the temperature dependence of critical coupling ratios α_c and critical exponents ν , which is the inverse of the shift exponent θ . The analysis of the peak heights of diverging quantities, however, did not show criticality. Consequently, it is not meaningful to interpret the estimates shown in the tables as parameters of critical points.

For the results that are listed in the following tables, twist order parameter z_L , and improved and unimproved second-moment estimators, $\xi_{\tau,\text{imp}}^{(2)}$ and $\xi_{\tau,\text{unimp}}^{(2)}$, respectively, of the imaginary time correlation length were used. 10^5 measurements were taken after 10^4 sweeps for equilibration.

All fits were performed with the Levenberg–Marquardt χ^2 -minimisation routines from Numerical Recipes [63]. Error estimates show the square root of the diagonal elements of the covariance matrix.

Table A.1: Improved second-moment estimator of the imaginary time correlation length $\xi_{\tau,\text{imp}}^{(2)}$ of Model **A**. Chain lengths included: $L = 16, \dots, 512$ for $T = 0.01, 0.025$ and $L = 16, \dots, 256$ for $T = 0.04, 0.05$.

T	Fit	α_c	θ	a	b	χ_{pdof}^2
0.01	(5.48)	0.76244(5)	2.72(14)		-27(11)	2.1
	(5.52)	0.76254(9)	3.27(54)	-0.028(20)	-111(159)	2.4
	(5.53)	0.76209(8)		0.146(18)	-2.07(13)	10.1
	(5.54)	0.76256(5)	2.01(65)		-3.40(12)	11.0
	(5.55)	0.76226(8)	2.01(65)	0.069(13)	-4.74(28)	5.3
	(5.56)	0.76246(7)	2.72(14)	-0.004(9)	-27(2)	2.0
0.025	(5.48)	0.76289(8)	3.1(3)		-66(54)	1.12
	(5.52)					
	(5.53)	0.76239(16)		0.165(30)	-2.04(20)	6.39
	(5.54)	0.76308(8)	1.89(46)		-2.18(12)	8.32
	(5.55)	0.76255(15)	1.89(46)	0.107(24)	-3.61(34)	4.40
	(5.56)	0.76246(7)	3.1(3)	-0.008(14)	-63(6)	1.00
0.04	(5.48)	0.76440(13)	2.78(38)		-29(30)	2.23
	(5.52)	0.76468(27)	4.2(2.6)	-0.048(37)	-1205(8229)	3.10
	(5.53)	0.76400(26)		0.132(42)	-1.88(26)	5.43
	(5.54)	0.76440(12)	2.8(-)		-31.7(2.0)	1.45
	(5.55)	0.76449(21)	2.8(-)	0.013(22)	-29.8(3.9)	2.07
	(5.56)	0.76448(21)	2.78(38)	-0.011(23)	-27(3.6)	2.11
0.05	(5.48)	0.76526(21)	2.41(33)		-8(8)	3.59
	(5.52)	0.76448(102)	1.48(76)	0.25(58)	-1.5(1.1)	5.68
	(5.53)	0.76465(36)		0.141(46)	-1.70(27)	2.79
	(5.54)	0.76567(18)	1.63(-)		-0.875(62)	5.62
	(5.55)	0.76465(36)	1.63(-)	0.161(49)	-1.79(28)	2.86
	(5.56)	0.76517(30)	2.41(33)	0.010(26)	-8.5(1.4)	3.53

Table A.2: Unimproved second-moment estimator of the imaginary time correlation length $\xi_{\tau, \text{unimp}}^{(2)}$ of Model A. Chain lengths included: $L = 32, \dots, 512$ for $T = 0.01$ and $L = 16, \dots, 256$ for $T = 0.25$.

T	Fit	α_c	θ	a	b	χ_{pdof}^2
0.01	(5.48)					
	(5.52)					
	(5.53)	0.76233(19)		-0.023(63)	0.17(93)	0.31
	(5.54)					
	(5.55)					
	(5.56)					
0.025	(5.48)	0.76331(15)	3.4(8)		-206(465)	0.48
	(5.52)	0.76323(36)	3.1(1.3)	0.014(56)	-89(299)	0.91
	(5.53)	0.76264(35)		0.186(62)	-2.2(6)	1.41
	(5.54)	0.76340(14)	2.6(6)		-19.7(3.7)	0.87
	(5.55)	0.76311(35)	2.6(6)	0.038(31)	-24.8(5.5)	0.52
	(5.56)	0.76328(25)	3.4(8)	0.003(26)	-209(46)	0.48

Table A.3: Twist order parameter z_L of Model **A**. Chain lengths included: $L = 16, \dots, 512$.

T	Fit	α_c	θ	a	b	χ_{pdof}^2
0.01	(5.48)	0.76246(17)	1.7(1)		-4.4(1.3)	0.05
	(5.52)	0.76262(45)	1.9(6)	-0.09(22)	-6(7)	0.004
	(5.53)	0.76243(25)		0.001(67)	-3.62(42)	0.12
	(5.54)	0.76256(15)	1.61(5)		-3.355(94)	0.27
	(5.55)	0.76238(25)	1.61(5)	0.064(73)	-3.72(43)	0.11
	(5.56)	0.76248(25)	1.7(1)	-0.005(66)	-4.35(50)	0.05
0.025	(5.48)	0.76389(15)	1.55(6)		-3.1(6)	0.69
	(5.52)	0.76416(34)	1.8(5)	-0.16(15)	-4.8(3.5)	0.68
	(5.53)	0.76402(20)		-0.109(43)	-3.22(30)	0.55
	(5.54)	0.76416(11)	1.42(9)		-2.079(52)	1.87
	(5.55)	0.76377(22)	1.42(9)	0.137(65)	-2.58(24)	0.98
	(5.56)	0.76392(20)	1.55(6)	-0.008(52)	-3.03(29)	0.68
0.04	(5.48)	0.76508(29)	1.58(7)		-3.33(66)	1.55
	(5.52)	0.76637(53)	2.8(9)	-0.38(9)	-49(107)	1.32
	(5.53)	0.76529(39)		-0.102(57)	-3.26(37)	1.53
	(5.54)	0.76743(23)	1.1(2)		-0.767(20)	1.58
	(5.55)	0.76398(53)	1.1(2)	3.00(42)	-4.61(54)	3.54
	(5.56)	0.76519(40)	1.58(7)	-0.020(66)	-3.22(36)	1.53
0.05	(5.48)	0.76714(31)	1.45(6)		-2.43(42)	1.02
	(5.52)	0.76801(88)	2.2(1.2)	-0.39(24)	-8(22)	1.25
	(5.53)	0.76745(37)		-0.212(57)	-2.80(36)	0.96
	(5.54)	0.76786(24)	1.27(9)		-1.442(29)	3.19
	(5.55)	0.76675(44)	1.27(9)	0.41(14)	-2.34(30)	1.16
	(5.56)	0.76715(40)	1.45(6)	-0.005(83)	-2.42(31)	1.02

Table A.4: Improved second-moment estimator of the imaginary time correlation length $\xi_{\tau,\text{imp}}^{(2)}$ of Model **B**. Chain lengths included: $L = 16, \dots, 512$.

T	Fit	α_c	θ	a	b	χ_{pdof}^2
0.01	(5.48)	0.62132(5)	2.70(28)		-19(15)	0.35
	(5.52)	0.62126(9)	2.32(47)	0.020(30)	-7.4(8.7)	0.21
	(5.53)	0.62113(7)		0.091(16)	-1.45(16)	1.20
	(5.54)	0.62134(5)	2.44(7)		-8.98(48)	0.58
	(5.55)	0.62128(7)	2.44(7)	0.014(11)	-9.83(79)	0.16
	(5.56)	0.62131(7)	2.70(28)	0.003(10)	-19.6(1.6)	0.31
0.025	(5.48)	0.62163(5)	3.00(45)		-41(55)	5.31
	(5.52)	0.62125(17)	1.62(41)	0.17(14)	-1.8(1.4)	0.64
	(5.53)	0.62127(9)		0.145(26)	-1.70(25)	0.38
	(5.54)	0.62163(5)	3.2(7)		-77(12)	4.06
	(5.55)	0.62155(7)	3.2(7)	0.015(26)	-1.70(24)	0.38
	(5.56)	0.62153(7)	3.00(45)	0.026(13)	-54(9)	3.76
0.05	(5.48)	0.62286(7)	4.58(1.8)		-2537(12664)	17.34
	(5.52)	0.62184(33)	1.32(29)	0.73(93)	-1.61(48)	1.14
	(5.53)	0.62216(11)		0.239(25)	-2.07(19)	1.26
	(5.54)	0.62290(6)	2.3(-)		-3.63(42)	17.77
	(5.55)	0.62240(9)	2.3(-)	0.127(17)	-8.83(80)	3.95
	(5.56)	0.62263(9)	4.58(1.8)	0.049(12)	-3522(352)	11.46
0.075	(5.48)					
	(5.52)					
	(5.53)	0.62357(18)		0.243(41)	-1.76(27)	0.96
	(5.54)	0.62440(11)	1.7(-)		-0.29(11)	9.62
	(5.55)	0.62360(18)	1.7(-)	0.237(40)	-2.16(33)	1.10
	(5.56)					

Table A.5: Unimproved second-moment estimator of the imaginary time correlation length $\xi_{\tau, \text{unimp}}^{(2)}$ of Model **B**. Chain lengths included: $L = 32, \dots, 512$ for $T = 0.01$ and $L = 16, \dots, 512$ for $T = 0.025$.

T	Fit	α_c	θ	a	b	χ_{pdof}^2
0.01	(5.48)	0.62132(7)	2.8(1.2)		-51(237)	0.61
	(5.52)	0.62099(73)	1.2(1.8)	0.52(5.79)	-1.1(3.8)	0.40
	(5.53)	0.62114(15)		0.088(58)	-1.70(84)	0.68
	(5.54)	0.62130(6)	3.8(1.2)		-2046(1025)	0.64
	(5.55)	0.62132(11)	3.8(1.2)	0.005(22)	-1885(1210)	0.93
	(5.56)	0.62127(12)	2.8(1.2)	0.013(27)	-65(36)	0.49
0.025	(5.48)	0.62165(10)	3.11(75)		-64(142)	2.45
	(5.52)	0.62105(44)	1.42(68)	0.30(54)	-1.4(1.2)	0.93
	(5.53)	0.62117(19)		0.162(47)	-1.87(45)	0.66
	(5.54)	0.62170(10)	2.10(34)		-2.39(69)	2.68
	(5.55)	0.62132(17)	2.10(34)	0.092(33)	-5.9(1.5)	0.91
	(5.56)	0.62152(10)	3.11(75)	0.025(21)	-80(22)	1.97

Table A.6: Twist order parameter z_L of Model **B**. Chain lengths included: $L = 16, \dots, 512$.

T	Fit	α_c	θ	a	b	χ_{pdof}^2
0.01	(5.48)	0.62121(18)	1.59(5)		-5.75(83)	0.19
	(5.52)	0.62107(49)	1.51(26)	0.13(47)	-5.1(1.8)	0.23
	(5.53)	0.62130(22)		-0.115(57)	-5.75(40)	0.17
	(5.54)	0.62112(15)	1.64(5)		-6.56(14)	0.36
	(5.55)	0.62127(23)	1.64(5)	-0.051(61)	-6.22(43)	0.24
	(5.56)	0.62120(23)	1.59(5)	-0.004(64)	-5.78(40)	0.19
0.025	(5.48)	0.62141(17)	1.57(4)		-5.32(49)	1.16
	(5.52)	0.62172(41)	1.76(26)	-0.20(21)	-7.4(3.7)	1.43
	(5.53)	0.62158(22)		-0.153(40)	-5.45(24)	1.07
	(5.54)	0.62127(12)	1.61(10)		-5.922(64)	1.21
	(5.55)	0.62150(22)	1.61(10)	-0.055(44)	-5.62(25)	1.08
	(5.56)	0.62148(20)	1.57(4)	-0.005(46)	-5.29(24)	1.16
0.05	(5.48)	0.62256(52)	1.44(4)		-3.93(40)	0.07
	(5.52)	0.62220(143)	1.34(35)	0.3(1.4)	-3.74(33)	0.07
	(5.53)	0.62307(59)		-0.355(62)	-4.64(33)	0.18
	(5.54)	0.62291(26)	1.41(7)		-3.639(37)	0.21
	(5.55)	0.62245(63)	1.41(7)	0.074(92)	-3.86(28)	0.58
	(5.56)	0.62254(62)	1.44(4)	0.003(87)	-3.94(28)	0.07
0.075	(5.48)	0.62211(65)	1.48(5)		-4.44(55)	2.30
	(5.52)	0.61935(269)	1.03(30)	15(150)	-17(169)	2.45
	(5.53)	0.62250(76)		-0.296(77)	-5.07(42)	2.49
	(5.54)	0.62354(41)	1.36(26)		-3.223(44)	3.60
	(5.55)	0.62147(83)	1.36(26)	0.38(14)	-4.21(35)	2.02
	(5.56)	0.62200(80)	1.48(5)	0.02(11)	-4.50(38)	2.29

Table A.7: Improved second-moment estimator of the imaginary time correlation length $\xi_{\tau,\text{imp}}^{(2)}$ of Model **C** – left transition. Chain lengths included: $L = 16, \dots, 256$.

T	Fit	α_c	θ	a	b	χ_{pdof}^2
0.01	(5.48)	0.48224(15)	1.23(24)		-0.20(16)	0.08
	(5.52)	0.48235(16)	2.9(5.3)	-0.083(36)	-6(77)	0.02
	(5.53)	0.48230(14)		-0.064(33)	-0.26(27)	0.05
	(5.54)	0.48224(6)	1.23(7)		-0.20(3)	0.06
	(5.55)	0.48225(19)	1.23(7)	-0.003(98)	-0.20(21)	0.08
	(5.56)	0.48225(19)	1.23(24)	-0.002(10)	-0.20(21)	0.08
0.025	(5.48)	0.48279(21)	1.35(32)		-0.20(16)	1.30
	(5.52)					
	(5.53)	0.48283(23)		-0.045(41)	-0.38(35)	1.35
	(5.54)	0.48303(15)	1.00(34)		-0.086(13)	1.32
	(5.55)	0.48263(36)	1.00(34)	-5.3(4.3)	5.1(4.2)	1.21
	(5.56)	0.48277(21)	1.35(32)	0.007(83)	-0.31(27)	1.29
0.04	(5.48)	0.48314(18)	1.51(17)		-0.73(38)	3.33
	(5.52)					
	(5.53)	0.48318(23)		-0.035(36)	-0.83(26)	3.39
	(5.54)	0.48325(11)	1.40(34)		-0.516(43)	2.63
	(5.55)	0.48306(26)	1.40(34)	0.049(60)	-0.68(21)	3.28
	(5.56)	0.48312(25)	1.51(17)	0.005(48)	-0.76(24)	3.33

Table A.8: Unimproved second-moment estimator of the imaginary time correlation length $\xi_{\tau,\text{unimp}}^{(2)}$ of Model **C** – left transition. Chain lengths included: $L = 32, \dots, 256$.

T	Fit	α_c	θ	a	b	χ_{pdof}^2
0.01	(5.48)	0.48230(28)	1.48(55)		-1.0(2.2)	0.10
	(5.52)					
	(5.53)	0.48236(37)		-0.06(12)	-1.3(1.5)	0.12
	(5.54)	0.48233(11)	1.43(18)		-0.81(17)	0.05
	(5.55)	0.48227(46)	1.43(18)	0.03(21)	-0.9(1.2)	0.10
	(5.56)	0.48229(44)	1.48(55)	0.01(19)	-1.0(1.2)	0.10

Table A.9: Twist order parameter z_L of model **C** – left transition. Chain lengths included: $L = 16, \dots, 256$ for $T = 0.01$ and $L = 16, \dots, 512$ for $T = 0.025, 0.04$.

T	Fit	α_c	θ	a	b	χ_{pdof}^2
0.01	(5.48)	0.48360(48)	1.32(5)		-4.90(72)	4.46
	(5.52)					
	(5.53)	0.48464(52)		-0.93(12)	-6.43(89)	6.79
	(5.54)	0.48308(22)	1.38(9)		-5.94(8)	3.62
	(5.55)	0.48366(62)	1.38(9)	-0.21(21)	-5.24(70)	4.91
	(5.56)	0.48338(65)	1.32(5)	0.09(25)	-5.15(68)	4.39
0.025	(5.48)	0.48240(43)	1.31(4)		-4.47(56)	2.23
	(5.52)					
	(5.53)	0.48337(45)		-0.915(89)	-5.92(73)	3.52
	(5.54)	0.48259(23)	1.29(6)		-4.200(70)	1.74
	(5.55)	0.48221(53)	1.29(6)	0.16(22)	-4.61(55)	2.14
	(5.56)	0.48229(55)	1.31(4)	-0.05(20)	-4.60(55)	2.21
0.04	(5.48)	0.48189(47)	1.25(4)		-3.77(43)	0.30
	(5.52)	0.48132(205)	1.10(48)	3(20)	-6(20)	0.41
	(5.53)	0.48285(46)		-1.073(82)	-4.86(67)	0.59
	(5.54)	0.48105(27)	1.33(4)		-4.895(66)	1.62
	(5.55)	0.48212(54)	1.33(4)	-1.073(82)	-4.85(67)	0.59
	(5.56)	0.48188(56)	1.25(4)	0.01(22)	-3.78(51)	0.30

Table A.10: Twist order parameter z_L of model **C** – right transition. Chain lengths included: $L = 16, \dots, 256$ for $T = 0.01$ and $L = 16, \dots, 512$ for $T = 0.025, 0.04$.

T	Fit	α_c	θ	a	b	χ_{pdof}^2
0.01	(5.48)	1.3126(14)	1.41(9)		9.4(2.8)	2.38
	(5.52)					
	(5.53)	1.3116(17)		0.94(34)	12.2(2.6)	2.95
	(5.54)	1.3134(7)	1.48(14)		11.62(43)	1.78
	(5.55)	1.3127(18)	1.48(14)	0.22(48)	10.6(2.3)	2.57
	(5.56)	1.3132(19)	1.41(9)	-0.17(55)	10.0(2.1)	2.95
0.025	(5.48)	1.3146(7)	1.47(6)		10.7(2.4)	0.22
	(5.52)	1.3142(16)	1.57(45)	0.4(1.4)	12.5(10.2)	0.29
	(5.53)	1.3139(8)		0.71(17)	13.0(1.8)	0.16
	(5.54)	1.3167(5)	1.77(26)		30.82(92)	6.80
	(5.55)	1.3137(8)	1.77(26)	0.80(16)	18.5(2.6)	0.27
	(5.56)	1.3146(9)	1.47(6)	0.01(26)	10.7(1.5)	0.22
0.04	(5.48)	1.3146(5)	1.38(6)		7.7(1.7)	0.76
	(5.52)	1.3132(10)	1.93(48)	1.20(45)	22(27)	0.25
	(5.53)	1.3137(6)		0.96(15)	10.4(1.7)	0.30
	(5.54)	1.3142(3)	1.32(6)		6.16(14)	0.84
	(5.55)	1.3146(7)	1.32(6)	-0.30(35)	7.1(1.2)	0.88
	(5.56)	1.3145(7)	1.38(6)	0.06(30)	7.5(1.3)	0.74

Bibliography

- [1] A. Auerbach: *Interacting electrons and quantum magnetism* (Springer, New York 1994)
- [2] S. Sachdev: *Quantum phase transitions* (Cambridge University Press, Cambridge 1999)
- [3] F.D.M. Haldane: Phys. Rev. Lett. **50**, 1153 (1983)
- [4] I. Affleck, T. Kennedy, E.H. Lieb, H. Tasaki: Phys. Rev. Lett. **59**, 799 (1987)
- [5] J. Zinn-Justin: *Quantum field theory and critical phenomena* (Clarendon Press, Oxford 1996)
- [6] H.G. Evertz, G. Lana, M. Marcu: Phys. Rev. Lett. **70**, 873 (1993)
- [7] H.G. Evertz: Adv. Phys. **52**, 1 (2003)
- [8] B.B. Beard: *Improvements in cluster algorithms for quantum spin chains* (PhD Thesis, Massachusetts 1996)
- [9] B.B. Beard, U.J. Wiese: Phys. Rev. Lett. **77**, 5130 (1996)
- [10] E. Lieb, D. Mattis: J. Math. Phys. **3**, 749 (1962)
- [11] T. Fukui, N. Kawamaki: Phys. Rev. B **55**, R14 709 (1997)
- [12] K. Takano: Phys. Rev. Lett. **82**, 5124 (1999)
- [13] K. Takano: Phys. Rev. B **61**, 8863 (2000)
- [14] Z. Xu, J. Dai, H. Ying, B. Zeng: Phys. Rev. B **67**, 214 426 (2003)
- [15] M. Hase, I. Terasaki, K. Uchinokura: Phys. Rev. Lett. **70**, 3651 (1993)
- [16] T. Nakamura: Phys. Rev. B **71**, 144 401 (2005)
- [17] T. Masuda, A. Zheludev, H. Manaka, L.-P. Regnault, J.-H. Chung, Y. Qiu: Phys. Rev. Lett., submitted (2005); cond-mat/0511143

- [18] T. Masuda, A. Zheludev, H. Manaka, J.-H. Chung: submitted to proceedings of LT24, Orlando, FL, (2005); cond-mat/0506382
- [19] H. Manaka, I. Yamada: *J. Phys. Jpn. Soc.* **66**, 1908 (1997)
- [20] H. Manaka, I. Yamada, H. Aruga Katori: *Phys. Rev. B* **63**, 104 408 (2001)
- [21] W.J.L. Buyers, R.M. Morra, R.L. Armstrong, M.J. Hogan, P. Gerlach, K. Hirawaka: *Phys. Rev. Lett.* **56**, 371 (1986)
- [22] J.P. Renard, M. Verdaguer, L.P. Regnault, W.A.C. Erkelens, J. Rossat-Mignod, W.C. Stirling: *Europhys. Lett.* **3**, 945 (1987)
- [23] S. Yamamoto, H. Hori: *J. Phys. Soc. Jpn.* **73**, 822 (2004)
- [24] Z. Honda, K. Katsumata, H. Aruga Katori, K. Yamada, T. Ohishi, T. Manabe, M. Yamashita: *J. Phys. Condens. Matter* **9**, 3487 (1997)
- [25] A. Zheludev, Z. Honda, K. Katsumata, R. Feyerherm, K. Prokes: *Europhys. Lett.* **55**, 868 (2001)
- [26] Z. Honda, H. Asakawa, K. Katsumata: *Phys. Rev. Lett.* **81**, 2566 (1998)
- [27] A. Zheludev, Z. Honda, Y. Chen, C.L. Broholm, K. Katsumata, S.M. Shapiro: *Phys. Rev. Lett.* **88**, 077 206 (2002)
- [28] Y. Uchiyama, Y. Sasago, I. Tsukada, K. Uchinokura, A. Zheludev, T. Hayashi, N. Miura, P. Bni: *Phys. Rev. Lett.* **83**, 632 (1999)
- [29] G. Xu, J.F. DiTusa, T. Ito, H. Takagi, C.L. Bonholm, G. Aeppli: *Phys. Rev. B* **54** R6827 (1996)
- [30] A. Zheludev, S. Maslov, T. Yokoo, S. Raymond, S.E. Nagler, J. Akimitsu: *J. Phys. Condens. Matter* **13** R525 (2001)
- [31] M. Hagiwara, K. Kobayashi, T. Chihara: *J. Phys. Soc. Jpn.* **66**, 1702 (1997)
- [32] M. Hagiwara, Y. Narumi, K. Kindo, M. Kohno, H. Nakano, R. Sato, M. Takahashi: *Phys. Rev. Lett.* **80**, 1312 (1998)
- [33] Y. Narumi, M. Hagiwara, M. Kohno, K. Kondo: *Phys. Rev. Lett.* **86**, 324 (2001)
- [34] M. Hagiwara, Y. Narumi, K. Kindo, M. Kohno, H. Nakano, R. Sato, M. Takahashi: *RIKEN Rev.* **46**, 14 (2002)
- [35] M. Verdaguer, A. Gleizes, J.P. Renard, J. Seiden: *Phys. Rev. B* **29**, 5144 (1984)

- [36] M. Hagiwara, K. Minami, Y. Narumi, K. Tatani, K. Kindo: J. Phys. Soc. Jpn. **67**, 2209 (1998)
- [37] F. Schwabl: *Statistische Mechanik* (Springer, Berlin Heidelberg 2000)
- [38] M. Plischke, B. Bergersen: *Equilibrium statistical physics* (World Scientific, Singapore 1994)
- [39] J.M. Yeomans: *Statistical mechanics of phase transitions* (Oxford University Press, Oxford New York 1992)
- [40] J.J. Binney, N.J. Dowrick, A.J. Fisher, M.E.J. Newman: *The theory of phase transition – An introduction to the renormalization group* (Oxford University Press, Oxford New York 1992)
- [41] R. Shankar: *Principles of quantum mechanics* (Plenum Press, New York 1994)
- [42] D.P. Landau, K. Binder: *A guide to Monte Carlo simulations in statistical physics* (Cambridge University Press, Cambridge 2000)
- [43] J.C. Le Guillou, J. Zinn-Justin: Phys. Rev. B **21**, 3976 (1980)
- [44] K. Chen, A.M. Ferrenberg, D.P. Landau: Phys. Rev. B **48**, 3249 (1993)
- [45] C. Holm, W. Janke: Nucl. Phys. B (Proc. Suppl.) **30**, 846 (1993)
- [46] C. Holm, W. Janke: Phys. Rev. B **48**, 936 (1993)
- [47] W.J. Camp, J.P. Van Dyke: J. Phys. A **9**, 731 (1976)
- [48] A. Berger, G. Campillo, P. Vivas, J.E. Pearson, S.D. Bader, E. Baca, P. Prieto: J. Appl. Phys. **91**, 8393 (2002)
- [49] M. Campostrini, M. Hasenbusch, A. Pelissetto, P. Rossi, E. Vicari: Phys.Rev. B **63**, 214 503 (2001)
- [50] E. Bittner, W. Janke: Phys. Rev. B **71** 024 512 (2005)
- [51] J.A. Lipa, D.R. Swanson, J.A. Nissen, T.C.P. Chui, U.E. Israelsson: Phys. Rev. Lett. **76**, 944 (1996)
- [52] J.A. Lipa, J.A. Nissen, D.A. Stricker, D.R. Swanson, T.C.P. Chui: Phys. Rev. B **68**, 174 518 (2003)
- [53] S. Todo, K. Kato: Phys. Rev. Lett. **87**, 047 203 (2001)

- [54] W. Heisenberg: Z. Phys. **49**, 619 (1928) in: W. Blum, H.P. Dürr, H. Rechenberg (Eds.): *Heisenberg Gesammelte Werke* (Springer, Berlin Heidelberg 1985)
- [55] N. Kawashima, J.E. Gubernatis: Phys. Rev. Lett. **73**, 1295 (1994)
- [56] N. Kawashima, J.E. Gubernatis: J. Stat. Phys. **80**, 169 (1995)
- [57] M. Karbach, G. Müller: Comp. Phys. **11**, 36 (1997)
- [58] M. Karbach, K. Hu, G. Müller: Comp. Phys. **12**, 565 (1998)
- [59] M. Karbach, K. Hu, G. Müller: cond-mat/0008018 (2004)
- [60] W. Marshall: Proc. R. Soc. **48**, A232 (1955)
- [61] C. Degli Eposti Boschi, E. Ercolessi, G. Morandi: Proc. Symp. *Symmetries in Science XIII*, (Bregenz, Austria 2004)
- [62] M. Nakamura, S. Todo: Phys. Rev. Lett. **89**, 077 204 (2002)
- [63] H. W. Press, S. A. Teukolsky, W. T. Vetterling: *Numerical Recipes in C* (Cambridge University Press, Cambridge 1993)
- [64] I. Affleck, T. Kennedy, E.H. Lieb, H. Tasaki: Commun. Math. Phys. **115**, 477 (1988)
- [65] C.K. Majumdar, D.K. Ghosh: J. Math. Phys. **10**, 1388 (1969)
- [66] S. Todo, M. Matsumoto, C. Yasuda, H. Takayama: Phys. Rev. B **64**, 224 412 (2001)
- [67] M. Matsumoto, C. Yasuda, S. Todo, H. Takayama: Phys. Rev. B **65**, 014 407 (2001)
- [68] A. Cuccoli, V. Tognetti: Phys. Rev. B **52**, 10 221 (1995)
- [69] A. Cuccoli, T. Roscilde, V. Tognetti, R. Vaia, P. Verrucchi: Phys. Rev. B **67**, 104 414 (2003)
- [70] G.G. Lonzarch: Nature Phys. **1**, 11 (2005)
- [71] A. Kopp, S. Chakravarty: Nature Phys. **1**, 53 (2005)
- [72] M. Vojta: Rep. Prog. Phys. **66**, 2069 (2003)
- [73] D. Mermin, H. Wagner: Phys. Rev. Lett. **17**, 1133 (1966)
- [74] P.C. Hohenberg: Phys. Lett. **114A**, 331 (1967)
- [75] T. Kennedy, H. Tasaki: Commun. Math. Phys. **147**, 431 (1992)

- [76] W. Janke, *Statistical Analysis of Simulations: Data Correlations and Error Estimation* in: J. Grotendorst, D. Marx, A. Muramatsu (Eds.): *Proceedings of the Euro Winter School Quantum Simulations of Complex Many-Body Systems: From Theory to Algorithms*, NIC Series **10**, 423 (2002); www.physik.uni-leipzig.de/~janke/publications.html
- [77] R.H. Swendsen, J.S. Wang: Phys. Rev. Lett. **58**, 86 (1997)
- [78] U. Wolff: Phys. Rev. Lett. **62**, 361 (1989)
- [79] M.E. Fisher, M.N. Barber: Phys. Rev. Lett. **28**, 1516 (1972)
- [80] J. L. Cardy (Ed.): *Current Physics Sources and Comments Vol.2: Finite Size Scaling* (North Holland, Amsterdam 1998)
- [81] B. Widom: J. Chem. Phys. **43**, 2892 (1965)
- [82] K.G. Wilson: Phys. Rev. B **4**, 3174 (1971)
- [83] C. Hoelbling, C.B. Lang: Phys. Rev. B **54**, 3434 (1996)
- [84] P.R. Crompton, W. Janke, Z.X. Xu, H.P. Ying: Nucl. Phys. B (Proc. Suppl.) **140**, 817 (2005)
- [85] R. Bischof, P.R. Crompton: Phys. Rev. B, submitted (2005); cond-mat/0507148
- [86] A. Vishwanath, L. Balentis, T. Senthil: Phys. Rev. B **69**, 224 416 (2004)
- [87] H.G. Evertz, W. von der Linden: Phys. Rev. Lett. **86**, 5164 (2001)
- [88] S.R. White: Phys. Rev. Lett. **69**, 2863 (1992)